UAV-based Measurement of Marine Vessels Smoke Plumes – Guidance and Control System

David Coelho Escudeiro

Thesis to obtain the Master of Science Degree in

Aerospace Engineering

Supervisors: Dr. Rita Maria Mendes de Almeida Correia da Cunha
Dr. Paulo André Nobre Rosa

Examination Committee

Chairperson: Prof. José Fernando Alves da Silva
Supervisor: Dr. Rita Maria Mendes de Almeida Correia da Cunha
Member of the Committee: Prof. Pedro Manuel Urbano de Almeida Lima

March 2018

To my parents.

Acknowledgments

Firstly, I would like to thank my supervisors, Dr. Rita Cunha and Dr. Paulo Rosa, for their invaluable guidance, help, and support throughout this work. Their deep knowledge and intuition certainly contributed to develop my research and to obtain a more consolidated work.

My profound gratitude to my Parents and Sister, for their unconditional love and support through all my life, especially in the most challenging moments. To my Parents Ana Paula and João Carlos for providing me with all the conditions to succeed in my studies, and to my Sister Patrícia, for being the best housemate. To my Grandmothers, Fernanda and Joana, for all their affection and patience, being always available for me. To Marta, for her love, invaluable friendship and for being always there for me.

I also want to thank all my friends and colleagues for helping me to overcome each course of these intensive years. For sure IST gave me much more than just a Master degree, but true friends for life.

This work was conducted with the support of Deimos Engenharia, to whom I would like to thank the opportunity and warm welcome at the company, especially to Eng. Pedro Freire da Silva who was the first responsible for making this cooperation possible, and for introducing me to Dr. Paulo Rosa. Finally, but no less importantly, I would like to thank all members of DSOR group, for welcoming me in the lab and for always being kind and supportive.

The work of this thesis was performed within the framework of projects UID/EEA/50009/2013 and PTDC/EEI-AUT/5048/2014 funded by Fundação para a Ciência e Tecnologia.

Abstract

This dissertation addresses the problem of designing a Guidance and Control (G&C) system for UAV-based monitoring of marine vessels gas emissions. A constant speed, fixed-wing UAV is considered for this purpose, aiming to track a slower vessel and provide enhanced conditions for the smoke plume gas measurements. The adopted solution can be separated into two parts: a path planning approach, in which a virtual reference point is generated, at each time instant, providing the desired trajectory for the UAV to satisfy the given mission restrictions; and a nonlinear control law design, to guarantee that the UAV heading rate converges to the reference trajectory. In terms of path planning, an oscillatory motion was adopted for the reference point, allowing for the compensation of the speed difference between both vehicles, while respecting the UAV maximum heading rate. For the control part, a novel error formulation is proposed, leading to a nonlinear design with global asymptotic stability guarantees, achieved by using Lyapunov-based methods for nonlinear cascade systems. The control law thus obtained is the main contribution of this dissertation, as it solves the reference trajectory tracking control problem for a fixed-speed nonholonomic vehicle. Finally, the overall system is implemented and simulation results are presented to support the theoretical developments. Sufficient conditions to ensure the enforcement of the actuation bounds are introduced, and the performance of the novel error formulation is assessed.

Keywords: Unmanned Aerial Vehicles (UAVs); Guidance and Control (G&C) System; Trajectory Tracking; Nonholonomic Systems; Nonlinear Control; Lyapunov Design

Resumo

Esta dissertação aborda o desenho de um sistema de Guiamento e Controlo para monitorização aérea, baseada em UAVs, das emissões de gases de embarcações marítimas. Um UAV de asa fixa e velocidade constante é considerado, com o objectivo de seguir um navio com velocidade inferior, proporcionando condições ideais para as medições da pluma de fumo. A solução adotada pode ser dividida em duas partes: uma técnica de planeamento de rota, responsável por gerar um ponto de referência em cada instante de tempo, fornecendo as condições desejadas ao UAV para cumprir os requisitos da missão; e o desenho de uma lei de controlo não-linear, garantindo que a taxa de rumo do UAV converge para a referência. Para o planeamento de rota, um movimento oscilatório foi adotado para o ponto de referência, ajustando a sua trajectória à diferença de velocidades entre os dois veículos, respeitando a taxa de rumo máxima do UAV. Para o problema do controlo, uma nova formulação do erro é proposta, levando ao desenho não-linear com garantias de estabilidade assimptótica global, alcançada através da aplicação de métodos de Lyapunov para sistemas não-lineares em cascata. A lei de controlo então obtida é a principal contribuição deste trabalho, resolvendo o problema do seguimento de trajectórias de referência para veículos não-holonómicos com velocidade constante. Finalmente, o sistema completo é implementado e resultados de simulação são apresentados para suportar os desenvolvimentos teóricos. Condições suficientes para garantir o cumprimento dos limites de atuação são introduzidas, e o desempenho da formulação proposta foi avaliado.

Palavras-Chave: Veículos Aérios Não Tripulados; Sistema de Guiamento e Controlo; Seguimento de Trajectórias; Sistemas Não-holonómicos; Controlo Não-Linear; Análise de Lyapunov

Contents

List of Tables

List of Figures

Acronyms

ATC Air Traffic Control.

CO Center of Oscillation.

CompMon Compliance Monitoring pilot for Marpol Annex VI.

ENU East North Up.

EU European Union.

FSC Fuel Sulphur Content.

G&C Guidance and Control.

GHG Greenhouse.

GNC Guidance, Navigation, & Control.

GPS Global Positioning System.

IMO International Maritime Organization.

IMU Inertial Measurement Unit.

ISS Input-to-State Stability.

IST Instituto Superior Técnico.

LOS Line of Sight.

LPV Linear Parameter-Varying.

MARPOL International Convention for the Prevention of Pollution from Ships.

MHE Moving Horizon Estimation.

MPC Model Predictive Control.

MSc Masters degree in the area of Science..

RPAS Remote Piloted Airborne Systems.

SECA Sulphur Emission Control Area.

UAV Unmanned Aerial Vehicle.

Chapter 1

Introduction

1.1 Motivation

Currently, more than 90% of world trade is being carried by marine vessels, as this is the most cost-effective way of moving en masse goods and raw materials all over the world [1]. Such a great number should suggest an equally large impact on the Greenhouse Gases (GHGs) emissions. According to a study done by the International Maritime Organization (IMO) [1], the annual average fuel consumption of all the ships in the world stands between 247 and 325 million tonnes of fuel, considering the time interval between 2007 and 2012. Comparing to the global anthropogenic (human-induced) sources, shipping CO_2 emissions represent only a small portion of approximately 3.1%, on average in the same time span, as depicted in Table 1.1:

Table 1.1: Shipping CO_2 emissions compared with global CO_2 emissions from anthropogenic sources (values in millions of tonnes) [1]

Year	Global CO_2	Total shipping	% of global	International shipping	% of global
2007	31,409	1,100	3.5%	885	2.8%
2008	32,204	1,135	3.5%	921	2.9%
2009	32,047	978	3.1%	855	2.7%
2010	33,612	915	2.7%	771	2.3%
2011	34,723	1,022	2.9%	850	2.4%
2012	35,640	938	2.6%	796	2.2%
Average	33,273	1,015	3.1%	846	2.6%

Not only the carbon dioxide CO_2 but also other fine particles such as SO_x and NO_x represent a threat to the environment and consequently to the human health. According to the same study [1], IMO estimates that the shipping SO_x and NO_x emissions between 2007 and 2012 represent in average 15% and 13%, of the global emissions, respectively.

Even with the sulphur and nitrous oxides from shipping having a more significant impact on the global emissions than the carbon dioxide, one may think that shipping does not have a heavy ecological footprint as it was expected. However, these percentages are comparing to all anthropogenic sources. If only the means of transport are considered, the numbers can be slightly different. According to recent studies presented in the journal “The Economist” [2], the 15 biggest ships alone emit more oxides of sulphur and nitrogen than all the cars in the world. This is a serious environmental threat, and further measures on efficiency and emissions should be taken to mitigate the significant shipping emissions growth, which is patent in the projections for the coming decades [1].

Given the inevitable growth in the number of marine vessels operating in the oceans, due to its economic advantage over the other means of cargo transportation, the way to decelerate the trend of growth in emissions is to limit the impact of each individual ship in the global gas emissions. The MARPOL Convention implemented in 1973 by the IMO was the first global effort to reduce the pollution of the ocean and seas, including dumping, oil, and air pollution.

More concretely, the MARPOL Annex VI, first adopted in 1997 and extensively revised in 2008, imposes fixed limits on the main air pollutants contained in ship exhaust gases, including the sulphur and nitrous oxides, and other particulate matter. The most specific limit is presented in Regulation 14 of the MARPOL Annex VI [3], where different limits are applicable for ships operating inside or outside a Sulphur Emission Control Area (SECA).

Table 1.2: Limits on the SO_x shipping emissions applied in the MARPOL Annex VI - Regulation 14 [3]. The values are expressed in terms of % m/m (mass by mass).

Outside a SECA	**Inside a SECA**
4.50% prior to 1 January 2012	1.50% prior to 1 July 2010
3.50% on and after 1 January 2012	1.00% on and after to 1 July 2010
0.50% on and after 1 January 2020	0.10% on and after to 1 January 2015

As depicted in Table 1.2, the imposed SO_x limits are much stricter inside rather thean outside a SECA. In the European Union (EU), the established SECAs cover the Baltic and the North Sea area, including the English Channel. While the current limit outside the SECAs is fairly easy to comply with for most of the ships, inside this area an effective control must be pursued in order to ensure the limits are duly satisfied.

As the new limit for the shipping sulphur emissions in the SECAs entered into force in the beginning of 2015, some of the EU Member States around the SECA area – Belgium, Finland, Sweden and The Netherlands – joined forces to create the Compliance Monitoring pilot for Marpol Annex VI (CompMon) network. The CompMon project aims to provide a tighter control on the ship compliance with the MARPOL Annex VI. This can be achieved through the use of remote sensing and sampling methods to measure the sulphur emissions of ships, in order to determine those who are possibly non-compliant with the MARPOL Annex VI. When some high sulphur concentration is found, the national enforcement authorities should receive this information, so they can proceed to more accurate on-board inspections [4].

The sulphur emissions from maritime shipping can be monitored from land or with airborne devices. Land monitoring can be achieved by means of a sniffer sensor placed near the shipping lanes, along the coastline or on a bridge, having a very limited range, thus getting worse measurements. Airborne monitoring gives a greater coverage of the sea and can provide faster and more precise measurements. Report [5] summarizes some recommendations for the airborne measurement of Fuel Sulphur Content (FSC), particularly the types of sensors available and the different flight approaches. For instance, from August to November 2016, a Belgian aircraft equipped with a sniffer sensor performed aerial monitorization of FSC on more than 1300 ships, out of which almost 100 were potentially non-compliant [6].

With the evolution of technology leading to lighter and cheaper sniffer sensors, it is reasonable to assume that the tendency for the future is to perform the monitorization of emissions with UAVs, reducing both the risks and the costs, and increasing the efficiency of the measurements. Moreover, this monitorization will be needed also outside the SECA area, as the limits on the SO_x shipping emissions will decrease to 0.5% (m/m) (cf. Table 1.2), requiring a significant increase in the monitoring means.

Looking upon the importance of the monitorization of the gas emissions of marine vessels, the main objective of this dissertation is the development of a Guidance and Control System for an autonomous fixed-wing UAV, allowing for the tracking of a marine vessel, more precisely of its smoke plume.

1.2 State-of-the-Art

This section provides a brief literature review on the two main problems related to measurement of marine vessels smoke plumes using fixed-wing UAVs: the smoke plume detection and/or localization and the UAV tracking to the plume.

1.2.1 Smoke plume detection

The problem of active airborne monitoring of shipping sulphur emissions has its main difficulty on the localization of the smoke plume. A similar field where the problem of smoke detection arises is in the

forest fire surveillance, where the commonly used fixed smoke sensors have some limitations. A single sensor has a very short coverage, and cannot provide information about the location of the source or the size of the smoke plume. Therefore, video-based smoke and fire detection has been an active research field in the last years [7, 8, 9] – some of them using UAVs [10, 11, 12]–, aiming for an early forest fire detection. Also outside the forest fire scope, there is effort on the development of image processing algorithms capable of recognizing the smoke properties based on video. Some authors focus more on the chromatic and pixel energy properties [13, 14], while others on the smoke shape and its dynamic features [15, 16, 17]. For a proper overview of the more technical issues of this research field, the reader is referred to [18] and references therein.

Despite all the progress attained so far in the video-based smoke detection, there is still room for improvement in order to decrease the false alarm rates. Moreover, most of the developed computer vision techniques are only valid for static image sources, therefore not directly applicable to the localization of vessels smoke plumes.

A different approach to the smoke/gas sensing is the use of autonomous vehicles to perform gas distribution mapping and gas source localization. Soares J. *et al.*[19] propose a graph-based formation algorithm to track an odor plume with ground robots, adapting the robots formation to the plume shape, in order to find the gas source. Similarly, Neumann, P. and his co-workers [20, 21] employ a gas-sensitive micro-drone – a small quadcopter equipped with a gas detector –, performing several consecutive samplings in different positions, in order to map the gas distribution of a predefined area, and also to track the smoke plume to find its source location. These papers also present another feature, the wind velocity estimation in real-time based only on the IMU information. These additional measurements can help estimate the direction of the gas source with respect to the current position.

Within the scope of the present work, the previous method for gas distribution mapping becomes unfeasible due to the speed constraints of a fixed-wing UAV. However, knowing the position of the vessel, the source of the smoke plume is also known. Hence, the wind direction is estimated, one can have an acceptable estimate of the smoke plume location.

On the aircraft-based wind estimation, several solutions are available in the literature, including some primary work for Air Traffic Control (ATC) applications, which enabled to estimate the wind field based on aircraft radar tracks in addition to magnetic heading and the true airspeed [22], or even with only the radar track during turn maneuvers [23]. More recently, some methodologies were developed in order to estimate the wind velocity vector on-board small fixed-wing UAVs, all of them based on the wind triangle, depicted in Figure 1.1:

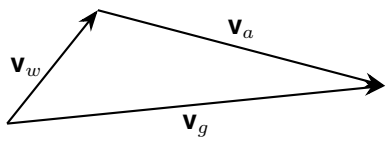

Figure 1.1: The wind triangle is defined by the UAV ground vector, $\mathbf{v}_g$, the wind vector, $\mathbf{v}_w$, and the flight vector, $\mathbf{v}_a$.

Aiming to enable energy harvesting, a method for wind field estimation is proposed in [24], using the sensors already available onboard the UAV, together with its kinematic model. In [25], the high sensitivity to the wind of a delta wing is exploited, and an iterative optimization method is proposed, combining the data from Global Positioning System (GPS) and Inertial Measurement Unit (IMU) with an aerodynamic model. Other methods are available using only the onboard sensors, without the need of any kinematic or aerodynamics models. While some solutions require more complex air data systems [26, 27], others are able to determine the wind velocity vector combining only the information from the GPS, IMU and a standard Pitot tube, with the UAV flying at different headings, such as in banking turns or cycle maneuvers [28, 29].

Given the available possibilities for the wind vector estimation requiring only the basic sensor suite onboard a fixed-wing UAV, this information will be considered to be known for the present study.

1.2.2 Target tracking

After the localization of the smoke plume, the UAV should be able to fly through it, while keeping track with the motion of the vessel. This challenge is to be tackled by the guidance system, which should plan the UAV trajectory, making sure it is able to follow it. In the literature, there are several publications

concerning the target tracking problem, from path planning and path following techniques to vision-based target tracking systems. All of them consider simpler, low-order kinematic models of the UAVs, in order to avoid more complex problems regarding the full aircraft dynamics, giving more relevance to the guidance issues.

As introduced in chapter 12 of [30], concerning the path planning techniques there are two main approaches: *deliberative* and *reactive* motion planning. While the former deals with the generation of well-defined paths and trajectories in completely known environments, the latter accounts for the dynamic environments, where the information is incomplete or uncertain. In the previous chapter of [30], some simple approaches are presented for waypoint based guidance, where the Dubins paths [31] are used to generate the shortest path between two configurations – steady planar positions with specific headings.

Other available methods for path planning consider the problem of the speed differential between the UAV and that of the target, adjusting the generated path to the target mean speed. In [32], two classes of flight trajectories are proposed for tracking moving targets, one consisting only on switching between clockwise and counter-clockwise orbits, and the other alternating between straight lines and circular orbits. Similarly, two modes are proposed in [33]: a sinusoidal trajectory for faster targets, and circular or rose curve orbits allowing to loiter around slowly-moving targets. Instead of generating different types of trajectories according to the speed of the target, [34, 35] propose solutions that are able to adapt to all speeds, from stationary to a full speed target – at most equaling the UAV maximum speed. In [34], an oscillatory motion is imposed to the UAV around a center of oscillation, and a less constrained system is derived – with some restricting assumptions – in order to favour its control. A similar oscillatory motion is considered in [35]. Here a reference point is generated around the target, modeled with the same dynamics as the UAV – ensuring a feasible trajectory –, and then a control law is presented in order to lead the UAV to converge to and track the reference point.

Regarding the problem of trajectory tracking, where a control system should command the vehicle to converge to the desired reference trajectory, several approaches are available in literature. While it is a trivial problem for fully actuated systems, it is a challenging problem for underactuated vehicles such as fixed-wing UAVs or other nonholonomic-like vehicles. For instance, the work in [36] addresses the position tracking control of underactuated rigid bodies on SE(3). A more technical literature review on this topic will be held later in the Control Chapter 3.

A slightly different subject is the path following problem. Here the goal is the convergence to a predefined path, with no time constraints. The problem can be adapted to a target tracking problem [37], where the purpose is to follow a circumference which moves together with the target. The method presented in [38] employs a Lyapunov based guidance vector field concept, enabling the tracking of a circular orbit or other closed orbit patterns, and can be adapted to several unmanned aircraft applications.

A more complex path following method is developed in [39]. Here, not only the full nonlinear dynamics model of the UAV is derived, but also the coordinated turn maneuver constraints are considered in a 3-D path following problem. A path-dependent error dynamic model is derived, and an output tracking error is defined, attaching the errors of the path-following and coordinated turn constraints, with the error convergence to zero ensuring the compliance of both problems.

A related line of research is concerned with the UAV vision-based target tracking. In [40], a fixed angle camera is used, and a guidance strategy is proposed to follow a constant-speed target. Using the position and velocity of the target obtained from the video image as feedback, appropriate control laws are derived to fix the target in the image frame while minimizing the standoff distance. Other authors consider a pan-tilt gimbaled camera, performing the autonomous tracking of a moving target while estimating its global position, velocity and heading [41, 42, 43]. In [41], relative kinematics is derived, relating the UAV and target headings and also the gimbal pan angle. Additionally, a Linear Parameter-Varying (LPV) filter is used for target motion estimation. In [43], a similar approach is presented, with the employment of the $\mathcal{L}_1$ fast adaptive estimator [44] for the target velocity estimation.

Further work has been developed on the vision-based target geolocation using UAVs [45, 46]. Using the pixel coordinates gathered from video processing algorithms, along with the video camera parameters, the UAV position and attitude, and the gimbal angles, the three-dimensional location of the target in inertial coordinates can be estimated. Moreover, some authors present optimal control techniques to minimize the error in the estimation error, by means of the generation of optimal trajectories for only one [47] or two coordinated UAVs [48].

While most of the previous approaches for target tracking consider only constant-velocity targets, other solutions introduce some techniques to deal with unexpected changes in the target motion. In [49], the standoff tracking problem is solved by using stochastic optimal control. The target is modeled

as a Brownian particle, and a control policy aims to minimize the expected value of a cost function based on the total squared distance error over an infinite horizon. In [50], the authors also consider an unpredictable motion of the ground target, adding some camera visibility restrictions, and two novel optimization-based control strategies are proposed. While one considers a similar stochastic problem as the previous author, the other goes further and assumes an evasive target motion, by means of a game theoretic approach. Even if the target has not an evasive behavior, stating the problem in this manner leads to a strongly robust control policy for unpredictable changes in the target velocity.

Additionally to the previous developments, remarkable work has been done on the coordination of multiple UAVs to perform cooperative target tracking and localization, with some techniques depicted in [51, 52, 53]. A more recent work applies Model Predictive Control (MPC) with Moving Horizon Estimation (MHE) in order to solve the stated optimal control problem [54, 55].

1.3 Mission Description

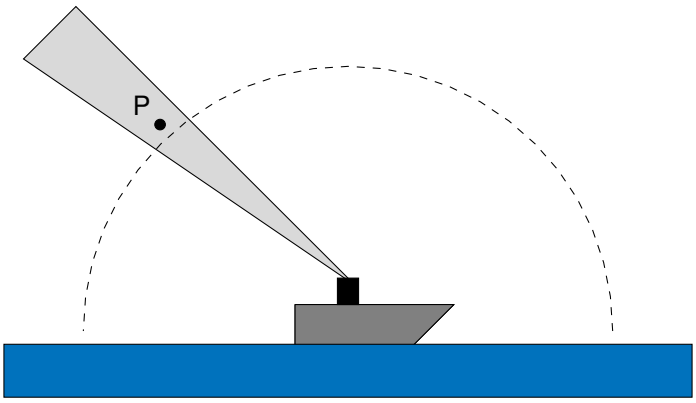

Figure 1.2: Representation of the keep-out area (dashed line) around the vessel and the desired smoke plume measurement point P

As this particular problem of the UAV-based monitorization of marine vessels gas emissions is still an emerging concern, there are few indications on the best way to guide the UAV to follow the vessels smoke plume and to perform the gas concentration measurements. The baseline for the definition of the mission conditions will be the best practices compilation reported in [5]. This report follows from the CompMon Sub-activity 4.6, and collects a series of recommendations for the airborne monitoring of ship plumes, aiming for a more efficient and safer operation.

In the above-mentioned publication [5], different types of sensor systems available for the airborne measurement of vessel emissions and subsequent calculation of the FSC are presented. In the present work, the mini-sniffer sensor is considered, being a lightweight, low-cost sensor, capable of detecting the FSC with high precision. In order for the mini-sniffer sensor to operate properly, the UAV must get into physical contact with the smoke plume, collect a sample of the smoke through a gas inlet, and then the gas sensors will take some time to process and to estimate the concentrations of CO_2, SO_2 and NO_x. Moreover, several consecutive measurements should be performed, in order to provide a better estimate of the gas concentrations.

Therefore, the UAV should be able to fly through the smoke plume several consecutive times with a certain periodicity, preferably in a region close to the vessel, which is where the gas concentrations are higher. Additionally, for safety reasons, the UAV should maintain a minimum distance to the vessel, and thus, a keep-out area around the vessel is considered. The UAV should be able to remain outside of this region all the times. The stated problem is illustrated in Figure 1.2, with the keep-out area represented by a dashed line around the vessel, and the desired point to perform the smoke plume measurement denoted by P.

Considering a proper UAV autonomous operation, a guidance system should be designed in order to guide the UAV to a suitable trajectory to comply with the previously stated objectives and restrictions, being able to track a slower vessel with a well-considered flight approach to the smoke plume.

1.4 Contributions and Organization of the Dissertation

Considering a general view of the current trends in airborne monitorization of marine vessel gas emissions, the main objective of this dissertation is the development of a Guidance and Control System for a fixed-wing UAV, allowing for the tracking of a marine vessel, more precisely of its smoke plume.

In order to achieve this primary objective, the following main contributions are provided in this dissertation:

- Generation of enhanced trajectories for constant speed vehicles with nonholonomic constraints, for the tracking of slow moving targets, enabling for successive crossings through a specific point in the target reference frame
- Definition of globally stable error formulation for the tracking control problem of nonholonomic vehicles, which eliminates the singularity inherent to a line-of-sight control approach

As part of the work carried out to accomplish the main objectives, this dissertation has other minor contributions:

- Review of the state-of-the-art on the following topics:
  - Smoke plume detection and/or localization
  - UAV-based target tracking
  - Tracking control of nonholonomic vehicles
- Application of Lyapunov-based methods for nonlinear systems stabilization
- Employment of a nonlinear cascade system approach to achieve global stability of the controlled system
- In-depth assessment of the influence of the design control parameters in the performance of the controlled system

In order to achieve the proposed goals, this dissertation is structured into 5 chapters, including this introduction, as follows:

Chapter 2 is devoted to the description of the guidance system (trajectory planning), generating a reference point with a suitable desired trajectory for the UAV to follow the moving vessel, considering all the stated objectives and restrictions. The relevant reference frames are introduced, as well as the considered simplified vehicle dynamics.

Chapter 3 is dedicated to the development of a control system (trajectory tracking) to steer the UAV to converge to the reference trajectory provided by the system of chapter 2. A generalized error formulation is proposed, applicable to the trajectory tracking problem of any kind of nonholonomic vehicles. A nonlinear control law is designed, and global asymptotic stability of the controlled system is achieved using the stability theory of Lyapunov.

Chapter 4 entails the implementation of the overall Guidance and Control System developed in the previous chapters and presents an in-depth analysis of its performance through a series of simulations. Sufficient conditions for a suitable trade-off between control effort and convergence rate are provided, and the system response to some typical perturbations is assessed. A final three-dimensional simulation is performed, with the UAV tracking to the vessel, sustaining the successful achievement of the mission goals and restrictions.

Chapter 5 contains the conclusions, critical remarks, and future work directions to support this dissertation.

Chapter 2

Guidance

The main objective in this chapter is the development of a guidance system which should be able to generate a reference trajectory for a fixed-wing UAV to follow a slower target – in this case a vessel. Given the speed differential between both vehicles, the reference trajectory should be able to keep track with the vessel, having its mean speed over time equivalent to the vessel speed, and should also be adjustable to any vessel speed, from zero up to the UAV speed. The generated trajectory should cross the smoke plume periodically as close as possible to the vessel, while respecting the minimum allowable distance to the vessel, so as to allow for the gas measurements. Hence, the generated trajectory should be: i) feasible by the UAV, ii) adjustable to different vessel speeds, and iii) outside and near the keep-out area around the vessel, flying through the smoke plume.

2.1 Problem statement

Based on the literature review of Section 1.2, on the existing target tracking techniques, the solution adopted in this study, in order to accomplish the proposed mission requirements, is described. It is noted that the considered target tracking problem is not trivial, as the fixed-wing UAV shall keep a constant speed for proper operation, while the target vessel is usually significantly slower.

The solution that seems to be most suitable is a path planning technique, where a virtual reference point is generated with the desired trajectory for the UAV, complying with the mission restrictions. This way a well-defined trajectory can be designed to cross the smoke plume in the desired point while respecting the minimum allowed distance to the vessel. Then a control law can be designed to command the UAV to converge to and track the reference point.

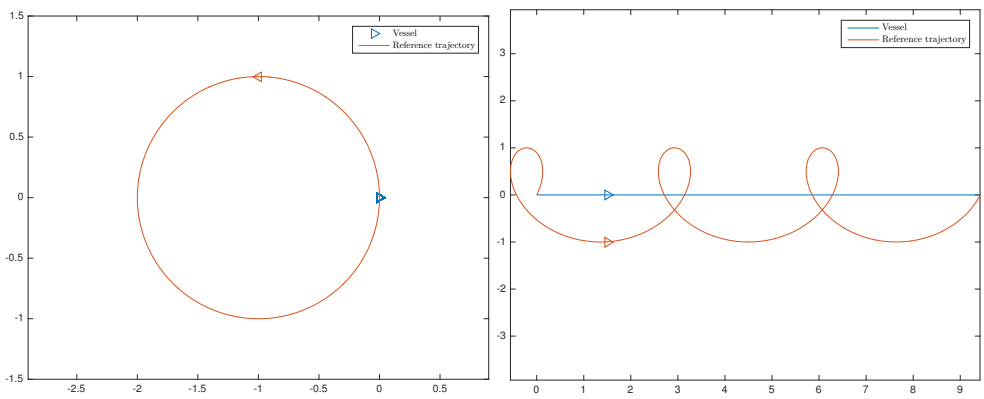

(a) Static vessel (b) Vessel with nonzero constant speed

Figure 2.1: Generation of a reference point with a circular trajectory relative to the vessel

Considering a static vessel, the simplest trajectory to fit the requirements is a circular reference trajectory, including the desired point in the smoke plume, such as the one illustrated in Figure 2.2a – considering a vertical smoke plume. However, when the vessel starts moving, if we consider a circular

reference trajectory relative to the vessel, it would not satisfy the UAV maximum heading rate, as it can be observed in Figure 2.2b.

One should find a proper reference trajectory that can be valid for a wide range of possible vessel speeds, while respecting the dynamics of the UAV. Recalling the work done in [34] and [35], the proposed oscillatory motion seems to have the potential to comply with the presented requirements, and mainly the ideas of [35] will be exploited in this chapter.

2.2 Reference Frames and Vehicle Dynamics

In order to define the equations of motion of the vehicles and the reference point, several reference frames are introduced. The inertial reference frame $\{I\}$ is an Earth-fixed reference frame with its origin placed in the initial position of the Center of Oscillation (CO), which will be formally defined in the following section, and East North Up (ENU) orientation. Denoting the reference axes by X_I, Y_I and Z_I, the $X_I - Y_I$ plane is tangent to the surface of the Earth in the origin. The X_I axis points towards East and Y_I towards North. The Z_I axis is perpendicular to the Y_I and X_I axes and points up, in the opposite direction of the center of the Earth.

A body-fixed reference frame $\{B\}$ is also defined, with origin in the center of mass of the UAV and the X_B axis aligned along its longitudinal axis, pointing towards the nose of the airframe. The Y_B axis points out the left wing and the Z_B axis points in the upper direction.

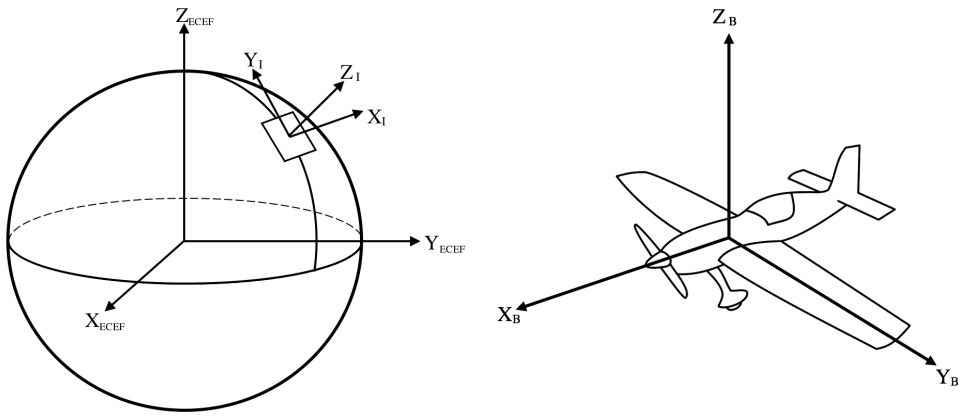

(a) Inertial Reference Frame $\{I\}$

(b) UAV body-fixed Reference Frame $\{B\}$

Figure 2.2: Main Reference Frames

A similar reference frame is also defined as $\{V\}$, with its origin in the center of mass of the vessel. The axes X_V, Y_V and Z_V are aligned relatively to the vessel in the same way as the corresponding axes of the reference frame $\{B\}$ are aligned relatively to the UAV.

The transformation between reference frames can be defined by a translation and a rotation. Considering the position of an arbitrary point represented in the inertial reference frame, $\mathbf{s}^I$, the position of that same point can be represented in the body-fixed reference frame through the transformation

$$\mathbf{s}^B = \mathbf{r}^I + \mathcal{R}_I^B(\psi, \theta, \phi)\mathbf{s}^I, \tag{2.1}$$

where $\mathbf{r}^I$ is the UAV position in the inertial reference frame, and $\mathcal{R}_I^B$ is a rotation matrix from the inertial to the body-fixed reference frames. The yaw (ψ), pitch (θ) and roll (ϕ) angles are the so-caled Euler angles, which are widely used in aeronautics, providing an intuitive means of representing the three-dimensional orientation of a body. These angles are defined by consecutive right-handed rotations, and several different Euler angle systems exist [56], each of which having a different rotation sequence. The most used rotation sequence for describing the aircraft attitude is derived in [30] and is given by

$\mathcal{R}_3(\psi) \to \mathcal{R}_2(\theta) \to \mathcal{R}_1(\phi)$. The resulting rotation matrix is given by

$$\begin{aligned}
\mathcal{R}_B^I(\phi,\theta,\psi) &= \mathcal{R}_3(\psi)\mathcal{R}_2(\theta)\mathcal{R}_1(\phi) \\
&= \begin{bmatrix} \cos\psi & -\sin\psi & 0 \\ \sin\psi & \cos\psi & 0 \\ 0 & 0 & 1 \end{bmatrix} \begin{bmatrix} \cos\theta & 0 & \sin\theta \\ 0 & 1 & 0 \\ -\sin\theta & 0 & \cos\theta \end{bmatrix} \begin{bmatrix} 1 & 0 & 0 \\ 0 & \cos\phi & -\sin\phi \\ 0 & \sin\phi & \cos\phi \end{bmatrix} \\
&= \begin{bmatrix} \mathsf{c}\theta\mathsf{c}\psi & \mathsf{s}\phi\mathsf{s}\theta\mathsf{c}\psi - \mathsf{c}\phi\mathsf{s}\psi & \mathsf{c}\phi\mathsf{s}\theta\mathsf{c}\psi + \mathsf{s}\phi\mathsf{s}\psi \\ \mathsf{c}\theta\mathsf{s}\psi & \mathsf{s}\phi\mathsf{s}\theta\mathsf{s}\psi + \mathsf{c}\phi\mathsf{c}\psi & \mathsf{c}\phi\mathsf{s}\theta\mathsf{s}\psi - \mathsf{s}\phi\mathsf{c}\psi \\ -\mathsf{s}\theta & \mathsf{s}\phi\mathsf{c}\theta & \mathsf{c}\phi\mathsf{c}\theta \end{bmatrix},
\end{aligned} \tag{2.2}$$

where $\mathsf{c}\phi \triangleq \cos\phi$ and $\mathsf{s}\phi \triangleq \sin\phi$. An analogous method is used for the transformation from the inertial to the vessel reference frame.

A complete six-degree-of-freedom dynamic model of a fixed-wing UAV is derived in [30], relating the 12-state variables of a rigid-body, including three position states and three velocity states for the translational motion, and three angular position and three angular velocity states for the rotational motion. Also, the forces and moments acting on a UAV are described, mainly due to the gravity, aerodynamics and propulsion. Further analyse can be performed, in order to design control laws to find the required action on the thrust and on the control surfaces – ailerons, rudder, and elevator –, in order to achieve a stable flight operation, being able to command the aircraft to the desired attitude.

The main purpose in this dissertation is the design of higher-level guidance strategies in order to get the desired attitude commands to be handled by existing low-level controllers, implemented in common commercial autopilots. Here a simplified kinematics motion is considered, and the aircraft is considered to be aligned with its velocity vector, with null values of the roll and pitch angles, as well as null flight path angle, γ, and null sideslip angle β. The low-level controller should be responsible for ensuring that the reference attitude commands are tracked. For more detailed equations of motion of UAVs, the reader is refered to [30]. The kinematics model for the UAV motion representation consider only a two-dimensional motion, in the horizontal plane with altitude h. Hence, the UAV attitude is considered to be $(\psi,\theta,\phi) = (\chi,0,0)$, where χ stands for the UAV heading, and represents the direction of the velocity vector. Thus, the rotation matrix (2.2) simplifies for a right-handed rotation around the Z_I axis by an angle χ, becoming

$$\mathcal{R}_B^I(\chi,0,0) = \mathcal{R}_3(\chi) = \begin{bmatrix} \cos\chi & -\sin\chi & 0 \\ \sin\chi & \cos\chi & 0 \\ 0 & 0 & 1 \end{bmatrix}. \tag{2.3}$$

The simplified kinematics motion of the UAV is then given by

$$\dot{\mathbf{x}} = \begin{cases} \dot{x} = v\cos(\chi) \\ \dot{y} = v\sin(\chi) \\ \dot{\chi} = \omega \end{cases} \tag{2.4}$$

where v and ω are the commanded speed and heading rate, respectively, that will be given to the inner-loop control, along with the desired altitude h. The desired speed of the UAV will be denoted as V_r and is considered to be the optimal speed for a cruise flight condition. This dynamic is commonly used in the UAV literature, and is known as a Dubins vehicle model [31, 30]. Additionaly this is also considered as a nonholonomic vehicle, as it satisfies the nonholonomic constraint

$$\dot{x}\sin\chi - \dot{y}\cos\chi = 0. \tag{2.5}$$

An important restriction that should be taken in consideration during the guidance and control system design is the UAV maximum heading rate ω_{max}, that is the maximum absolute value of u that can be attained by the UAV, and is constrained by the minimum turn radius.

Similarly, the dynamics motion of the vessel can also be defined with the same motion of the UAV, by

$$\dot{\mathbf{x}}_V = \begin{cases} \dot{x}_\mathsf{V} = V_\mathsf{V} \cos(\chi_\mathsf{V}) \\ \dot{y}_\mathsf{V} = V_\mathsf{V} \sin(\chi_\mathsf{V}) \\ \dot{\chi}_\mathsf{V} = \omega_V \end{cases} \tag{2.6}$$

where the vessel speed V_V is considered to vary in the range $V_V \in [0, V_\mathsf{r}]$, with a relatively low acceleration, and the vessel heading rate ω_V is considered to be significantly lower than the one of the UAV. These assumptions of low linear acceleration and low heading rate for the vessel are reasonable, since the vessels considered in this mission are mostly very large, travelling in cruise speed for a long time, and having very low course deviations. Nevertheless, in the Simulations Chapter 4, the proposed algorithms will be evaluated also in the case V_V changes faster than expected, in order to show that the same conclusions apply.

2.3 Proposed guidance solution

Given that the dynamics of the vehicles are introduced, the adopted guidance solution can be properly described. Recalling the former problem of tracking a vessel with a fixed-wing UAV, it should ideally fly through the vessel smoke plume several consecutive times, being the closest possible to the vessel, where the gas concentrations are higher, but always respecting a minimum distance to the vessel.

Firstly, the concept of Center of Oscillation (CO) is introduced. The CO is the virtual point to be placed in the smoke plume measurement site. This point is fixed in the vessel reference frame as long as the vessel keeps a constant velocity. The positioning of the CO will be addressed later in this chapter.

Secondly, the reference point with position coordinates given by (x_r, y_r) is introduced. The reference point will be virtually generated with the desired motion of the UAV, and can be seen as the desired point where the UAV should be at each time instant. The reference point motion is based on the oscillatory heading rate solution presented in [35], and can be modeled in the inertial reference frame as

$$\dot{\mathbf{x}}_r = \begin{cases} \dot{x}_\mathsf{r} = V_\mathsf{r} \cos(\chi_\mathsf{r}) \\ \dot{y}_\mathsf{r} = V_\mathsf{r} \sin(\chi_\mathsf{r}) \\ \dot{\chi}_\mathsf{r} = -A \sin(\omega_0 t + \phi_0) + \omega_V \end{cases} \tag{2.7}$$

where V_r is the desired UAV speed to be regulated by the autopilot and ω_V is the vessel heading rate. The initial position of the reference point will be coincident with the CO, and the former will have an oscillatory motion around the latter. The scalar parameter A, as well as the frequency ω_0 and phase ϕ_0 of the oscillatory motion should be tuned in order to adjust the reference point motion relative to the CO, which by definition coincides with the motion of the vessel. The method devised to select the parameters is detailed in the following section.

2.4 Analysis of the oscillation parameters

In order to better understand the behaviour of the reference point motion, the third equation in (2.7) is integrated to obtain an expression for the reference heading over time. For this analysis, the vessel is considered to move with a constant velocity, having the constant speed V_V and the constant heading χ_V, leading to $\omega_V = 0$. Assuming that $\chi_\mathsf{r}(0) = A/\omega_0$,

$$\chi_\mathsf{r}(t) = \int_0^t \left[-A \sin(\omega_0 \tau + \phi_0)\right] d\tau = \frac{A}{\omega_0} \cos(\omega_0 t + \phi_0). \tag{2.8}$$

For simplicity in this study, a new parameter is defined as $\eta = A/\omega_0$. Substituting (2.8) into the first and second equations of (2.7), one obtains

$$\begin{cases} \dot{x}_\mathsf{r}(t) = V_\mathsf{r} \cos\left[\eta \cos(\omega_0 t + \phi_0)\right] \\ \dot{y}_\mathsf{r}(t) = V_\mathsf{r} \sin\left[\eta \cos(\omega_0 t + \phi_0)\right] \end{cases}. \tag{2.9}$$

In order to better understand the behaviour of both reference coordinates in time, functions $\dot{x}_{\mathsf{r}}(t)$ and $\dot{y}_{\mathsf{r}}(t)$ are represented in Figure 2.3, for $\eta = 1$, $\omega_0 = 1$ rad/s, $\phi_0 = 0$ rad and considering unitary speed $V_r = 1$ m/s, in the time span $t = [0, T]$, where T is the oscillation period, $T = 2\pi/\omega_0 = 2\pi$ s.

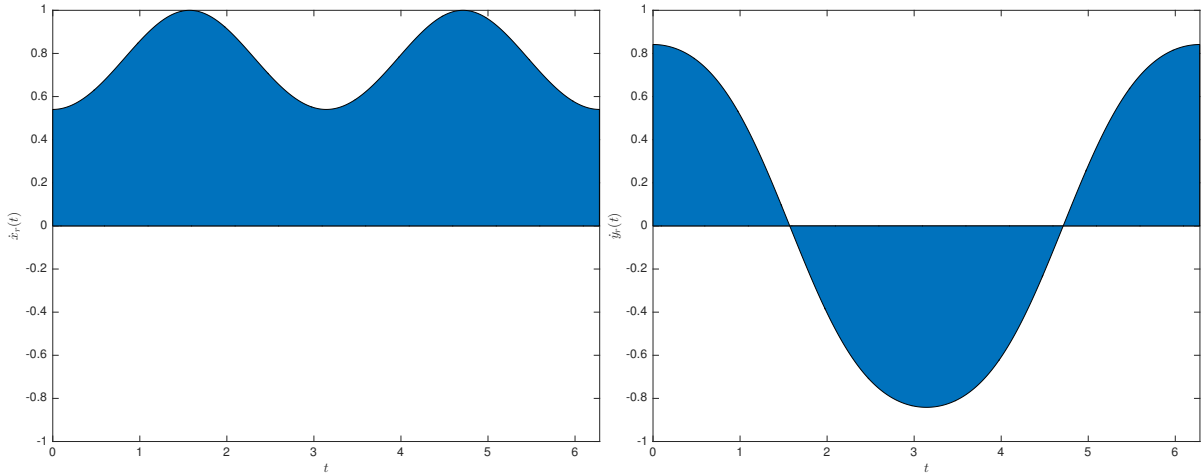

(a) Derivative of x_{r} (b) Derivative of y_{r}

Figure 2.3: Derivative of the coordinates of the reference point over time

In Figure 2.3 the distance traveled by the reference point in a period T corresponds to the area of the regions filled in blue, in each direction, X_I and Y_I. Therefore, one can see that, with this oscillatory heading solution, the reference point will advance in the X_I axis direction, while oscillating around the Y_I axis.

Hence, considering a constant vessel speed, one can force the reference point to follow the vessel by adequately defining the average speed of the reference point over an oscillation period T. The mean speed of the reference point in a period T is given by

$$\begin{cases} \bar{\dot{x}}_{\mathsf{r}}(t) & = \frac{1}{T}\int_0^T \dot{x}_{\mathsf{r}}(t)\,dt = V_{\mathsf{r}}\frac{1}{T}\int_0^T \cos\left[\eta\cos\left(\omega_0 t\right)\right]dt \\ \bar{\dot{y}}_{\mathsf{r}}(t) & = \frac{1}{T}\int_0^T \dot{y}_{\mathsf{r}}(t)\,dt = V_{\mathsf{r}}\frac{1}{T}\int_0^T \sin\left[\eta\cos\left(\omega_0 t\right)\right]dt \end{cases} \tag{2.10}$$

Let the ratio between vessel and reference speeds be given by $\nu = V_{\mathsf{V}}/V_{\mathsf{r}}$ and define the function

$$F(\eta) = \frac{1}{T}\int_0^T \cos\left[\eta\cos\left(\omega_0 t\right)\right]dt. \tag{2.11}$$

Then, having a mean speed of the reference point over a period equal to the vessel speed is equivalent to

$$\begin{aligned} V_{\mathsf{V}} &= \bar{V}_{\mathsf{r}} \\ \Leftrightarrow V_{\mathsf{V}} &= \sqrt{\left(\bar{\dot{x}}_{\mathsf{r}}\right)^2 + \left(\bar{\dot{y}}_{\mathsf{r}}\right)^2} \\ \Leftrightarrow V_{\mathsf{V}} &= V_{\mathsf{r}}\sqrt{\left[F\left(\eta\right)\right]^2 + 0} \\ \Leftrightarrow \nu &= \left|F(\eta)\right|. \end{aligned} \tag{2.12}$$

Given the periodic properties of the trigonometric functions $\sin$ and $\cos$, function $F(\eta)$ can be seen as a different representation of the Bessel function of the first kind and zero order[1], $J_0(\eta)$, in its integral form, represented by (2.13) which is depicted in Figure (2.4).

$$J_0(\eta) = \frac{1}{\pi}\int_0^{\pi} \cos\left[\eta\sin\left(t\right)\right]dt = \frac{1}{2\pi}\int_0^{2\pi} \cos\left[\eta\sin\left(t\right)\right]dt = F(\eta). \tag{2.13}$$

[1] Throughout this dissertation, we will refer to the Bessel function of the first kind and zero order, only as Bessel function.

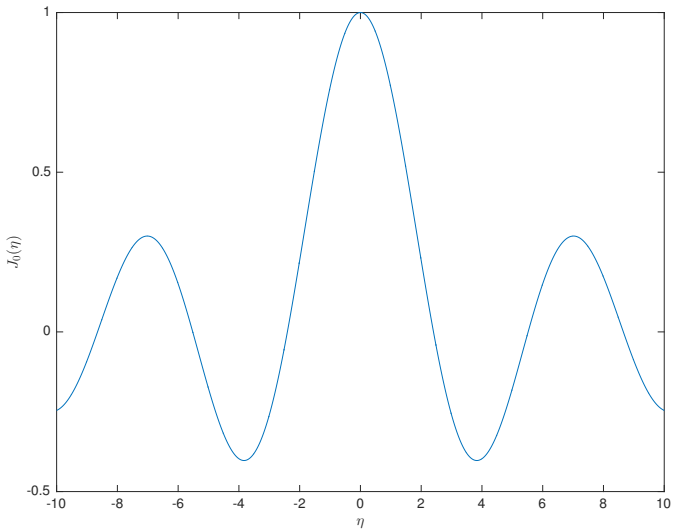

Figure 2.4: Representation of the Bessel function of the first kind and zero order, $J_0(\eta)$

From (2.12), a relation between the speed ratio ν and parameter η is found. Therefore, this parameter η can be used to adjust the reference point mean speed in the X_I axis direction to the vessel speed, which requires the computation of the inverse of the Bessel function. From Figure 2.4 one can see the Bessel function is non-invertible in its full domain. However, in the problem at hand, it can be considered that the speed ratio is given by $\nu \in [0, 1]$, which covers the range from having a static vessel to having a vessel with the same speed as the UAV. The Bessel function $J_0(\eta)$ can then be inverted in a restrict domain between $\eta = 0$ and its first positive zero. The first positive zero of $J_0(\eta)$ can be found numerically, and is $\eta \approx 2.4048$.

Parameter η is then defined as a function of ν as

$$\eta(\nu) = J_0^{-1}(\nu). \tag{2.14}$$

It is highlighted that, in order to achieve the desired mean motion along the X_I axis, the initial heading of the reference point should be set according to $\chi_\mathrm{r}(t=0) = \Big[\eta \cos(\omega_0 t + \phi_0)\Big]_{t=0} = \eta \cos \phi_0$.

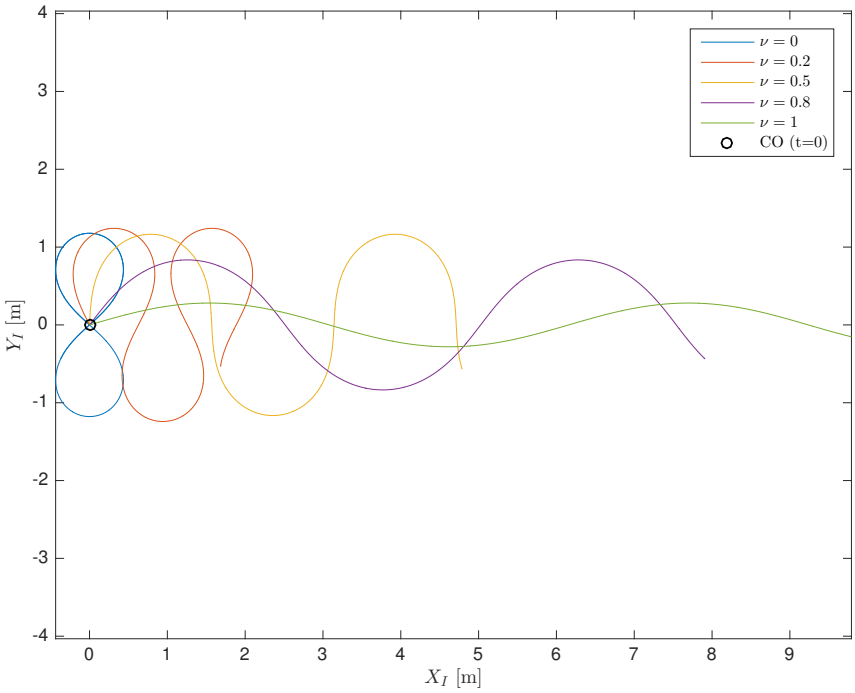

Figure 2.5: Generated reference trajectories for different values of the speed ratio, ν, considering an unitary reference speed $V_\mathrm{r} = 1$ m/s, $\omega_0 = 1$ rad/s and $\phi_0 = 0$ rad

As observed in Figure 2.5, when the vessel is stationary, the reference point describes a Lemniscate of Bernoulli around the CO. For higher values of the speed ratio, the heading motion of the reference point is adjusted so that it can fly over the CO every period $T/2 = \pi/\omega_0$. In the case the vessel has the same speed as the reference point, the latter flies directly over the former, as naturally expected.

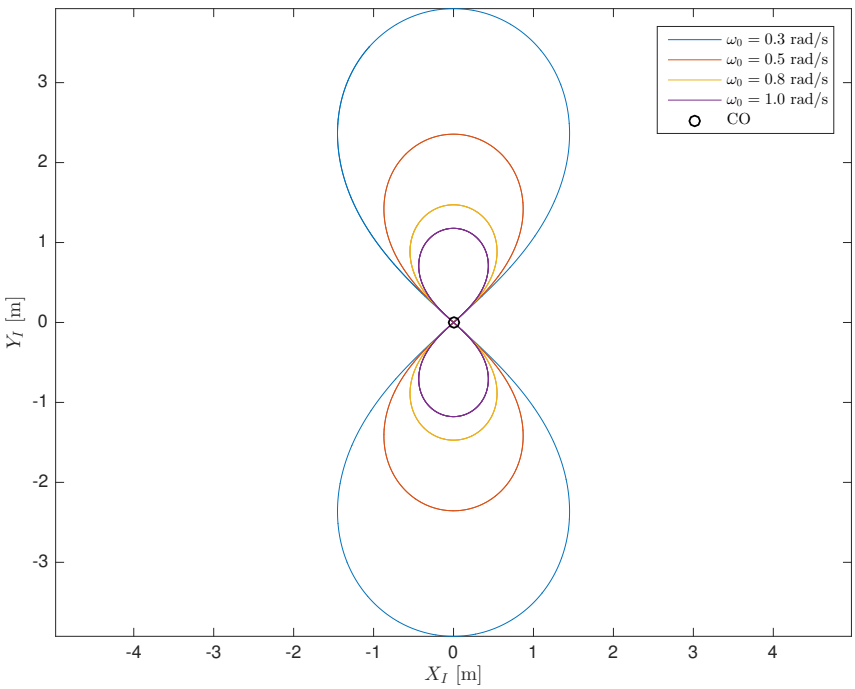

Figure 2.6: Generated reference trajectories for different values of the oscillation frequency ω_0, considering an unitary reference speed, $V_\mathrm{r} = 1$ m/s, a static vessel, $\nu = 0$ and $\phi_0 = 0$ rad

Now that the reference point is able to follow the vessel motion through the tuning of variable η, another important constraint should be considered, that is the UAV maximum heading rate ω_max. Recalling the heading rate equation of the reference point (2.7), this restriction can be imposed by

$$|\dot{\chi}_\mathrm{r}| \leq \omega_\mathrm{max} \Rightarrow |A \sin(\omega_0 t + \phi_0) + \omega_V| \leq \omega_\mathrm{max} \Rightarrow A + |\omega_V| \leq \omega_\mathrm{max}. \tag{2.15}$$

Therefore, to ensure the heading rate of the reference point is always achievable by the UAV, the oscillation frequency, ω_0, shall satisfy

$$\omega_0 \leq \frac{\omega_\mathrm{max} - |\omega_V|}{\eta(\nu)}. \tag{2.16}$$

In Figure 2.6, the generated reference trajectories for different values of the oscillation frequency ω_0 are represented, for a static vessel. For smaller values of ω_0 it is noted that the trajectory will have a greater amplitude, as $\eta = A/\omega_0$, thus having a higher period of oscillation and a higher maximum distance to the CO. Therefore, there is a tradeoff between the value of ω_0 and the time between consecutive crossings over the CO. Parameter ω_0 should be small enough for the generated trajectory to be attained by the UAV, but sufficiently large so that the time between CO crossings can be minimized.

The remaining parameter to be considered is the oscillation phase, ϕ_0. This parameter can be used to fix the initial position of the reference point in a different position of the periodic trajectory, i.e., the CO can be positioned in a different point of the generated trajectory, other than the center of the Lemniscate of Bernoulli – when considering a static vessel $\nu = 0$. However, this parameter will be used later in the CO positioning section 2.6.

2.5 Maximum distance between the reference point and the CO

In this section, the maximum distance achieved between the reference point trajectory and the CO will be computed so that it can be later used in the CO Positioning. From its definition, the CO will have

the same motion of the vessel, as it is fixed in $\{V\}$ for constant vessel speed and constant wind. When vessel speed variations occur, the CO will be placed accordingly, as described in the following section 2.6. Thus, the CO motion can be represented as

$$\dot{\mathbf{x}}_{\mathsf{CO}} = \begin{cases} \dot{x}_{\mathsf{CO}} & = V_{\mathsf{CO}} \cos(\chi_{\mathsf{CO}}) \\ \dot{y}_{\mathsf{CO}} & = V_{\mathsf{CO}} \sin(\chi_{\mathsf{CO}}) \\ \dot{\chi}_{\mathsf{CO}} & = \omega_{\mathsf{CO}} \end{cases}. \tag{2.17}$$

The CO velocity vector, represented by V_{CO} and ω_{CO}, can be assumed to be approximately equal to that of the vessel, $V_{\mathsf{CO}} \approx V_{\mathsf{V}}$ and $\omega_{\mathsf{CO}} \approx \omega_V$. This approximation is deemed valid, because the direction of the smoke plume is considered to always have the same direction, even when the vessel is turning. Now equations (2.17) can be integrated in order to obtain the CO position coordinates over time. For constant velocities, we obtain

$$\mathbf{x}_{\mathsf{CO}}(t) = \begin{cases} x_{\mathsf{CO}}(t) & = V_{\mathsf{V}} \frac{\sin(\omega_{\mathsf{V}} t)}{\omega_{\mathsf{V}}} \\ y_{\mathsf{CO}}(t) & = V_{\mathsf{V}} \frac{\left[1-\cos(\omega_{\mathsf{V}} t)\right]}{\omega_{\mathsf{V}}} \\ \chi_{\mathsf{CO}}(t) & = \omega_{\mathsf{V}} t \end{cases}. \tag{2.18}$$

Note that the integration constants are set according to the definition of the inertial coordinate frame, where the initial position of the CO is the origin, i.e., $\mathbf{x}_{\mathsf{CO}}(t=0) = \big(x_{\mathsf{CO}}, y_{\mathsf{CO}}, \chi_{\mathsf{CO}}\big)(t=0) = (0,0,0)$.

2.5.1 Constant Velocity

In this subsection, the maximum distance between the reference point and the CO is calculated, considering the case when the vessel moves with constant velocity V_{V}, leading to $\chi_{\mathsf{CO}}(t) \equiv \omega_{\mathsf{V}}(t) \equiv 0$.

In this particular case with $\omega_{\mathsf{V}} = 0$, it is possible to notice that the CO position coordinates in (2.18) are not well defined. In order to see what happens when $\omega_{\mathsf{V}} = 0$, calculate the limits

$$\begin{cases} \lim\limits_{\omega_{\mathsf{V}} \to 0} x_{\mathsf{CO}} & = V_{\mathsf{V}} \lim\limits_{\omega_{\mathsf{V}} \to 0} \dfrac{\sin(\omega_{\mathsf{V}} t)}{\omega_{\mathsf{V}}} = \dfrac{0}{0} \\ \lim\limits_{\omega_{\mathsf{V}} \to 0} y_{\mathsf{CO}} & = V_{\mathsf{V}} \lim\limits_{\omega_{\mathsf{V}} \to 0} \dfrac{[1-\cos(\omega_{\mathsf{V}} t)]}{\omega_{\mathsf{V}}} = \dfrac{0}{0} \end{cases}. \tag{2.19}$$

In both cases an indetermination of the type $0/0$ is obtained, which can be solved using the L'Hôpital's rule as

$$\begin{cases} \lim\limits_{\omega_{\mathsf{V}} \to 0} x_{\mathsf{CO}} & = V_{\mathsf{V}} \lim\limits_{\omega_{\mathsf{V}} \to 0} \dfrac{t\cos(\omega_{\mathsf{V}} t)}{1} = V_{\mathsf{V}} t \\ \lim\limits_{\omega_{\mathsf{V}} \to 0} y_{\mathsf{CO}} & = V_{\mathsf{V}} \lim\limits_{\omega_{\mathsf{V}} \to 0} \dfrac{t\sin(\omega_{\mathsf{V}} t)}{1} = 0 \end{cases}. \tag{2.20}$$

The position coordinates of the CO over time become the trivial solution of a point moving in a straight line, with its velocity along the X_I axis direction.

Now considering the reference point, its position coordinates over time should also be obtained. Hence, substituting (2.8) in (2.7) one obtains

$$\begin{cases} x_{\mathsf{r}}(t,\nu) = \int_0^t V_{\mathsf{r}} \cos\left[\eta(\nu)\cos(\omega_0 \tau)\right] d\tau = V_{\mathsf{r}} F_{\mathsf{x}}(t,\nu) \\ y_{\mathsf{r}}(t,\nu) = \int_0^t V_{\mathsf{r}} \sin\left[\eta(\nu)\cos(\omega_0 \tau)\right] d\tau = V_{\mathsf{r}} F_{\mathsf{y}}(t,\nu) \end{cases} \tag{2.21}$$

where $F_{\mathsf{x}}(t,\nu) = \int \cos\left[\eta(\nu)\cos(\omega_0 t)\right] dt$ and $F_{\mathsf{y}}(t,\nu) = \int \sin\left[\eta(\nu)\cos(\omega_0 t)\right] dt$. The distance between the reference point and the CO over time is then given by

$$d(t,\nu) = \sqrt{\left[x_{\mathsf{r}}(t,\nu) - x_{\mathsf{CO}}(t)\right]^2 + \left[y_{\mathsf{r}}(t,\nu) - y_{\mathsf{CO}}(t)\right]^2}. \tag{2.22}$$

Now in order to find the maximum value of this distance, the time derivative should be computed and the time instants at which its derivative is zero should be evaluated from

$$\begin{aligned} \frac{d}{dt} d(t,\nu) = 0 \Rightarrow & \left[x_{\mathsf{r}}(t,\nu) - x_{\mathsf{CO}}(t)\right]\left[\dot{x}_{\mathsf{r}}(t,\nu) - \dot{x}_{\mathsf{CO}}(t)\right] + \left[y_{\mathsf{r}}(t,\nu) - y_{\mathsf{CO}}(t)\right]\left[\dot{y}_{\mathsf{r}}(t,\nu) - \dot{y}_{\mathsf{CO}}(t)\right] = 0 \\ \Leftrightarrow & V_{\mathsf{r}}^2 \left[F_{\mathsf{x}}(t,\nu) - \nu \cdot t\right]\left[\dot{F}_{\mathsf{x}}(t,\nu) - \nu\right] + V_{\mathsf{r}}^2 \left[F_{\mathsf{y}}(t,\nu) - 0\right]\left[\dot{F}_{\mathsf{y}}(t,\nu) - 0\right] = 0. \end{aligned} \tag{2.23}$$

Given the complexity of (2.23) and the difficulty to find analytically a time instant t that satisfies it, a more conservative way to find a bound for the distance is considered.

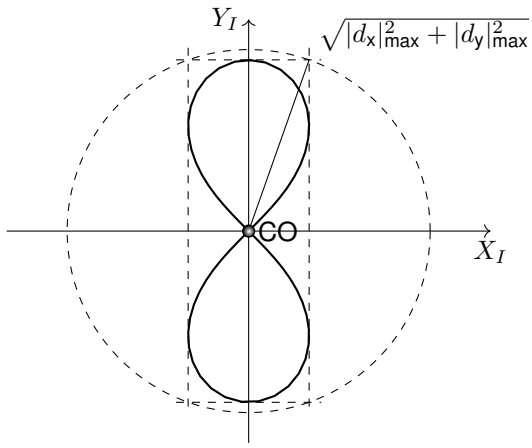

Figure 2.7: Representation of the considered conservative maximum distance between the reference point and the CO, for the speed ratio $\nu = 0$

Instead of finding the maximum value of the distance between the reference point and the CO, the maximum distances will be found separately in the X_I and Y_I coordinates, as represented in Figure 2.7. Therefore, we define

$$\begin{cases} d_{\mathsf{x}}(t,\nu) & = x_{\mathsf{r}}(t,\nu) - x_{\mathsf{CO}}(t) = V_{\mathsf{r}}\left[F_x(t,\nu) - \nu \cdot t\right] \\ d_{\mathsf{y}}(t,\nu) & = y_{\mathsf{r}}(t,\nu) - y_{\mathsf{CO}}(t) = V_{\mathsf{r}} F_y(t,\nu) \end{cases} . \tag{2.24}$$

A simulation is presented in Figure 2.8 with the generation of the reference trajectory for a straight line CO motion, with $\nu = 0.5$, during two periods, $2T$. In the bottom graphs of this figure, the equations (2.24) are represented, with the distances in the X and Y axes directions, in order to give a better understanding of the functions $F_{\mathsf{x}}(t)$ and $F_{\mathsf{y}}(t)$.

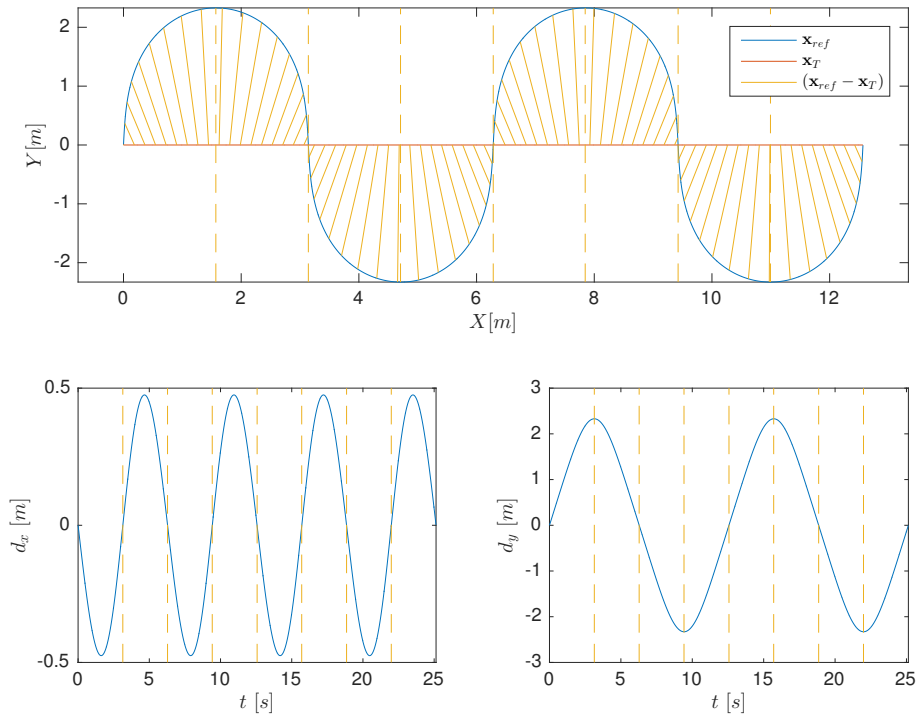

Figure 2.8: Representation of the distances between the reference point and the CO, in the X_I and Y_I axes directions, separately. Simulation during two oscillation periods $2T$, with $\nu = 0.5$.

Given the periodic properties of the sinusoidal functions involved, one can observe that $d_{\mathsf{x}}(t,\nu)$ has two maxima and two minima in a period T, all with the same absolute value. Similarly for $d_{\mathsf{y}}(t,\nu)$, there is one maximum and one minimum in a period T with the same value.

Now setting the derivatives of (2.24) to zero, the time instants in which the functions have their maximum absolute values are found,

$$\begin{cases} t_{\mathsf{x}}(\nu) & = \frac{1}{\omega_0}\arccos\left[\frac{1}{\eta}\arccos(\nu)\right] \\ t_{\mathsf{y}} & = \frac{\pi}{2\omega_0} \end{cases}. \tag{2.25}$$

The previous expression for the time instant in which the maximum distance in the X_I axis direction occurs is only valid for $\nu \neq 1$. For that particular case, parameter η is zero, and therefore the outter $\arccos$ function has no solution. However, in that case, with the speed of the reference point being the same as that of the CO, the distance is zero.

Now considering (2.24) at time instants t_{x} and t_{y} we obtain

$$\begin{cases} |d_{\mathsf{x}}(t,\nu)|_{\mathsf{max}} & = |d_{\mathsf{x}}(t_{\mathsf{x}}(\nu),\nu)| = V_{\mathsf{r}}\,|F_{\mathsf{x}}(t_{\mathsf{x}}(\nu),\nu) - \nu\cdot t_{\mathsf{x}}(\nu)| \\ |d_{\mathsf{y}}(t,\nu)|_{\mathsf{max}} & = |d_{\mathsf{y}}(t_{\mathsf{y}},\nu)| = V_{\mathsf{r}}\,|F_{\mathsf{y}}(t_{\mathsf{y}},\nu)| \end{cases}. \tag{2.26}$$

Therefore, for each speed ratio ν, it is proposed to ensure that the distance between the reference point and the CO never exceeds the following value

$$d_{\mathsf{max}}(\nu) = \sqrt{d_{\mathsf{x}}^2(t_{\mathsf{x}}(\nu),\nu) + d_{\mathsf{y}}^2(t_{\mathsf{y}},\nu)}. \tag{2.27}$$

Function $d_{\mathsf{max}}(\nu)$ is represented in Figure 2.9, where the upper bound of the distance between the reference point and the CO is shown depending on the speed ratio ν. Given the linear dependency of distance $d_{\mathsf{max}}(\nu)$ on the reference point speed V_{r}, the simulation presented in Figure 2.9 considers a unitary reference speed $V_{\mathsf{r}} = 1$ m/s. but Therefore, for higher reference speeds one can simply multiply the resulting distance in this figure by the considered speed.

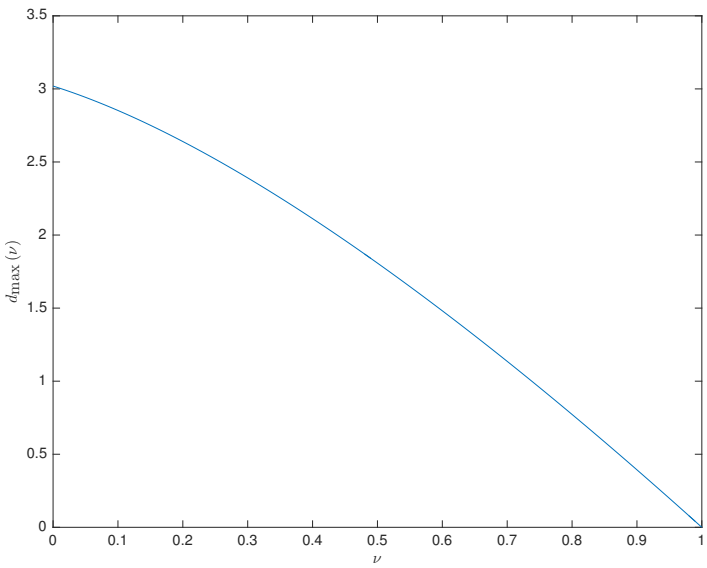

Figure 2.9: Representation of the maximum conservative distance between the reference point and the CO, for a constant velocity of the CO. The oscillation frequency ω_0 is calculated according to (2.16) so thatthe resulting amplitude A equate the UAV maximum heading rate ω_{max}.

2.5.2 Constant speed, constant heading rate

In this subsection, a similar study will be done, now considering a nonzero constant heading rate for the vessel ω_V, and thus for the CO. In order to generate reference trajectories suitable for a UAV, the CO heading rate ω_V should be much smaller than the UAV maximum heading rate ω_{max}, i.e., $\omega_V \ll \omega_{\mathsf{max}}$.

The CO coordinates over time are obtained from (2.18). The nonzero value of ω_V will be added to the third equation of (2.7), and the reference heading over time becomes

$$\chi_{\mathsf{r}}(t,\nu) = \eta(\nu)\cos(\omega_0 t) + \omega_V t. \tag{2.28}$$

Therefore, the reference position coordinates can be now written as

$$\begin{cases} x_{\mathsf{r}}(t,\nu) &= \int_0^t V_{\mathsf{r}} \cos\left[\eta(\nu)\cos(\omega_0\tau) + \omega_V\tau\right] d\tau = V_{\mathsf{r}} G_x(t,\nu) \\ y_{\mathsf{r}}(t,\nu) &= \int_0^t V_{\mathsf{r}} \sin\left[\eta(\nu)\cos(\omega_0\tau) + \omega_V\tau\right] d\tau = V_{\mathsf{r}} G_y(t,\nu) \end{cases} \tag{2.29}$$

where $G_x(t,\nu) = \int_0^t \cos\left[\eta(\nu)\cos(\omega_0\tau) + \omega_V\tau\right] d\tau$ and $G_y(t,\nu) = \int_0^t \sin\left[\eta(\nu)\cos(\omega_0\tau) + \omega_V\tau\right] d\tau$.

The relative distances in both coordinates are in this case given by

$$\begin{cases} d_{\mathsf{x}}(t,\nu) &= x_{\mathsf{r}}(t,\nu) - x_{\mathsf{T}}(t) = V\left[G_{\mathsf{x}}(t,\nu) - \nu\frac{\sin(\Omega t)}{\Omega}\right] \\ d_{\mathsf{y}}(t,\nu) &= y_{\mathsf{r}}(t,\nu) - y_{\mathsf{T}}(t) = V\left[G_{\mathsf{y}}(t,\nu) - \nu\frac{1-\cos(\Omega t)}{\Omega}\right] \end{cases} \tag{2.30}$$

Comparing functions G_{x} and G_{y} with F_{x} and F_{y}, one can expect a similar behaviour of the relative distance over time, now affected by the lower frequency term due to the heading rate extra component.

In Figure 2.10, a simulation is presented with the generated trajectory around the CO describing a circular trajectory. From this figure, one can conclude that the maximum distance can be calculated with the same method as for the constant heading vessel in the previous subsection, with the only difference in the value of ω_0 according to the vessel heading rate.

It is reinforced, however, that this guidance solution is only suitable for small values of the vessel heading rate ω_V. If larger values are considered, the reference point will not be able to maintain its mean motion around the CO. This limitation is due to the approximation made in the analysis of the parameter η, where a constant vessel heading was considered. For the purpose of this dissertation, this assumption is deemed valid, since the considered targets here are large vessels operating in cruise condition, which involves essentially straight line trajectories, with very low heading rates, when present. Therefore, for problems involving larger target heading rates, this analysis may not be valid.

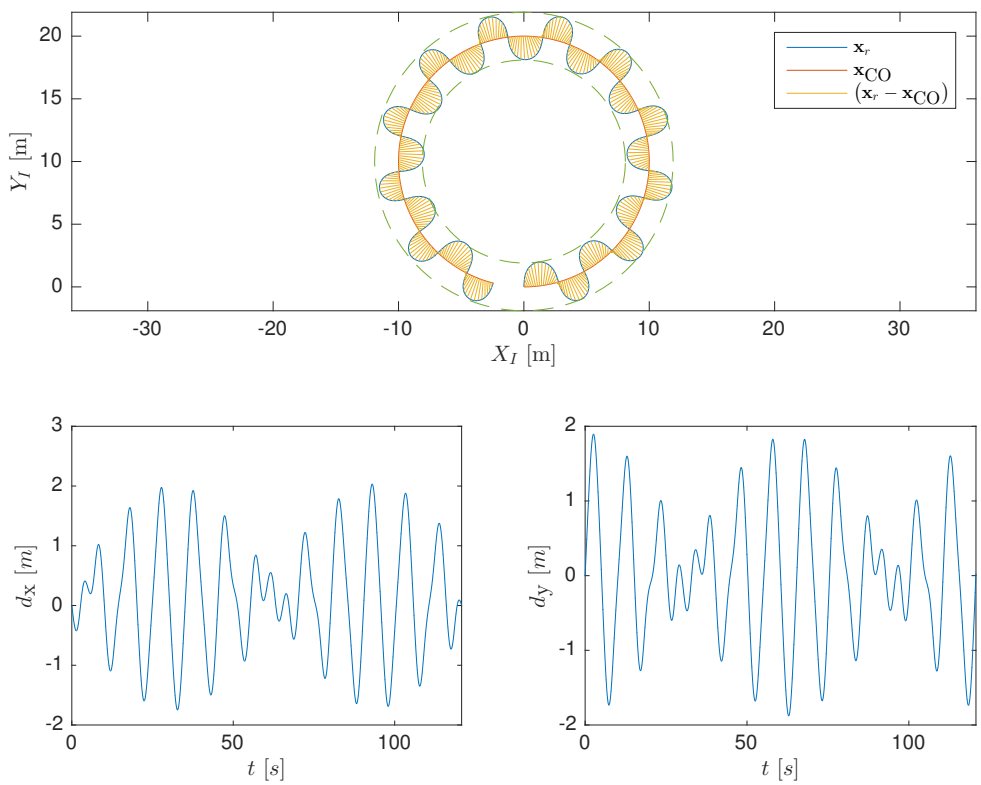

Figure 2.10: Representation of the distances between the reference point and the CO, in the X_I and Y_I axes directions, separately, with constant vessel heading rate $\omega_V = 0.05$ rad/s. Simulation during two oscillation periods $2T$, with $\nu = 0.5$.

2.6 Positioning of the Center of Oscillation (CO)

In the previous subsections, the generation of the reference point was described, based on an oscillatory motion around the CO. Additionally, the maximum distance achieved between the reference point and the CO was determined, depending on the current speed ratio ν. The goal of this subsection is to place the CO within the desired plume measurement site, so that the generated reference point trajectory complies with the proposed requirements. Ideally, the measurement site should be the closest possible to the vessel, but always respecting the keep-out area avoidance restriction.

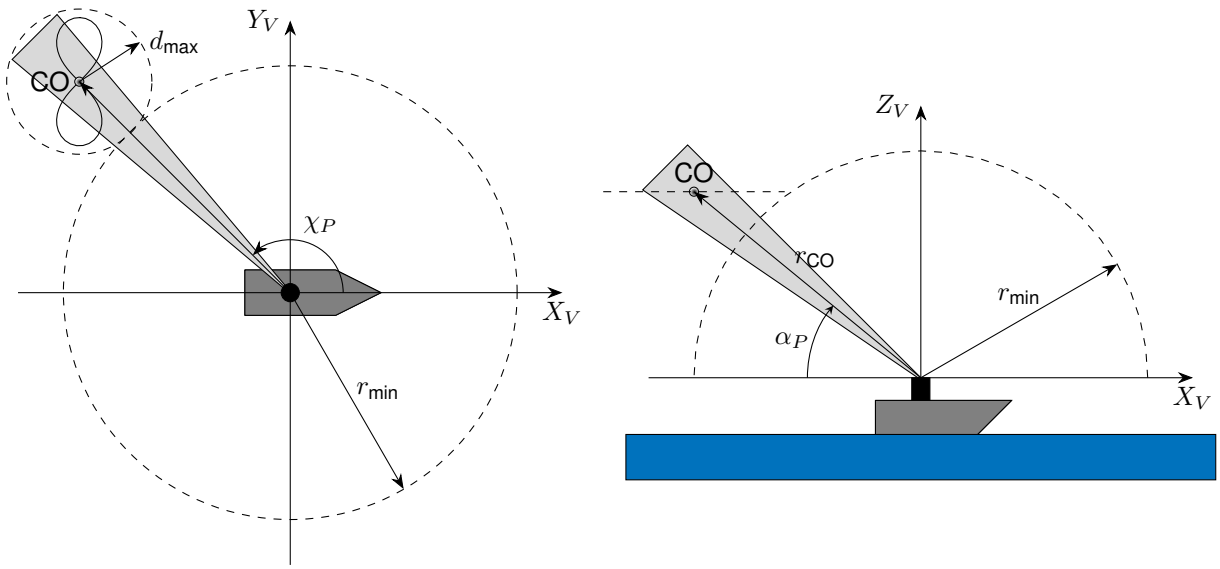

Figure 2.11: Representation of the vessel, the smoke plume, the CO and the reference point trajectory

The smoke plume direction is defined by means of its heading χ_P and elevation α_P, while the radius of the keep-out area around the vessel is represented by r_{min}. The position of the CO in the vessel reference frame is given by

$$\begin{cases} x_{\text{CO}} = r_{CO} \cos\alpha_P \cos\chi_P \\ y_{\text{CO}} = r_{CO} \cos\alpha_P \sin\chi_P \\ z_{\text{CO}} = r_{CO} \sin\alpha_P \end{cases} . \tag{2.31}$$

where r_{CO} is the three-dimensional distance between the vessel and the CO.

In order to ensure the reference trajectory never enters the keep-out area, one can relate r_{CO} with the maximum distance between the reference point and the CO, d_{max}, from

$$r_{\text{CO}} = r_{\text{min}} + d_{\text{max}} \cos\alpha_P, \tag{2.32}$$

where d_{max} is calculated from (2.27). However, the definition of the maximum distance in (2.27) is a very conservative approximation, and a less conservative solution can be defined in order to optimize the resulting distance between the reference point and the vessel.

A new approximation for the maximum distance d_{max} is now defined depending on the heading of the smoke plume χ_P, and is given by

$$d_{\text{max}}(\nu, \chi_P) = |d_{\text{x}}(t,\nu)|_{\text{max}} + \Big(|d_{\text{y}}(t,\nu)|_{\text{max}} - |d_{\text{x}}(t,\nu)|_{\text{max}} \Big) |\sin\chi_P| \tag{2.33}$$

where $|d_{\text{x}}(t,\nu)|_{\text{max}}$ and $|d_{\text{y}}(t,\nu)|_{\text{max}}$ are defined by (2.26).

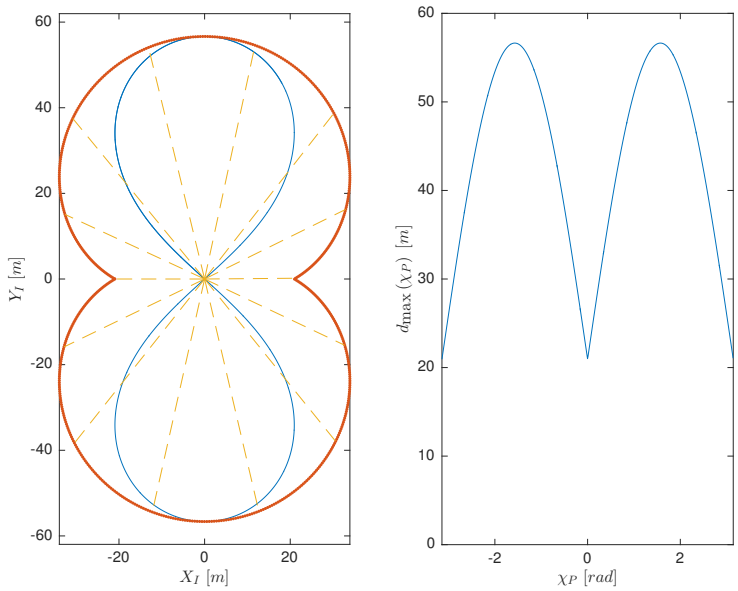

Figure 2.12: Representation of the new approximation for the maximum distance between the reference point and the CO, depending on the smoke plume heading. In this simulation the following values for the constants where considered: $V_\text{r} = 20$ m/s, $(\dot{\chi})_\text{max} = 1$ rad/s, $\nu = 0$

In Figure 2.12, the distance given by (2.33) is represented, for a null speed ratio. With this new solution for the approximation of the maximum distance between the reference point and the CO, depending on the smoke plume heading, the resulting positioning of the CO leads to the minimization of the minimum distance between the reference point and the vessel. The reference trajectory is then generated close to the keep-out area, while remaining always outside of it.

An additional solution can still be proposed. In the previous case, the only situations in which the reference point would reach exactly the minimum allowable distance to the vessel, r_min, occur when the heading of the smoke plume is $\chi_P = \pm\pi/2$. For every other values of χ_P, the minimum distance the reference point can get to the vessel is always slightly larger than r_min. In order to approach the reference trajectory even more to the keep-out area, one can use the oscillation phase ϕ_0 to minimize the distance between the smoke plume measurement point to the keep-out area,

$$\phi_0(\chi_P) = \begin{cases} \arccos\left(\frac{\chi_P+\pi/2}{\eta(\nu=0)}\right) & , \chi_P \in [-\pi, 0] \\ 2\pi - \arccos\left(\frac{\chi_P-\pi/2}{\eta(\nu=0)}\right) & , \chi_P \in [0, \pi] \end{cases} . \tag{2.34}$$

If the oscillation phase is tuned with the previous equations, depending on the smoke plume heading, the CO can be placed exactly in the border of the keep-out area, according to (2.31), with $r_{CO} = r_\text{min}$.

In order to better understand the difference between the proposed solutions, a series of simulations was made and is represented in the following figures. In each figure, several results are presented for the same solution, covering different values of the smoke plume heading, χ_P. A static vessel was considered, in order to provide a clearer representation. As the purpose of these simulations is to show clearly the differences between the proposed solutions, the elevation of the smoke plume is here considered to be zero, $\alpha_P = 0$ rad, and a top-view of the two-dimensional horizontal plane is depicted. The considered keep-out area radius is $r_\text{min} = 200$ m.

In Figure 2.13 the first and more conservative solution is presented. The very conservative approximation of the maximum distance (2.27) is evident in this simulations, mainly when the smoke plume is aligned with the vessel heading, when $\chi_P = 0$ or $\chi_P = \pi$ rad.

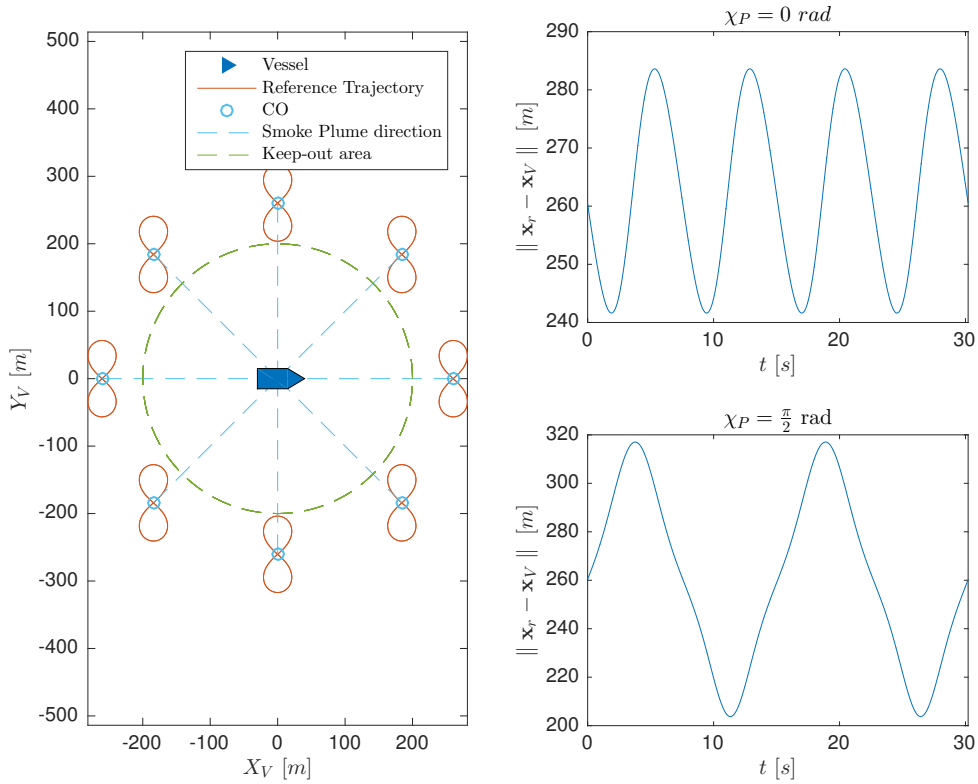

Figure 2.13: Simulation of the reference trajectory generation, for different smoke plume headings, considering the most conservative CO positioning method

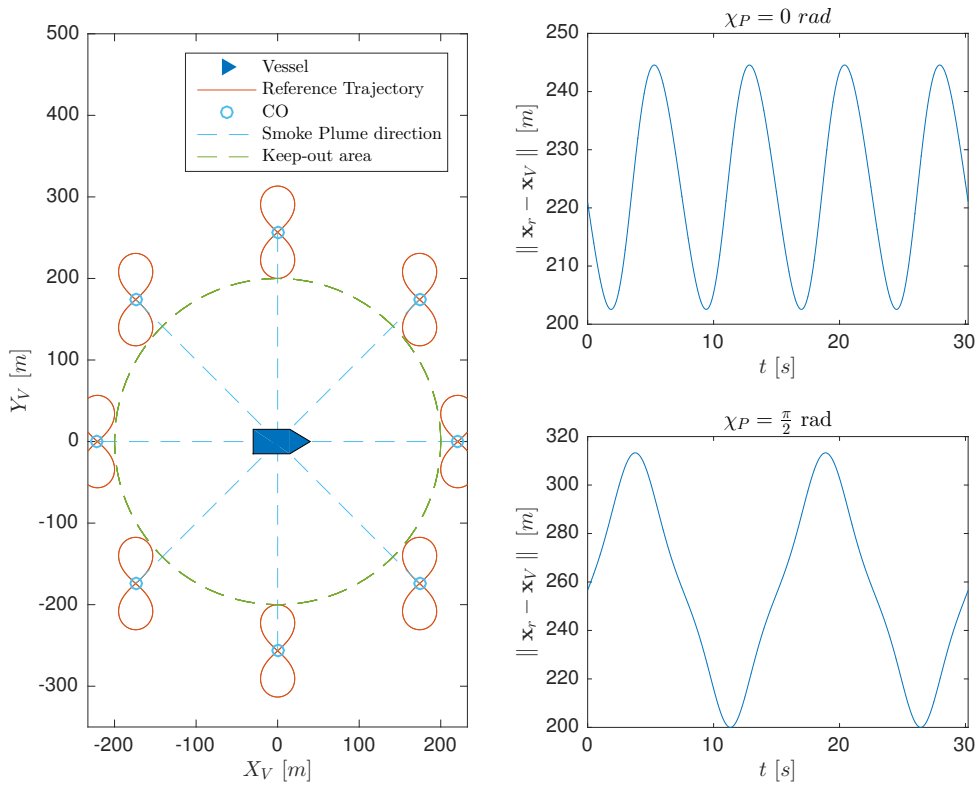

Figure 2.14: Simulation of the reference trajectory generation, for different smoke plume headings, considering the second CO positioning method

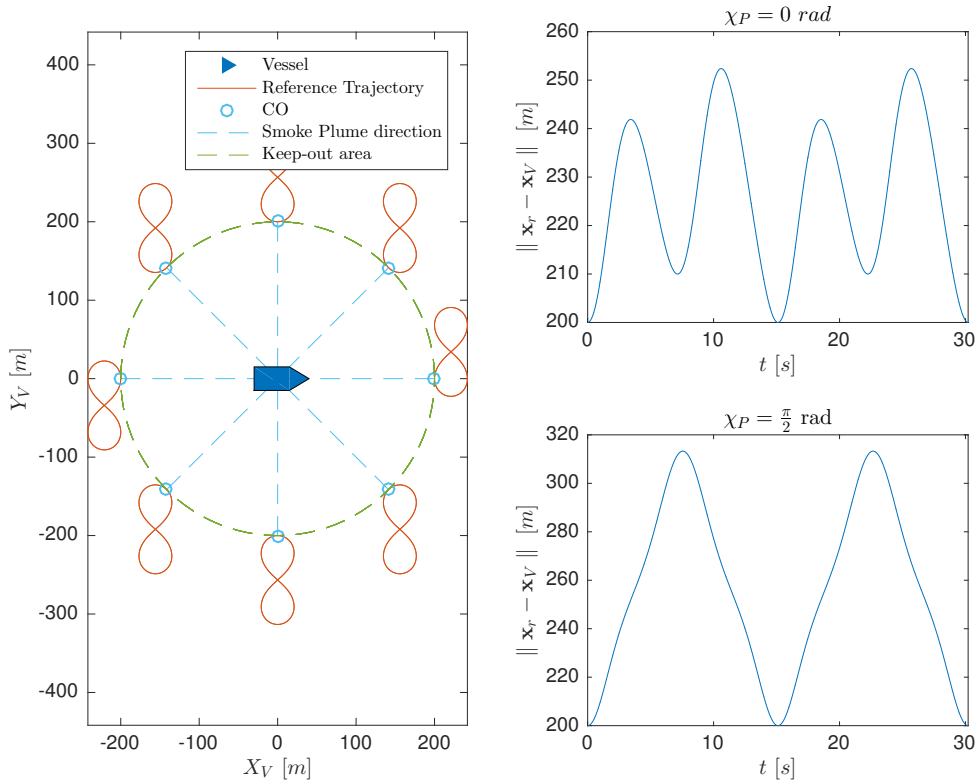

Figure 2.15: Simulation of the reference trajectory generation, for different smoke plume headings, considering the most accurate CO positioning method

The second solution is represented in Figure 2.14. Here, the baseline approximation for the maximum distance given by (2.33) leads to a significant improvement when compared to the previous one, as the reference trajectory is very close to the keep-out area borders for all the smoke plume directions.

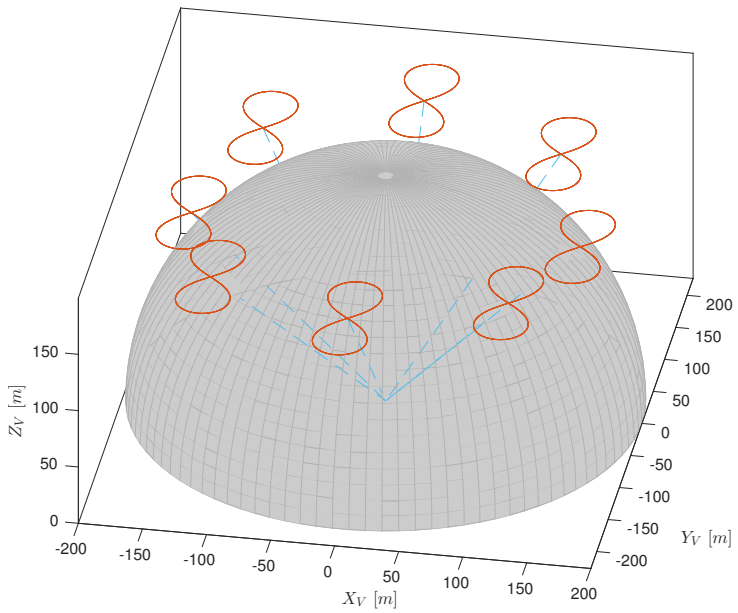

Figure 2.16: Three-dimensional simulation of the reference trajectory generation, for different smoke plume headings

Even with the significant improvement from the first to the second proposed methods, the smoke measurement site can still be placed closer to the keep-out area border – considering the smoke measurement is to be performed in the CO point. In Figure 2.15, the most accurate method is represented,

with the variation of the oscillation phase depending on the smoke plume heading. With this solution, the CO touches the keep-out area border exactly in the center of the smoke plume. However, with this last solution, the time interval between consecutive crossings through the CO is doubled, and the smoke plume measurements are performed only once in an oscillation period T.

Now that the difference between the several methods for the CO positioning is provided, the three-dimensional solution is presented in Figure 2.16 through a series of simulations, considering an elevation angle for the smoke plume of $\alpha_P = 45\,\mathrm{deg}$. The keep-out area is here represented by a semi-sphere, and is centered in the vessel position, with a radius of $r_{\text{min}} = 200$ m.

2.7 Summary

A guidance system was developed in this chapter, that is able to generate a reference trajectory for a constant speed UAV to follow a slower vessel. The designed system complies with the proposed objectives, generating a trajectory adjustable to the vessel motion, that enables a continuous tracking of the smoke plume, allowing for periodic gas measurements in optimized points, near the vessel but always outside the keep-out area.

The proposed solution for the reference trajectory is based on an oscillatory dynamics of the reference heading rate, allowing for a periodic crossing to a target point, here defined as the Center of Oscillation (CO), which is then placed in the desired point for the smoke plume measurements. The oscillatory motion is adjusted based on the oscillatory parameters η, ω_0, and ϕ_0, whose effect on the resulting trajectory motion is properly analyzed.

Parameter η is responsible for the target's mean speed following. Relating the reference mean motion along an oscillation period with the vessel speed, a relation was found between the speed ratio ν — vessel speed V_{V} over the reference speed V_{r} — and parameter η, based on the Bessel function of the first kind and zero order. With the inversion of this function in the appropriate domain, an expression was found for the required value of η for a given speed ratio. For a static vessel ($\nu = 0$) the resulting trajectory draws a Lemniscate of Bernoulli around the target. As the speed ratio increases, the value of η decreases accordingly, and the resulting heading range is shortened, leading to a progression of the reference trajectory along the vessel heading direction.

The oscillation frequency ω_0 is responsible for the regulation of the oscillation amplitude. Maintaining the shape of the trajectory resulting from the parameter η tuning, the frequency ω_0 will define the required maximum heading rate, being essential to assure the UAV maximum heading rate is satisfied. The value of ω_0 will then affect the oscillation period $T = 2\pi/\omega_0$, and, thus, smaller values of ω_0 lead to an increase in the time between consecutive crossings over the CO.

The remaining parameter, ϕ_0, stands for the oscillation phase and is particularly useful to adjust the position of the initial point in the resulting periodic trajectory. For example, when considering a static vessel, a value of $\phi_0 = 0$ leads to the resulting trajectory to oscillate around the initial point, being the center of the Lemniscate, while a phase $\phi_0 = \pi/2$ rad produces the generation of the resulting trajectory "below" the initial point, being in the top of the Lemniscate.

After the analysis of the oscillation parameters, the maximum distance achieved between the reference point and the CO was found in both coordinate directions. Then, the CO was placed in the smoke plume direction, in relation to the vessel, at a distance r_{CO}. This offset distance r_{CO} is computed based on the keep-out area radius and on the maximum distance between the CO and the reference point, previously calculated, in order to ensure that the reference point never enters the keep-out area.

The designed guidance system is then in compliance with the stated objectives, providing a feasible trajectory for a constant speed UAV to track a moving vessel, while flying through the smoke plume, allowing for consecutive gas measurements in optimized points, always respecting the minimum distance to the vessel.

Chapter 3

Control

This chapter is devoted to the development of a control method for a fixed-wing UAV to track a virtual reference point, such as the one generated by the guidance system designed in the previous chapter. The results obtained in this chapter can be applied to a wide range of autonomous nonholonomic vehicles other than UAVs, such as underwater vehicles, underactuated vessels, cars, or other ground vehicles or robots with similar nonholonomic constraints.

The main contribution of this thesis is presented in this chapter, which is a novel error formulation that eliminates the singularity presented on the line-of-sight tracking of a constant-speed vehicle.

First, the control problem is introduced, as well as the notation used to solve it. Secondly, a brief overview of the existing solutions for trajectory tracking of nonholonomic vehicles is provided. Then, the new problem formulation that accounts for the constant speed constraint is presented. A nonlinear controller is derived, and global asymptotic stability is proved by using Lyapunov-based methods, as well as a cascaded system approach. Finally, the trade-off between convergence rate and control effort is discussed.

3.1 Introduction of the Control Problem

The main target tracking problem of this dissertation is first addressed in the previous chapter. The first key challenge was due to the speed differential between the target and the pursuer vehicle. With the generation of a virtual reference point moving with the desired trajectory for the pursuer, the challenge becomes to track a target with the same speed and a feasible motion. It is important to note that all the dynamics considered in this chapter are written in the two-dimensional horizontal plane, considering a top-view of the environment.

Consider all types of nonholonomic vehicles that can be represented as a unicyle – or the so-called Dubins vehicle – by the equations of motion in (2.4). The main limitation of these dynamics is due to the absence of lateral velocity and is characterized by the nonholonomic constraint

$$\dot{y}\cos\chi - \dot{x}\sin\chi = 0. \tag{3.1}$$

Moreover, consider that a feasible reference trajectory is given and that it can be represented by

$$\dot{\mathbf{x}}_{\mathsf{r}} = \begin{cases} \dot{x}_{\mathsf{r}} = v_{\mathsf{r}}\cos(\chi_{\mathsf{r}}) \\ \dot{y}_{\mathsf{r}} = v_{\mathsf{r}}\sin(\chi_{\mathsf{r}}) \\ \dot{\chi}_{\mathsf{r}} = \omega_{\mathsf{r}} \end{cases} . \tag{3.2}$$

The feasible reference speed v_{r} and heading rate ω_{r} functions should be suitable for the considered pursuer. In the particular case of a UAV, as considered in this dissertation, the reference speed should be a constant value, ideally the optimal speed for a cruise flight condition. The reference heading rate described in the previous chapter is given by

$$\omega_{\mathsf{r}}(t) = -\eta\omega_0 \sin\left(\omega_0 t + \phi_0\right), \tag{3.3}$$

which is a feasible reference heading function for a UAV, as long as the amplitude of this oscillatory motion never exceeds the UAV maximum heading rate, i.e., $|\eta\omega_0| \leq \omega_{\mathsf{max}}$. In order to extend the applications of the following results in this chapter, the reference heading rate will be considered to be a generic

bounded and smooth function, that can be either a constant or a time-varying function. Moreover, in order to comply with subsequent requirements, the derivative of the reference heading rate should be also bounded, i.e., $|\dot{\omega}_\mathsf{r}| \leq (\dot{\omega}_\mathsf{r})_{\mathsf{max}}$.

The geometry of the tracking control problem is illustrated in Figure 3.1:

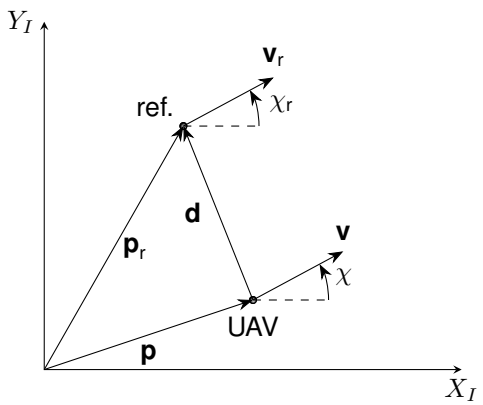

Figure 3.1: Geometry of the tracking control problem. Representation of the pursuer vehicle (UAV) and the reference point in the horizontal plane of the inertial reference frame, as well as the corresponding velocity vectors.

Vector $\mathbf{p}$ represents the horizontal coordinates of the controllable vehicle in the inertial reference frame, $\left(x^I, y^I\right)^T$. For convenience of notation, the index associated with the inertial reference frame, $\{I\}$, will be omitted, leading to $\mathbf{p} = (x, y)^T$. The same simplification is applied to the reference position $\mathbf{p}_\mathsf{r} = (x_\mathsf{r}, y_\mathsf{r})^T$. It is recalled that the reference point should be interpreted as a desired virtual pursuer. In the present chapter, the commanded pursuer speed will be considered to match that of the reference, i.e. $v = V_\mathsf{r}$. The velocity of the pursuer can then be represented by $\dot{\mathbf{p}} = \mathbf{v} = \mathcal{R}(\chi)\begin{bmatrix} V_\mathsf{r} & 0 \end{bmatrix}^T$, and the analogous stands for the reference velocity $\dot{\mathbf{p}}_\mathsf{r} = \mathbf{v}_\mathsf{r}$. The standard rotation matrix $\mathcal{R}(\alpha)$ that will be widely used in the current chapter is defined as the two-dimensional right-handed rotation by an angle α and can be written from the rotation matrix (2.3) as

$$\mathcal{R}(\alpha) \triangleq \begin{bmatrix} 1 & 0 & 0 \\ 0 & 1 & 0 \end{bmatrix} \mathcal{R}_B^I(\alpha, 0, 0) \begin{bmatrix} 1 & 0 \\ 0 & 1 \\ 0 & 0 \end{bmatrix} = \begin{bmatrix} 1 & 0 & 0 \\ 0 & 1 & 0 \end{bmatrix} \begin{bmatrix} \cos\alpha & -\sin\alpha & 0 \\ \sin\alpha & \cos\alpha & 0 \\ 0 & 0 & 1 \end{bmatrix} \begin{bmatrix} 1 & 0 \\ 0 & 1 \\ 0 & 0 \end{bmatrix} = \begin{bmatrix} \cos\alpha & -\sin\alpha \\ \sin\alpha & \cos\alpha \end{bmatrix}, \tag{3.4}$$

and its time derivative is denoted as $\dot{\mathcal{R}}(\alpha) = \mathcal{S}(\dot{\alpha})\,\mathcal{R}(\alpha)$, where $\mathcal{S}(\dot{\alpha}) \triangleq \dot{\alpha}\begin{bmatrix} 0 & -1 \\ 1 & 0 \end{bmatrix}$.

The main objective of the tracking control problem is to control the pursuer position to the reference position, $\mathbf{p} \to \mathbf{p}_\mathsf{r}$, as well as the pursuer velocity to the reference velocity vector, $\mathbf{v} \to \mathbf{v}_\mathsf{r}$. The latter control objective for the velocity vector can be posed only as a heading direction objective, $\chi \to \chi_\mathsf{r}$, since the speed V_r is considered to be controlled separately by an inner-loop controller. Since the relative positions can be represented by the distance vector as $\mathbf{d} = \mathbf{p}_\mathsf{r} - \mathbf{p}$, the former objective can be stated as $\mathbf{d} \to 0$. Therefore, the analysis taken in this chapter will aim to reach this control objective asymptotically, satisfying all the aforementioned contraints.

3.2 Background on existing nonholonomic tracking control solutions

Despite the vast research carried out in the last decades on the guidance and control of autonomous vehicles, the tracking control problem addressed in this dissertation is still an open topic for highly-constrained vehicles such as fixed-wing UAVs. The existing solutions in terms of the tracking control of unicycle-like vehicles consider two degrees-of-freedom for actuation, both the speed and the heading

rate. However, the control challenge that emerged in the current study is confined to just one degree-of-freedom, since the only control input is the UAV heading rate – the speed and altitude are taken as constants.

In the present section, existing solutions for the nonholonomic tracking control are briefly described, motivating for the challenge that arises when the speed control is set to constant.

A vast literature on the topic of nonholonomic tracking control can be found, for instance, in [57, 58, 59, 60, 61, 62, 63, 64]. A very extensive literature review on the control of nonholonomic systems is provided in [60], including recent developments in this research field. These works focus on nonholonomic vehicles than can be described by (2.4), and on the problem of tracking virtual desired references as in this dissertation.

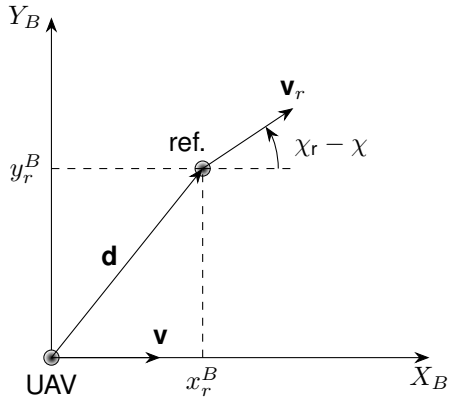

Figure 3.2: Geometry of the tracking control problem, in the body reference frame $\{B\}$.

Most of the aforementioned references consider the same control geometry, which can be considered the most straightforward approach to the problem. The reference point position is written in the pursuer body-fixed reference frame, as depicted in Figure 3.2. Furthermore, the error state is defined as the difference between both configurations – coordinates and heading –, written in the pursuer body-fixed reference frame, as follows:

$$\mathbf{x}_e = \begin{bmatrix} x_e \\ y_e \\ \chi_e \end{bmatrix} = \begin{bmatrix} x_\mathsf{r}^B \\ y_\mathsf{r}^B \\ \chi_\mathsf{r} - \chi \end{bmatrix} = \mathcal{R}_I^B(\chi, 0, 0) \begin{bmatrix} x_\mathsf{r} - x \\ y_\mathsf{r} - x \\ \chi_\mathsf{r} - \chi \end{bmatrix} \tag{3.5}$$

This error state formulation leads to the following error dynamics, whose derivation is provided in Appendix A:

$$\dot{\mathbf{x}}_e = \begin{bmatrix} \dot{x}_e \\ \dot{y}_e \\ \dot{\chi}_e \end{bmatrix} = \begin{bmatrix} y_e\omega - v + V_\mathsf{r}\cos\chi_e \\ -x_e\omega + V_\mathsf{r}\sin\chi_e \\ \omega_r - \omega \end{bmatrix} = \begin{bmatrix} \cos\chi_e & 0 \\ \sin\chi_e & 0 \\ 0 & 1 \end{bmatrix} \begin{bmatrix} V_\mathsf{r} \\ \omega_r \end{bmatrix} + \begin{bmatrix} -1 & y_e \\ 0 & -x_e \\ 0 & -1 \end{bmatrix} \begin{bmatrix} v \\ \omega \end{bmatrix} \tag{3.6}$$

With the control inputs of the pursuer vehicle being its speed v and heading rate ω, the underactuation due to the nonholonomic constraint (3.1) is evident in the error state dynamics of (3.6), where it can be seen that the input variables are outnumbered by the states.

This limitation is overcome in the literature, and global asymptotic stability is achieved either with controllers derived from Lyapunov functions [57, 58, 59, 61], applying backstepping techniques [61, 63], or through the cascaded system approach [62, 64]. In this dissertation, a brief analysis is made on some of the proposed controllers in the previously cited works, so that insight is provided on the difference between the different methods for the controllers design.

The similar Lyapunov-based controllers derived in [58] ($\mathbf{u}_1$) and [61] ($\mathbf{u}_2$) are given by:

$$\mathbf{u}_1 = \begin{bmatrix} v \\ \omega \end{bmatrix} = \begin{bmatrix} V_\mathsf{r}\cos\chi_e + k_1 x_e \\ \omega_r + V_\mathsf{r}\left(k_2 y_e + k_3 \sin\chi_e\right) \end{bmatrix},$$

$$\mathbf{u}_2 = \begin{bmatrix} v \\ \omega \end{bmatrix} = \begin{bmatrix} V_\mathsf{r} \cos \chi_e + k_2 x_e \\ \omega_r + V_\mathsf{r} y_e \frac{\sin \chi_e}{\chi_e} + k_1 \chi_e \end{bmatrix}.$$

In these controllers, it is evident the direct cancellation of the terms $V_\mathsf{r} \cos \chi_e$ and ω_r which appeared directly in (3.6). The remaining terms come from the chosen Lyapunov function derivative, in order to make it negative. For example in the first case [58] the adopted Lyapunov function is $V = \left(x_e^2 + y_e^2\right)/2 + \left(1 - \cos \chi_e\right)/k_2$ and the resultant derivative evaluated on the closed-loop system becomes $\dot{V} = -k_1 x_e^2 - V_\mathsf{r} \frac{k_3}{k_2} \sin^2 \chi_e \leq 0$.

This method is sufficient to prove stability. However, it is only suitable for vehicles with full speed control, since the speed control input can be close to zero, which is clearly not suitable for the kind of speed constraints considered in this thesis. Similar results are achieved by means of the backstepping technique, though leading to more complex controller equations.

A slightly different controller is achieved with the cascade system approach. This method leads to simpler controller equations, such as the ones derived in [62] and used in [64]:

$$\mathbf{u} = \begin{bmatrix} V_\mathsf{r} + k_1 x_e - k_2 \omega_r y_e \\ \omega_r + k_3 \chi_e \end{bmatrix}$$

The previous equation for the speed control law is clearly closer to the imposed speed constraints. Furthermore, a result for constrained input is derived in [62]:

$$\mathbf{u} = \begin{bmatrix} V_\mathsf{r} + \sigma_x(x_e) \\ \omega_r + \sigma_\chi(\chi_e) \end{bmatrix} \tag{3.7}$$

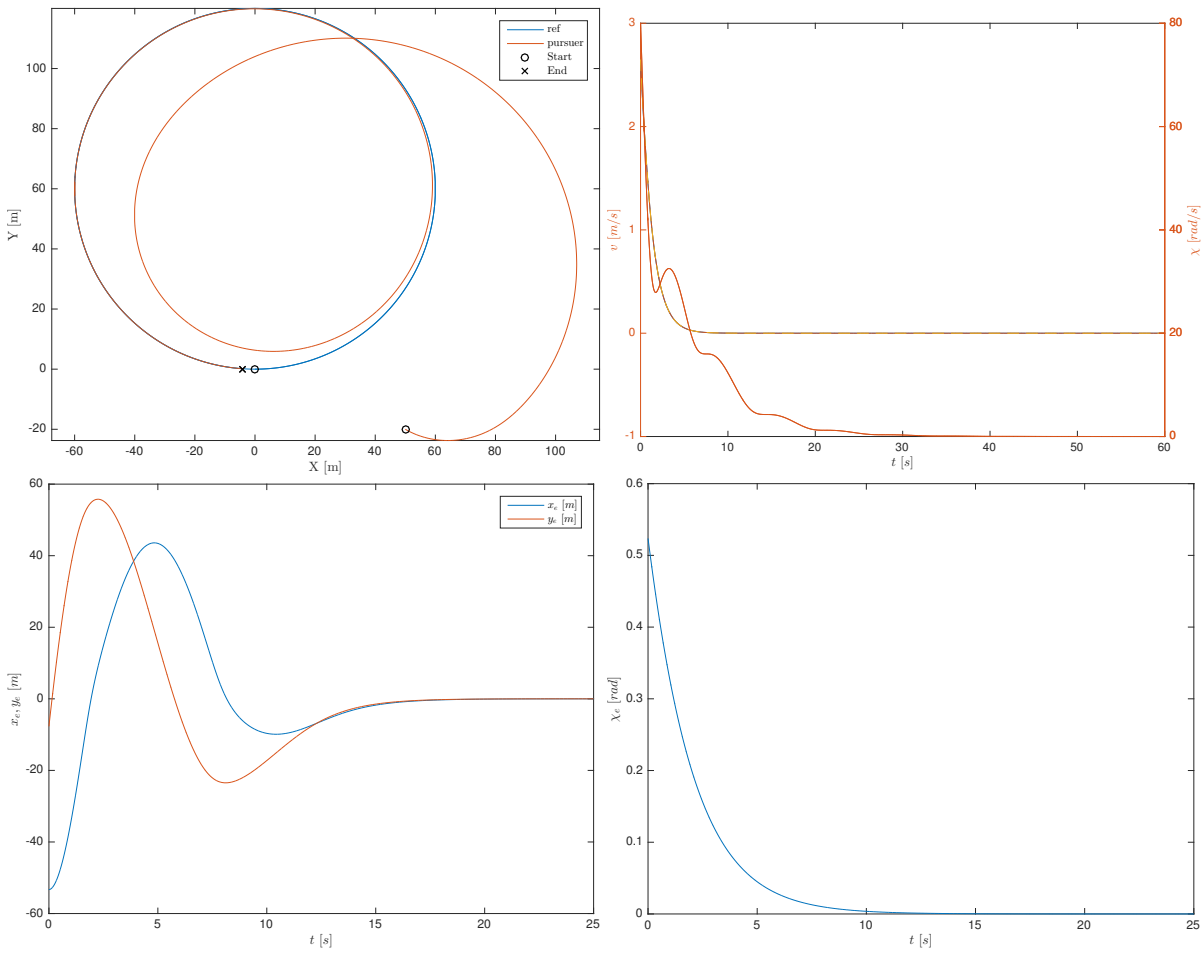

Figure 3.3: Simulation of a tracking control problem applying the controller (3.7). $V_r = 30\ m/s$, $\omega_r = 0.5\ rad/s$, $k_1 = 10$, $k_2 = 0.1$, $k_3 = 0.5$ and $k_4 = 1$.

This resulting control law considers generic saturation function $\sigma(x)$ that satisfies the conditions $x\sigma(x) > 0, \forall x \neq 0$ and $\frac{d\sigma}{dx}(0) > 0$, and requires a bounded reference speed $V_{\mathrm{r}}(t)$ and a persistently exciting $\omega_r(t)$. The idea of the cascaded system approach in this case is to use the heading rate control input to stabilize directly the heading error, forcing the pursuer heading to be aligned with the reference heading, and then use only the speed input control to lead the pursuer position to match the reference. Simulation results are presented in Figure 3.3 by applying the previous controller, with saturation functions $\sigma_x(x) = k_1 \tanh(k_2 x)$ and $\sigma_\chi(\chi_e) = k_3 \tanh(k_4 \chi_e)$.

The results of this simulation show that the controller (3.7) is close to the needs of this dissertation. Given the restricted but still existing range on the fixed-wing UAVs speed, this controller can be applied. In this example, the nominal speed of $v = 30\ m/s$ was considered, as well as a speed variation of $\pm 10\ m/s$ around the nominal speed. This is usually feasible for a standard UAV. However, frequent speed variations are strongly not recommended for fixed-wing UAVs as it leads to a significant increase in the energy consumption.

Therefore, from the existing solutions on the nonholonomic tracking control, there is no suitable result for the needs of the tracking control problem at hand. The most promising results for the problem addressed in this work are those presented in [65], where a nonlinear guidance logic is introduced to guide a fixed-wing UAV on curved trajectories. This solution is based on a line-of-sight control approach that follows a reference point in the desired path line. However, the main goal of [65] is to deal with the path following problem – not the same as trajectory tracking –, and the reference point considered in this solution is chosen by the guidance system, taking into account the current position of the UAV with respect to the path line.

An alternative approach to guide a UAV to track a reference point is proposed in the previously cited paper [35]. The same oscillatory motion is considered for the generation of a virtual reference point and a guidance law is suggested for the UAV to track the reference. This guidance law is based on the line-of-sight between the UAV and the reference point, and convergence is achieved for specific initial conditions, with short initial errors. The main shortcoming, however, of this solution is that it cannot guarantee global stability.

The main problem of the guidance solution suggested in [35] is that the relative angle, defined as the difference between the heading of the UAV and the line-of-sight, is not defined when the target coincides with the reference point, representing a singularity of the algorithm, which is to be avoided in control laws. Moreover, the relative angle rate can reach very high values for certain initial conditions, leading to unfeasible heading rate commands. This is a great challenge on the tracking control problem when only the heading rate control is available, and will be analysed in more detail in the following section.

3.3 Derivation of the error formulation

This section contains one of the main contributions of this dissertation, that is the derivation of a new system formulation for tracking control problems, based on a δ-control approach, which will be described in the sequel. Firstly, an intermediate result on proportional line-of-sight control is presented. Although not being of particular relevance for the final result of this dissertation, it can be seen as a bridge between the existing solutions described in the previous section, and the novel approach that will be presented in the remainder of this section.

3.3.1 Proposed approach for the line-of-sight proportional control

3.3.1.1 Error state dynamics derivation

By exploiting a control approach similar to the one adopted in [35], a different formulation is here presented. The desired heading, taken as a reference for the control law, is the line-of-sight between the UAV and the reference point. In Figure 3.4, the control geometry of Figure 3.1 is again depicted, but now with the introduction of the heading of the line-of-sight, represented as χ_d:

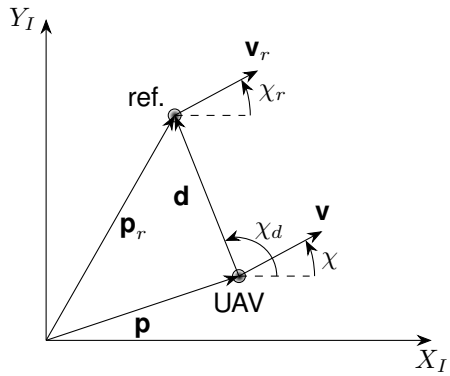

Figure 3.4: Geometry of the tracking control problem, defining the heading of the relative vector.

Defining its norm as $\|\mathbf{d}\| = d$, the relative vector $\mathbf{d}$ can be written in inertial coordinates as $\mathbf{d} = \mathcal{R}(\chi_d)\begin{bmatrix} d & 0 \end{bmatrix}^T$. Moreover, vector $\mathbf{d}$ can be also written in the inertial reference frame as the difference between both the reference point and the UAV positions, as $\mathbf{d} = \mathbf{p}_r - \mathbf{p}$. Thus, both representations of vector $\mathbf{d}$ can be equalized, leading to

$$\mathcal{R}(\chi_d)\begin{bmatrix} d & 0 \end{bmatrix}^T = \mathbf{p}_r - \mathbf{p}. \tag{3.8}$$

Now differentiating both sides of the previous equation with respect to time, and assuming the heading rate of the line-of-sight to be $\dot{\chi}_d = \omega_d$, it follows:

$$\mathcal{S}(\omega_d)R(\chi_d)\begin{bmatrix} d & 0 \end{bmatrix}^T + R(\chi_d)\begin{bmatrix} \dot{d} & 0 \end{bmatrix}^T = V_\mathrm{r}\Big[\mathcal{R}(\chi_\mathrm{r}) - \mathcal{R}(\chi)\Big]\begin{bmatrix} 1 & 0 \end{bmatrix}^T. \tag{3.9}$$

Now the proposed formulation involves representing the given relations in a local reference frame $\{D\}$ fixed with the UAV and having its X_D axis aligned with the direction of the line-of-sight. The resulting geometry is depicted in Figure 3.5:

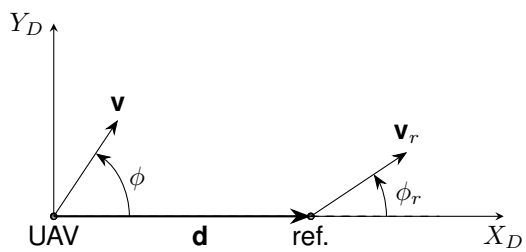

Figure 3.5: Geometry of the tracking control problem in the relative reference frame $\{D\}$.

Therefore, a rotation is applied by an angle χ_d to (3.9), resulting in:

$$R^T(\chi_d)\mathcal{S}(\omega_d)R(\chi_d)\begin{bmatrix} d & 0 \end{bmatrix}^T + R^T(\chi_d)R(\chi_d)\begin{bmatrix} \dot{d} & 0 \end{bmatrix}^T = V_\mathrm{r}R^T(\chi_d)\Big[\mathcal{R}(\chi_\mathrm{r}) - \mathcal{R}(\chi)\Big]\begin{bmatrix} 1 & 0 \end{bmatrix}^T. \tag{3.10}$$

Applying basic linear algebra to the previous equation, the unknown velocity of the line-of-sight vector $\mathbf{d}$ can be found, with the linear $\dot{d}$ and the angular ω_d velocities being then given by:

$$\begin{bmatrix} \dot{d} \\ d\omega_d \end{bmatrix} = V_\mathrm{r}\begin{bmatrix} \cos(\chi_r - \chi_d) - \cos(\chi - \chi_d) \\ \sin(\chi_r - \chi_d) - \sin(\chi - \chi_d) \end{bmatrix} \tag{3.11}$$

Now defining the error state as $\mathbf{x}_1 = \begin{bmatrix} d & \phi_r & \phi \end{bmatrix}^T$, where the new variables are defined as $\phi_r = \chi_\mathrm{r} - \chi_d$ and $\phi = \chi - \chi_d$, the tracking control problem can be represented by the following error state

dynamics:

$$\dot{\mathbf{x}}_1 = \begin{bmatrix} \dot{d} \\ \dot{\phi}_r \\ \dot{\phi} \end{bmatrix} = \begin{bmatrix} V_r\big(\cos\phi_r - \cos\phi\big) \\ \omega_r - \omega_d \\ \omega - \omega_d \end{bmatrix} = \begin{bmatrix} V_r\big(\cos\phi_r - \cos\phi\big) \\ \omega_r - \frac{V_r}{d}\big(\sin\phi_r - \sin\phi\big) \\ \omega - \frac{V_r}{d}\big(\sin\phi_r - \sin\phi\big) \end{bmatrix}. \tag{3.12}$$

This formulation is equivalent to the one considered in [35], with the available control input on the UAV heading rate controlling directly the state variable ϕ, while the remaining state variables d and ϕ_r being affected only by the respective cross terms. Note that the reference frame represented in Figure 3.5 is not inertial, and its angular velocity is represented in the error state dynamic through the variable ω_d.

The desired point of the control problem in this state formulation is given by $\mathbf{x}_1^d = \big(d, \phi_r, \phi\big)^d = \big(0, 0, 0\big)$. As can be noted in the error state dynamics (3.12), there is a singularity exactly at the desired point, where the line-of-sight heading is not defined. This is the same problem as described earlier in the analysis of the control solution proposed in [35]. However, despite this singularity, a particular case will be discussed in the following subsection, where an interesting result can be obtained, as long as the initial conditions are such that the system never approaches the singularity.

3.3.1.2 Particular case: circular reference trajectory– control of the steady-state distance error

Here the particular case of a circular reference trajectory is assessed, considering the error state dynamics deduced formerly. Despite the singularity in this formulation, the particular example that will be presented next can be interesting for specific applications, where the system tend to a constant steady-state error, thus converging to a state other than the desired point defined previously as $\mathbf{x}_1^d$.

Consider a basic proportional feedback controller acting linearly with the error on the state variable ϕ, given by

$$\omega = -k\phi, \tag{3.13}$$

where k is a positive constant. Then, the closed-loop system in (3.12) with the controller described in (3.13) becomes

$$\dot{\mathbf{x}}_1 = \begin{cases} \dot{d} & = V_\mathrm{r}\big(\cos\phi_r - \cos\phi\big) \\ \dot{\phi}_r & = \omega_r - \frac{V_\mathrm{r}}{d}\big(\sin\phi_r - \sin\phi\big) \\ \dot{\phi} & = -k\phi - \frac{V_\mathrm{r}}{d}\big(\sin\phi_r - \sin\phi\big) \end{cases}. \tag{3.14}$$

From the resulting controlled system, no major benefit seems to be achieved from the proportional controller, since the controlled state derivative $\dot{\phi}$ still has a term other than the stabilizing one. However, analyzing equations (3.14), one can expect the control input to converge to the reference heading rate ω_r, in the case of a circular reference trajectory, where ω_r is constant. Hence, the following analysis will consider by hypothesis that an equilibrium point exists, with the equilibrium control input being given by $\omega_{eq} = \omega_r$.

The equilibrium value of ϕ can be computed by inverting the control law in (3.13):

$$w_\mathrm{eq} = \omega_r \Rightarrow \phi_{eq} = -\frac{\omega_r}{k}. \tag{3.15}$$

Furthermore, the equilibrium values of the other state variables can be related with ϕ_{eq} if we consider the trajectory of the UAV in equilibrium to describe the same circunference as the reference one, but with a phase lag. This idea is depicted in Figure 3.6.

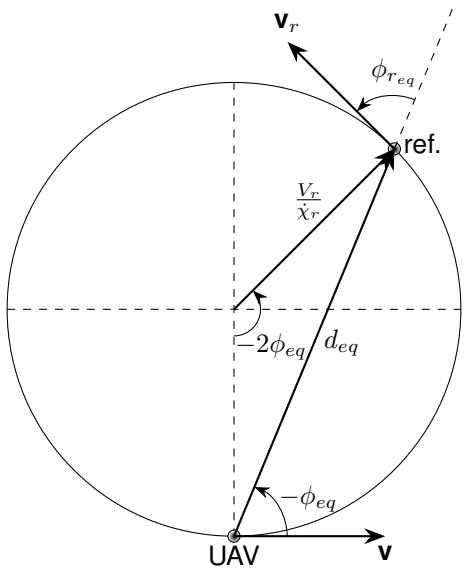

Figure 3.6: Geometry of the equilibrium state of the controlled system (3.14) for a circular reference trajectory. The relations between the different state variables can be easily derived from basic geometry.

Considering the geometry of the equilibrium state to be as illustrated in Figure 3.6, the relations between the three state variables can be found by using generic triangle and circumference properties. Thus, the state variables are related by $\phi_{r_{eq}} = -\phi_{eq}$ and $d_{eq} = 2R_r \sin\big(-\phi_{eq}\big)$, where R_r is the radius of the circular trajectory, given by $R_r = V_\mathsf{r}/\omega_r$. Accordingly, the equilibrium state is denoted by

$$\mathbf{x}_{1_{eq}} = \begin{cases} d_{eq} & = \frac{2V_\mathsf{r}}{\omega_r}\sin\left(\frac{w_r}{k}\right) \\ \phi_{r_{eq}} & = \frac{\omega_r}{k} \\ \phi_{eq} & = -\frac{\omega_r}{k} \end{cases} . \tag{3.16}$$

The steady-state equilibrium was derived by exploiting the knowledge available on the system, in an intuitive manner, to provide insight on the problem at hand. Formally, replacing the equlibrium state (3.16) in the controlled system (3.14), it can be seen that all the state derivatives are cancelled $\big(\dot{\mathbf{x}}_1(\mathbf{x}_{1_{eq}}) = 0\big)$. Thus, the solution given in (3.16) is proved to be an equilibrium of the system (3.14).

Now that an equilibrium point was identified, one may assess its stability. This result can be achieved through the so-called *Lyapunov's indirect method* (Theorem 4.7 in [66]), that analyzes the stability of an equilibrium point for a linearized system, to provide conditions for the stability of the nonlinear system around the given equilibrium point. Hence, the *Jacobian Matrix* A of system (3.14) is computed at the equilibrium point (3.16):

$$\begin{aligned} A = \frac{\partial f}{\partial \mathbf{x}_1}(\mathbf{x}_1)\bigg|_{\mathbf{x}_1=\mathbf{x}_{1_{eq}}} &= \begin{bmatrix} 0 & -V_\mathsf{r}\sin\phi_r & V_\mathsf{r}\sin\phi \\ \frac{V_\mathsf{r}}{d^2}\big(\sin\phi_r - \sin\phi\big) & -\frac{V_\mathsf{r}}{d}\cos\phi_r & \frac{V_\mathsf{r}}{d}\cos\phi \\ \frac{V_\mathsf{r}}{d^2}\big(\sin\phi_r - \sin\phi\big) & -\frac{V_\mathsf{r}}{d}\cos\phi_r & -k + \frac{V_\mathsf{r}}{d}\cos\phi \end{bmatrix}_{\mathbf{x}_1=\mathbf{x}_{1_{eq}}} \\ &= \begin{bmatrix} 0 & -V_\mathsf{r}\sin\left(\frac{\omega_r}{k}\right) & -V_\mathsf{r}\sin\left(\frac{\omega_r}{k}\right) \\ \frac{\omega_r^2}{2V_\mathsf{r}\sin\left(\frac{\omega_r}{k}\right)} & -\frac{\omega_r}{2\tan\left(\frac{\omega_r}{k}\right)} & \frac{\omega_r}{2\tan\left(\frac{\omega_r}{k}\right)} \\ \frac{\omega_r^2}{2V_\mathsf{r}\sin\left(\frac{\omega_r}{k}\right)} & -\frac{\omega_r}{2\tan\left(\frac{\omega_r}{k}\right)} & -k + \frac{\omega_r}{2\tan\left(\frac{\omega_r}{k}\right)} \end{bmatrix} \end{aligned} \tag{3.17}$$

Lyapunov's indirect method states that if Re$\lambda_i < 0$ for all eigenvalues λ_i of matrix A, then the considered equilibrium point is asymptotically stable. Moreover, if Re$\lambda_i > 0$ for at least one of the eigenvalues of A, then the equilibrium is unstable. Therefore, in order for the first condition to be satisfied, all the eigenvalues of A should be in the left half on the complex plane. Thus, in order to evaluate its eigenval-

ues, the characteristic polynomial of matrix A needs be calculated as follows

$$det(A - \lambda I) = 0 \Leftrightarrow \lambda^3 + k\lambda^2 + \left[\frac{k\omega_r}{2\tan(\frac{\omega_r}{k})} + \omega_r^2\right]\lambda + \frac{k\omega_r^2}{2} = 0. \tag{3.18}$$

Based on the *Routh-Hurwitz Stability Criterion* [67], all the eigenvalues of A are on the left side of the imaginary plane **if and only if** the following conditions are satisfied:

- $k > 0 \wedge \left[\frac{k\omega_r}{2\tan(\frac{\omega_r}{k})} + \omega_r^2\right] > 0 \Rightarrow k > 0 \wedge k > -2\omega_r \tan\left(\frac{\omega_r}{k}\right)$
- $k\left[\frac{k\omega_r}{2\tan(\frac{\omega_r}{k})} + \omega_r^2\right] > \frac{k\omega_r^2}{2} \Leftrightarrow k > -\omega_r \tan\left(\frac{\omega_r}{k}\right)$

The condition of the control gain to be positive $k > 0$ is guaranteed by definition. Additionally, since the tangent function, $\tan x$, is odd for $|x| < \pi/2$, and given the limits $\lim_{x\to\pi/2^-} \tan x = +\infty$ and $\lim_{x\to\pi/2^+} \tan x = -\infty$, the remaining two conditions are satisfied whenever the norm of the input of the tangent function does not exceed $\pi/2$. Therefore, the previous conditions simplify to

$$k > \frac{2\,|\omega_r|}{\pi}. \tag{3.19}$$

The nonlinear system in (3.14) is then asymptotically stable at the equilibrium point (3.16) if k satisfies the condition (3.19), considering a target with a constant heading rate ω_r.

Furthermore, the steady-state distance can be regulated through the proper tuning of the controller gain. Inverting the first equation of (3.16), the required gain for the desired steady-state distance d^* to be achieved is given by:

$$k = \frac{\omega_r}{\arcsin\left(\frac{d^*\omega_r}{2V_\mathrm{r}}\right)}. \tag{3.20}$$

From the condition on the lower bound for the controller gain (3.19), the maximum distance that can be achieved is given by

$$(d_{eq})_{\mathsf{max}} = d_{eq}\,(k = k_{\mathsf{min}}) = \frac{2V_\mathrm{r}}{\omega_r}\sin\left(\frac{\pi}{2}\right) = 2R_r \tag{3.21}$$

which is exactly the diameter of the reference trajectory.

Therefore, despite the singularity present in system (3.12), the basic proportional control law (3.13) leads to an asymptotically stable equilibrium point, as long as the initial conditions are such that the singularity is not approached. Furthermore, the most interesting feature of this application is that the steady-state distance can be regulated for a desired value d^*, with $d^* \in \left]0, \frac{2V_\mathrm{r}}{\omega_r}\right]$.

3.3.2 Introduction of the δ-control approach

After the line-of-sight approach presented in the previous subsection, the main problem of the singularity in the desired point – which arises in the tracking control problem for a constant speed unicycle-like vehicle – still holds. With a similar approach, a novel method will be derived in this section in order to completely avoid the singularity.

The proposed method is based on the introduction of a new variable, δ, to generate a vector colinear and with the same direction of the reference velocity. The new line-of-sight will be defined from the UAV to the tip of the new vector, $\boldsymbol{\delta}$, instead of the reference point itself. An adaptive $\delta = |\boldsymbol{\delta}|$ is then proposed in order to ensure the system never reaches the singularity. A new system error dynamics will be derived, similarly to the approach of the previous subsection, but now with the inclusion of variable δ.

Consider the geometry of the control problem introduced in the beginning of this chapter in Figure 3.1. Additionally, consider a new vector $\boldsymbol{\delta}$ with norm denoted by δ, with its origin in the reference point, and having the same heading as that of the reference velocity, χ_r. Hence, the new vector can be represented by $\boldsymbol{\delta} = \mathcal{R}\,(\chi_\mathrm{r})\begin{bmatrix}\delta & 0\end{bmatrix}^T$. Now consider the control approach from the previous subsection, but instead of

the direct line-of-sight vector definition – between the UAV and the reference point –, consider a relative vector that is the line-of-sight from the UAV to the tip of the new vector $\boldsymbol{\delta}$. This new relative vector, **z**, with norm $\rho = \|\mathbf{z}\|$, is given by the sum of the direct line-of-sight **d** with the new virtual vector $\boldsymbol{\delta}$, i.e.,

$$\mathbf{z} = \mathbf{p}_\mathsf{r} - \mathbf{p} + \boldsymbol{\delta} = \mathbf{d} + \boldsymbol{\delta}, \qquad \|\boldsymbol{\delta}\| = \delta > 0. \tag{3.22}$$

This new formulation of the tracking control problem is depicted in Figure 3.7.

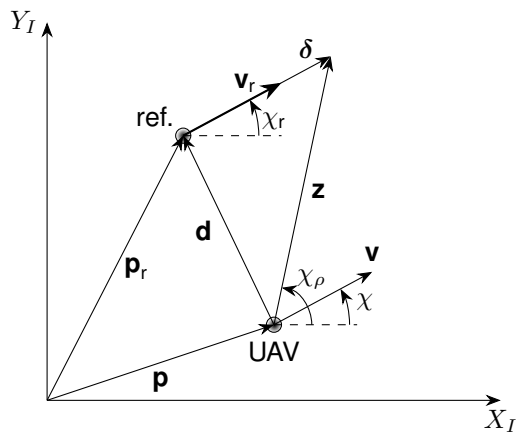

Figure 3.7: Geometry of the proposed tracking control approach, with the new variable δ

The heading of the relative vector **z**, here defined as χ_ρ, will be the desired heading for the proposed control methodology. This new approach allows avoiding the singularity when the UAV position coincides with that of the reference point. It can be noticed that, with the UAV on top of the reference point, the relative heading χ_ρ becomes exactly the reference heading χ_r.

If a small value of δ is considered, then, when the distance between the UAV and the reference point, d, is relatively large, i.e. $d \gg \delta$, the relative heading χ_ρ becomes nearly that of the direct line-of-sight, χ_d, represented in Figure 3.4. This intuitive approach, however, still does not solve the key problem, since the singularity is still present.

The benefit of a constant δ is that the singularity of the system is no longer at the reference point, i.e. when the UAV is on top of the reference point. However, for some positive constant δ, there is a set of possible initial conditions that can lead the system to the singularity, that corresponds to having the UAV position on the tip of the vector $\boldsymbol{\delta}$, and thus $\rho = 0$.

A possible solution for this problem is to set the constant value of δ large enough when compared to the given initial distance d. However, it is not trivial to prove that the distance d between the UAV and the reference point would not increase indefinitely, so that the system would approach the singularity anyway. Moreover, a very large constant value of δ would lead to a degradation of the control performance.

The approach proposed in this work is to have an adaptive δ, able to change its value according to the current distance, d, between the UAV and the reference point. In particular, the adaptive δ is defined as

$$\delta\left(d^2\right) = \varepsilon d^2 + R, \tag{3.23}$$

where ε and R are positive constants to be tuned later, after the controller is designed. From this definition, it is clear to see that vector $\boldsymbol{\delta}$ has a minimum value given by $\delta_{\mathsf{min}} = R$, attained when the UAV is above the reference point, and thus $d = 0$, and its norm increases with the distance. This is somewhat counterintuitive, and goes against the previous reasoning of having a small value of δ when the distance d is large, so that the relative heading χ_ρ would be nearly the heading of the line-of-sight χ_d. However, the approach proposed herein avoids the singularity of the other methods, as it will be explained in detail after the derivation of the new error dynamics.

3.3.2.1 Nominal system dynamics for a varying δ

Here the new error state dynamics will be derived, which will be considered as the nominal system for the purpose of this dissertation. The adopted formulation is similar to the one presented in subsec-

tion 3.3.1.1, but now the new variable δ and its dynamics will be considered, based on the problem formulation depicted in Figure 3.7.

Consider the relative vector **z**, defined in (3.22). This relative vector can also be written in inertial coordinates as $\mathbf{z} = \mathcal{R}(\chi_\rho)\begin{bmatrix}\rho & 0\end{bmatrix}^T$, and thus, both representations of vector **z** can be equated,

$$\mathcal{R}(\chi_\rho)\begin{bmatrix}\rho & 0\end{bmatrix}^T = \mathbf{p}_\mathrm{r} - \mathbf{p} + \boldsymbol{\delta}. \tag{3.24}$$

Now differentiating both sides of the previous equation with respect to time, and assuming the heading rate of the relative vector to be $\omega_\rho = \dot{\chi}_\rho$, it follows

$$\mathcal{S}(\omega_\rho)\mathcal{R}(\chi_\rho)\begin{bmatrix}\rho & 0\end{bmatrix}^T + \mathcal{R}(\chi_\rho)\begin{bmatrix}\dot{\rho} & 0\end{bmatrix}^T = V_\mathrm{r}\left[\mathcal{R}(\chi_\mathrm{r}) - \mathcal{R}(\chi)\right] + \delta\mathcal{S}(\omega_r)\mathcal{R}(\chi_r) + \dot{\delta}\mathcal{R}(\chi_r). \tag{3.25}$$

Consider a local reference frame $\{Z\}$, centered and fixed in the UAV position, with its X_Z axis aligned with the direction of **z**, as depicted in Figure 3.8.

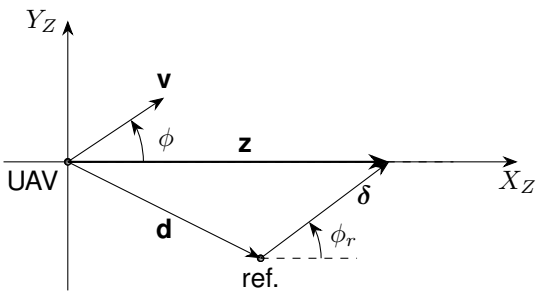

Figure 3.8: Geometry of the tracking control problem in the relative reference frame $\{Z\}$.

Here the angles ϕ_r and ϕ are defined differently from the previous section. From now on, consider $\phi_r = \chi_\mathrm{r} - \chi_\rho$ and $\phi = \chi - \chi_\rho$. Therefore, in order to represent (3.25) in reference frame $\{Z\}$, a rotation by an angle χ_ρ is applied, leading to:

$$\mathcal{R}^T(\chi_\rho)\left\{\mathcal{S}(\omega_\rho)\mathcal{R}(\chi_\rho)\begin{bmatrix}\rho\\0\end{bmatrix} + \mathcal{R}(\chi_\rho)\begin{bmatrix}\dot{\rho}\\0\end{bmatrix}\right\} = \mathcal{R}^T(\chi_\rho)\left\{V_\mathrm{r}\left[\mathcal{R}(\chi_\mathrm{r}) - \mathcal{R}(\chi)\right] + \delta\mathcal{S}(\omega_r)\mathcal{R}(\chi_r) + \dot{\delta}\mathcal{R}(\chi_r)\right\} \tag{3.26}$$

Applying some basic linear algebra to the previous equation, one get the expressions to properly define the relative vector dynamics, respectively the linear $\dot{\rho}$ and angular ω_ρ velocities,

$$\begin{bmatrix}\dot{\rho}\\ \rho\omega_\rho\end{bmatrix} = \begin{bmatrix}V_\mathrm{r}\cos\phi_r - V_\mathrm{r}\cos\phi - \delta\omega_r\sin\phi_r + \dot{\delta}\cos\phi_r\\ V_\mathrm{r}\sin\phi_r - V_\mathrm{r}\sin\phi + \delta\omega_r\cos\phi_r + \dot{\delta}\sin\phi_r\end{bmatrix} \tag{3.27}$$

From the relative formulation illustrated in Figure 3.8, it can be concluded that at least four state variables are required. The triangle formed by vectors **z**, **d**, and $\boldsymbol{\delta}$, needs three variables to be completely defined, without ambiguities. For the definition of this triangle, it will be considered the norm of the relative vector, ρ, and variables ϕ_r and δ representing vector $\boldsymbol{\delta}$. The norm of the remaining vector, d, can be written from the stated variables δ, ρ and ϕ_r, as it will be derived next. Additionally, variable ϕ should also be included in order to specify the direction of the UAV velocity.

Therefore, the considered state variables, fully describing the dynamics of interest of the system are

$$\mathbf{x} = \begin{bmatrix}\delta & \rho & \phi_r & \phi\end{bmatrix}^T \tag{3.28}$$

Now the time-derivatives of the state are defined in terms of the state variables, so that the system dynamics can be completely characterized without any exogenous terms. It is only left to find an expression for the derivative $\dot{\delta}$. Firstly, the norm of the difference vector between the UAV and the reference point is related with the state variables. By definition, the distance, d, can be written as

$$d = \sqrt{\left(x_\mathrm{r} - x\right)^2 + \left(y_\mathrm{r} - y\right)^2}. \tag{3.29}$$

Moreover, as the norm of a vector does not vary with the reference frame where it is represented, the previous equation can be rewritten as

$$d = \sqrt{\left[\left(x_{\mathsf{r}} - x\right)^{Z}\right]^2 + \left[\left(y_{\mathsf{r}} - y\right)^{Z}\right]^2}. \tag{3.30}$$

From Figure 3.8, it follows that $\left(x_{\mathsf{r}} - x\right)^{Z} = \rho - \delta\cos\phi_{\mathsf{r}}$ and $\left(y_{\mathsf{r}} - y\right)^{Z} = -\delta\sin\phi_{\mathsf{r}}$. The squared norm of the distance vector is then given by

$$\begin{aligned} d^2 &= \left(\rho - \delta\cos\phi_{\mathsf{r}}\right)^2 + \left(-\delta\sin\phi_{\mathsf{r}}\right)^2 \\ &= \rho^2 - 2\rho\delta\cos\phi_{\mathsf{r}} + \delta^2\cos^2\phi_{\mathsf{r}} + \delta^2\sin^2\phi_{\mathsf{r}} \\ &= \rho^2 + \delta^2 - 2\rho\delta\cos\phi_{\mathsf{r}} \end{aligned} \tag{3.31}$$

The time-derivative of the previous equation can be computed by considering the result of (3.27) and the time-derivative $\dot{\phi}_{\mathsf{r}} = \omega_{\mathsf{r}} - \omega_{\rho}$:

$$\begin{aligned} \frac{d}{dt}d^2 &= \frac{d}{dt}\left[\rho^2 + \delta^2 - 2\rho\delta\cos\phi_{\mathsf{r}}\right] \\ &= 2\dot{\rho}\left(\rho - \delta\cos\phi_{\mathsf{r}}\right) + 2\dot{\delta}\left(\delta - \rho\cos\phi_{\mathsf{r}}\right) + 2\rho\delta\dot{\phi}_{\mathsf{r}}\sin\phi_{\mathsf{r}} \\ &= 2\Bigg[\left(V_{\mathsf{r}}\cos\phi_{\mathsf{r}} - V_{\mathsf{r}}\cos\phi - \delta\omega_{\mathsf{r}}\sin\phi_{\mathsf{r}} + \dot{\delta}\cos\phi_{\mathsf{r}}\right)\left(\rho - \delta\cos\phi_{\mathsf{r}}\right) + \dot{\delta}\left(\delta - \rho\cos\phi_{\mathsf{r}}\right) \\ &\qquad + \rho\delta\omega_{\mathsf{r}}\sin\phi_{\mathsf{r}} - \delta\sin\phi_{\mathsf{r}}\left(V_{\mathsf{r}}\sin\phi_{\mathsf{r}} - V_{\mathsf{r}}\sin\phi + \delta\omega_{r}\cos\phi_{\mathsf{r}} + \dot{\delta}\sin\phi_{\mathsf{r}}\right)\Bigg] \\ &= 2\Bigg[\rho V_{\mathsf{r}}\left(\cos\phi_{\mathsf{r}} - \cos\phi\right) + \underbrace{\rho\delta\omega_{\mathsf{r}}\sin\phi_{\mathsf{r}} - \rho\delta\omega_{\mathsf{r}}\sin\phi_{\mathsf{r}}}_{=0} + \underbrace{\dot{\delta}\rho\cos\phi_{\mathsf{r}} - \dot{\delta}\rho\cos\phi_{\mathsf{r}}}_{=0} \\ &\qquad - \delta V_{\mathsf{r}}\big(\underbrace{\cos^2\phi_{\mathsf{r}} + \sin^2\phi_{\mathsf{r}}}_{=1}\big) + \underbrace{\delta^2\omega_{\mathsf{r}}\sin\phi_{\mathsf{r}}\cos\phi_{\mathsf{r}} - \delta^2\omega_{\mathsf{r}}\sin\phi_{\mathsf{r}}\cos\phi_{\mathsf{r}}}_{=0} \\ &\qquad + \delta V_{\mathsf{r}}\big(\underbrace{\cos\phi_{\mathsf{r}}\cos\phi + \sin\phi_{\mathsf{r}}\sin\phi}_{=\cos(\phi_{\mathsf{r}} - \phi)}\big) + \underbrace{\dot{\delta}\delta - \dot{\delta}\delta\big(\cos^2\phi_{\mathsf{r}} + \sin^2\phi_{\mathsf{r}}\big)}_{=0}\Bigg] \\ &= -2V_{\mathsf{r}}\Big[\rho\big(\cos\phi - \cos\phi_{\mathsf{r}}\big) + \delta\Big(1 - \cos\left(\phi_{\mathsf{r}} - \phi\right)\Big)\Big] \end{aligned} \tag{3.32}$$

Now from the previous result and from the definition of δ in (3.23), one can write

$$\dot{\delta} = \frac{d}{dt}\left(\varepsilon d^2 + R\right) = \varepsilon\frac{d}{dt}d^2 = -2\varepsilon V_{\mathsf{r}}\Big[\rho\big(\cos\phi - \cos\phi_{\mathsf{r}}\big) + \delta\Big(1 - \cos\left(\phi_{\mathsf{r}} - \phi\right)\Big)\Big]. \tag{3.33}$$

Hence, the nominal system dynamics is given by

$$\dot{\mathbf{x}} = \begin{bmatrix} \dot{\delta} \\ \dot{\rho} \\ \dot{\phi}_{\mathsf{r}} \\ \dot{\phi} \end{bmatrix} = \begin{bmatrix} -2\varepsilon V_{\mathsf{r}}\Big[\rho\big(\mathsf{c}\phi - \mathsf{c}\phi_{\mathsf{r}}\big) + \delta\big(1 - \mathsf{c}\phi\phi_{\mathsf{r}}\big)\Big] \\ V_{\mathsf{r}}\big(\mathsf{c}\phi_{\mathsf{r}} - \mathsf{c}\phi\big) - \delta\omega_{\mathsf{r}}\mathsf{s}\phi_{\mathsf{r}} - 2\varepsilon V_{\mathsf{r}}\mathsf{c}\phi_{\mathsf{r}}\Big[\rho\big(\mathsf{c}\phi - \mathsf{c}\phi_{\mathsf{r}}\big) + \delta\big(1 - \mathsf{c}\phi\phi_{\mathsf{r}}\big)\Big] \\ \omega_{\mathsf{r}} - \frac{1}{\rho}\big(V_{\mathsf{r}}\mathsf{s}\phi_{\mathsf{r}} - V_{\mathsf{r}}\mathsf{s}\phi + \delta\omega_{\mathsf{r}}\mathsf{c}\phi_{\mathsf{r}}\big) + 2\varepsilon V_{\mathsf{r}}\mathsf{s}\phi_{\mathsf{r}}\Big[\mathsf{c}\phi - \mathsf{c}\phi_{\mathsf{r}} + \frac{\delta}{\rho}\big(1 - \mathsf{c}\phi\phi_{\mathsf{r}}\big)\Big] \\ \omega - \frac{1}{\rho}\big(V_{\mathsf{r}}\mathsf{s}\phi_{\mathsf{r}} - V_{\mathsf{r}}\mathsf{s}\phi + \delta\omega_{\mathsf{r}}\mathsf{c}\phi_{\mathsf{r}}\big) + 2\varepsilon V_{\mathsf{r}}\mathsf{s}\phi_{\mathsf{r}}\Big[\mathsf{c}\phi - \mathsf{c}\phi_{\mathsf{r}} + \frac{\delta}{\rho}\big(1 - \mathsf{c}\phi\phi_{\mathsf{r}}\big)\Big] \end{bmatrix}, \tag{3.34}$$

where $\mathsf{c}\phi \triangleq \cos\phi$, $\mathsf{c}\phi_{\mathsf{r}} \triangleq \cos\phi_{\mathsf{r}}$, $\mathsf{s}\phi \triangleq \sin\phi$, $\mathsf{s}\phi_{\mathsf{r}} \triangleq \sin\phi_{\mathsf{r}}$ and $\mathsf{c}\phi\phi_{\mathsf{r}} \triangleq \cos\left(\phi - \phi_{\mathsf{r}}\right)$.

3.3.2.2 Singularity-free solution verification

From the resulting equations for the derived system dynamics (3.34), it can be concluded that the term $1/\rho$ is still present, and thus the formulation still has a singularity at $\rho = 0$. However, from the proposed definition of δ in (3.23), it can be proven that the states never reach the singularity, as long as a proper

selection of the constant parameters ε and R is made. In order to better understand the relation between the involved variables, consider the diagram of Figure 3.9:

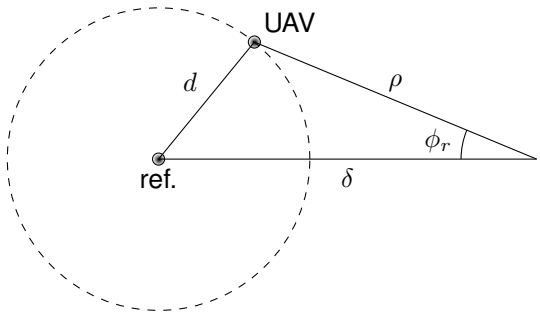

Figure 3.9: Resulting triangle relating the state variables δ, ρ, and ϕ_r with the distance d. Only the norms of the involved vectors are represented, in order to better understand the corresponding relations.

From Figure 3.9 and given δ should be always larger than d – from the proper relation between ε and R as will be described next –, it is clear that, for a given value of distance d, the minimum possible value of ρ will occur when both $\phi_r = 0$ and $\delta = d + \rho$. Note that the remaining state variable ϕ does not affect the positional relations, as it only describes the UAV orientation, which is not involved in the definition of the triangle in the previous figure. Moreover, from (3.23), the norm of the virtual vector $\boldsymbol{\delta}$ is $\delta = \varepsilon d^2 + R$. Hence, the minimum possible value of the variable ρ, for a given distance d, is given by

$$\rho_{\text{min}}(d) = \delta - d = \varepsilon d^2 + R - d. \tag{3.35}$$

Since the previous expression is a quadratic equation, and given $\varepsilon > 0$, the resulting geometric interpretation of $\rho_{\text{min}}(d)$ is a parabola with its aperture opened upwards. Thus, the value of the distance that leads to the minimum absolute value of ρ can be found from the differentiation

$$\frac{\partial}{\partial d}\rho_{\text{min}}(d) = 0 \Rightarrow 2\varepsilon d - 1 = 0 \Leftrightarrow d = \frac{1}{2\varepsilon}. \tag{3.36}$$

Replacing the resulting distance in (3.35), the minimum value of ρ is then $(\rho_{\text{min}})_{\text{min}} = R - \frac{1}{4\varepsilon}$. Therefore, it can be ensured that variable ρ has a proper lower-bound, with δ being always larger than d, and, thus, that the system never reaches the singularity, as long as the constant paramenters ε and R are chosen such that

$$R > \frac{1}{4\varepsilon}. \tag{3.37}$$

Moreover, with the geometry depicted in Figure 3.9, an upper-bound can be found for variable ϕ_r. For a given distance d, and for given values of ε and R, the maximum value of ϕ_r corresponds to the case in which vector **d** is perpendicular to **z** and, thus, forming a right triangle, with the maximum value of ϕ_r being given by

$$(\phi_r)_{\text{max}}(d) = \arcsin\left(\frac{d}{\varepsilon d^2 + R}\right). \tag{3.38}$$

3.3.2.3 Desired point definition

As previously stated, the control objective of the present problem is that of steering the UAV to track a given feasible reference point. Hence, the desired point in this formulation corresponds to a null vector **d**, that is achieved when the relative vector **z** matches vector $\boldsymbol{\delta}$, both in module, $\rho = \delta$, and in direction, having $\phi_r = 0$. Additionally, for the continuous tracking of the reference point, the UAV velocity vector should also equal the reference velocity $\mathbf{v}_r$, thus leading to $\phi = 0$. Therefore, in order for these conditions to be satisfied, and considering the definition of variable δ in (3.23), the desired state for the system of

the current tracking problem is given by

$$\mathbf{x}_d = \begin{bmatrix} \delta \\ \rho \\ \phi_r \\ \phi \end{bmatrix}_d = \begin{bmatrix} R \\ R \\ 0 \\ 0 \end{bmatrix}. \tag{3.39}$$

3.3.2.4 State variables transformation

The system dynamics in (3.34) model the relative motion between the pursuer and the target vehicles. This model is essentially useful for controller design, which will be described in the following sections, and can be derived from the given configurations in the inertial reference frame of both the UAV, (x, y, χ), and the reference point, $(x_\mathsf{r}, y_\mathsf{r}, \chi_\mathsf{r})$, as well as on the constant parameters (ε, R). Hence, we summarize here the expressions to compute the state variables $\mathbf{x} = \begin{bmatrix} \delta & \rho & \phi_r & \phi \end{bmatrix}^T$ from the given information:

1. $d = \sqrt{\left(x_\mathsf{r} - x\right)^2 + \left(y_\mathsf{r} - y\right)^2}$
2. $\delta = \varepsilon d^2 + R$
3. $\rho = \sqrt{\left(x_\mathsf{r} - x + \delta \cos \chi_\mathsf{r}\right)^2 + \left(y_\mathsf{r} - y + \delta \sin \chi_\mathsf{r}\right)^2}$
4. $\chi_\mathsf{r} = \arctan 2\left[\left(y_\mathsf{r} - y + \delta \sin \chi_\mathsf{r}\right), \left(x_\mathsf{r} - x + \delta \cos \chi_\mathsf{r}\right)\right]$
5. $\phi_r = \chi_\mathsf{r} - \chi_\rho$
6. $\phi = \chi - \chi_\rho$

3.4 Lyapunov-based controller

The control objective defined earlier in this chapter is to follow the trajectory of a reference point, which is considered to have a feasible motion for the pursuer vehicle. Hence, the tracking objective is depicted by ensuring that both $\mathbf{d} \to \mathbf{0}$ and $\chi \to \chi_\mathsf{r}$.

In order to simplify the tracking control problem, new variables were defined specifying the relative motion of the system composed by the pursuer and the reference point. With the derived relative motion, we were able to reduce the number of state variables from six to four, respectively

$$\begin{bmatrix} x & y & \chi & x_\mathsf{r} & y_\mathsf{r} & \chi_\mathsf{r} \end{bmatrix}^T \to \begin{bmatrix} \delta & \rho & \phi_\mathsf{r} & \phi \end{bmatrix}^T. \tag{3.40}$$

Initially only three state variables were considered, ρ, ϕ_r and ϕ. However, a novel control approach was proposed with the introduction of the new variable δ, in order to avoid the existing singularity inherent to the posed tracking problem.

Therefore, the derived relative motion will be considered for the controller derivation, with the control objective being now defined as $\mathbf{x} \to \mathbf{x}_d$, where $\mathbf{x}$ is the previously defined state vector $\mathbf{x} = \begin{bmatrix} \delta & \rho & \phi_\mathsf{r} & \phi \end{bmatrix}^T$, and $\mathbf{x}_d$ is given by equation (3.39).

With the speed and altitude of the UAV being assumed to be controlled by an inner-loop control module, the only control input that is available is the UAV heading rate, and thus, $u = \omega$.

Here a steering control law will be derived, acting only on the UAV heading rate, being able to lead the four-state model to the desired equilibrium point, and thus leading the UAV to the reference trajectory. Stability will be proved through the use of the Lyapunov theory.

Firstly, looking upon the control objective of leading the distance d to zero, and regarding only the state variables associated with the positional relations of the system, here defined as $\mathbf{x}_1 = (\delta, \rho, \phi_\mathsf{r})$ and which are not directly controllable, consider the Lyapunov function candidate

$$V_1\left(\mathbf{x}_1\right) = \frac{1}{2} d^2\left(\mathbf{x}_1\right) = \frac{1}{2}\left(\rho^2 + \delta^2 - 2\rho\delta \cos \phi_r\right) \tag{3.41}$$

In order to guarantee stability, a Lyapunov function must be positive definite and its derivative must be at least negative semi-definite (Theorem 4.1 in [66]). Checking the requirement of positive-definiteness for V_1,

- $V_1\left(\mathbf{x}_1 = \mathbf{x}_{1_d}\right) = 0,$ with $\mathbf{x}_{1_d} = (\delta, \rho, \phi_\mathsf{r})_d = (R, R, 0)$
- $V_1\left(\mathbf{x}_1\right) > 0 \;\; \forall\, \mathbf{x}_1 \neq \mathbf{x}_{1_d},$ because V_1 is a quadratic function

Hence $V_1\left(\mathbf{x}_1\right)$ is a positive definite function, and its derivative should be evaluated. From the result of (3.32) the derivative of $V_1\left(\mathbf{x}_1\right)$ becomes

$$\begin{aligned}\dot{V}_1\left(\mathbf{x}_1\right) &= -\rho V_\mathsf{r}\big(\cos\phi - \cos\phi_\mathsf{r}\big) - \delta V_\mathsf{r}\Big(1 - \cos\big(\phi_\mathsf{r} - \phi\big)\Big)\\ &= -\rho V_\mathsf{r}\big(\cos\phi - \cos\phi_\mathsf{r}\big) - \delta V_\mathsf{r}\Big(1 - \cos\big(\phi_\mathsf{r} - \phi\big)\Big) \pm \rho V_\mathsf{r}\\ &= -\rho V_\mathsf{r}\big(1 - \cos\phi_\mathsf{r}\big) - \delta V_\mathsf{r}\Big(1 - \cos\big(\phi_\mathsf{r} - \phi\big)\Big) + \rho V_\mathsf{r}\big(1 - \cos\phi\big).\end{aligned} \tag{3.42}$$

The derivative $\dot{V}_1$ is not necessarily negative and thus the function V_1 can not be considered a Lyapunov function, which was already expected since it considers the uncontrolled system.

However, from the expression of derivative $\dot{V}_1$, one can figure that V_1 and thus the distance d are always decreasing whenever the variable ϕ is zero. That is, whenever the UAV velocity **v** is aligned with the relative vector **z**, we can ensure the system is approaching the desired state. Therefore, we should build a controller that can lead ϕ to zero, and maintain $\phi(t) \equiv 0$.

Consider the control law

$$\omega = -\,k_1 \rho V_\mathsf{r} \frac{\sin\phi}{1 + \cos\phi} + \omega_\rho, \tag{3.43}$$

where

$$\omega_\rho = \frac{1}{\rho}\big(V_\mathsf{r}\mathsf{s}\phi_\mathsf{r} - V_\mathsf{r}\mathsf{s}\phi + \delta\omega_\mathsf{r}\mathsf{c}\phi_\mathsf{r}\big) - 2\varepsilon V_\mathsf{r}\mathsf{s}\phi_\mathsf{r}\left[\mathsf{c}\phi - \mathsf{c}\phi_\mathsf{r} + \frac{\delta}{\rho}\big(1 - \mathsf{c}\phi\phi_\mathsf{r}\big)\right]. \tag{3.44}$$

With controller (3.43), the closed-loop system (3.34) becomes

$$\dot{\mathbf{x}} = \begin{cases} \dot{\delta} &= -2\varepsilon V_\mathsf{r}\Big[\rho\big(\mathsf{c}\phi - \mathsf{c}\phi_\mathsf{r}\big) + \delta\big(1 - \mathsf{c}\phi\phi_\mathsf{r}\big)\Big]\\ \dot{\rho} &= V_\mathsf{r}\big(\mathsf{c}\phi_\mathsf{r} - \mathsf{c}\phi\big) - \delta\omega_\mathsf{r}\mathsf{s}\phi_\mathsf{r} - 2\varepsilon V_\mathsf{r}\mathsf{c}\phi_\mathsf{r}\Big[\rho\big(\mathsf{c}\phi - \mathsf{c}\phi_\mathsf{r}\big) + \delta\big(1 - \mathsf{c}\phi\phi_\mathsf{r}\big)\Big]\\ \dot{\phi}_\mathsf{r} &= \omega_\mathsf{r} - \tfrac{1}{\rho}\big(V_\mathsf{r}\mathsf{s}\phi_\mathsf{r} - V_\mathsf{r}\mathsf{s}\phi + \delta\omega_\mathsf{r}\mathsf{c}\phi_\mathsf{r}\big) + 2\varepsilon V_\mathsf{r}\mathsf{s}\phi_\mathsf{r}\Big[\mathsf{c}\phi - \mathsf{c}\phi_\mathsf{r} + \tfrac{\delta}{\rho}\big(1 - \mathsf{c}\phi\phi_\mathsf{r}\big)\Big]\\ \dot{\phi} &= -k_1\rho V_\mathsf{r}\tfrac{\sin\phi}{1+\cos\phi}\end{cases} \tag{3.45}$$

Evaluating the controlled system in the desired point (3.39) we find that $\mathbf{x}_d$ is an equilibrium point of (3.45). Now a composite Lyapunov function candidate for the whole system can be defined as

$$V_2\left(\mathbf{x}\right) = V_1\left(\mathbf{x}_1\right) + k_2\big(1 - \cos\phi\big). \tag{3.46}$$

This new function also satisfies the positive-definiteness requirements. Considering the controlled system (3.45), the time-derivative of V_2 is then given by

$$\begin{aligned}\dot{V}_2\left(\mathbf{x}\right) &= \dot{V}_1\left(\mathbf{x}_1\right) + k_2\dot{\phi}\sin\phi\\ &= \dot{V}_1\left(\mathbf{x}_1\right) - k_1k_2\rho V_\mathsf{r}\frac{\sin^2\phi}{1+\cos\phi}\\ &= \dot{V}_1\left(\mathbf{x}_1\right) - k_1k_2\rho V_\mathsf{r}\frac{1-\cos^2\phi}{1+\cos\phi}\\ &= \dot{V}_1\left(\mathbf{x}_1\right) - k_1k_2\rho V_\mathsf{r}\frac{\big(1-\cos\phi\big)\big(1+\cos\phi\big)}{1+\cos\phi}\\ &= -\rho V_\mathsf{r}\big(1 - \cos\phi_\mathsf{r}\big) - \delta V_\mathsf{r}\Big(1 - \cos\big(\phi_\mathsf{r} - \phi\big)\Big) + \rho V_\mathsf{r}\big(1 - \cos\phi\big) - k_1k_2\rho V_\mathsf{r}\big(1 - \cos\phi\big)\\ &= -\rho V_\mathsf{r}\big(1 - \cos\phi_\mathsf{r}\big) - \delta V_\mathsf{r}\Big(1 - \cos\big(\phi_\mathsf{r} - \phi\big)\Big) - \rho V_\mathsf{r}\big(1 - \cos\phi\big)\big(k_1k_2 - 1\big).\end{aligned} \tag{3.47}$$

Choosing k_2 such that $k_1 k_2 = 1$ we get a negative semidefinite derivative,

$$\dot{V}_2\left(\mathbf{x}\right) = -\rho V_{\mathsf{r}}\big(1 - \cos\phi_{\mathsf{r}}\big) - \delta V_{\mathsf{r}}\Big(1 - \cos\left(\phi_{\mathsf{r}} - \phi\right)\Big) \leq 0. \tag{3.48}$$

Hence, the requirements for considering $V_2\left(\mathbf{x}\right)$ a Lyapunov function are fulfilled and stability of system (3.34) is guaranteed with controller (3.43).

However, the weaker condition of negative semidefiniteness of the Lyapunov function derivative alone is not enough to prove asymptotic stability of the system, and further analysis should be made.

In a first and more restrictive analysis, considering a constant reference heading rate ω_{r}, the system (3.45) is autonomous and the *LaSalle's Invariance Principle* can be applied to prove asymptotical stability. Note that the controller (3.43) is not defined when $\cos\phi = -1$, that happens when the UAV velocity $\mathbf{v}$ has exactly the opposite direction of the relative vector $\mathbf{z}$. For now, this restriction implies that the full state-space can not be considered, and a global result cannot be obtained, however this restriction will be assessed later.

Now, let $D = \{\mathbf{x} \in \mathbb{R} : \cos\phi \neq -1\}$. To find $S = \Big\{\mathbf{x} \in D : \dot{V}_2(\mathbf{x}) = 0\Big\}$, note that

$$\dot{V}_2(\mathbf{x}) = 0 \Rightarrow \phi_{\mathsf{r}}, \phi = 0, \tag{3.49}$$

thus $S = \{\mathbf{x} \in D : \phi_{\mathsf{r}}, \phi = 0\}$. Now let $\mathbf{x}(t)$ be a solution that belongs identically to S:

$$\phi_{\mathsf{r}}(t), \phi(t) \equiv 0 \Rightarrow \dot{\phi}_{\mathsf{r}}(t) \equiv 0 \Rightarrow \omega_{\mathsf{r}}\left(1 - \frac{\delta}{\rho}\right) \equiv 0 \Leftrightarrow \omega_{\mathsf{r}} \equiv 0 \vee \rho \equiv \delta \tag{3.50}$$

Hence, as a straight-line reference trajcetory, $w_{\mathsf{r}} = 0$, is not considered, the only solution that can stay identically in the set S is the trivial solution $\mathbf{x}(t) = \mathbf{x}_d$. Therefore, from the Corollary (4.1) in [66], the system is asymptotically stable, meaning that $\mathbf{x}_0 \in D \Rightarrow \mathbf{x}(t) \to \mathbf{x}_d$ as $t \to \infty$.

For a more general analysis, the reference heading rate should not be restricted to a constant value, so the results can be applied for a broader range of reference trajectories, such as the ones generated in the previous chapter 2. When a time-varying reference heading rate $\omega_{\mathsf{r}}(t)$ is considered, the system (3.45) becomes a non-autonomous system, and thus the *LaSalle's Invariance Principle* cannot be applied anymore. Instead, in order to obtain similar results for a non-autonomous system, the *Barbalat's Lemma* – well defined in [68] (Lemma 4.2) – can be applied.

For the following analysis consider a time-varying bounded reference heading rate $\omega_{\mathsf{r}}(t)$, with a bounded time-derivative $\dot{\omega}_{\mathsf{r}}(t)$, which leads to the following non-autonomous system:

$$\dot{\mathbf{x}}\big(\mathbf{x}, t\big) = \begin{cases} \dot{\delta} & = -2\varepsilon V_{\mathsf{r}}\Big[\rho\big(\mathsf{c}\phi - \mathsf{c}\phi_{\mathsf{r}}\big) + \delta\big(1 - \mathsf{c}\phi\phi_{\mathsf{r}}\big)\Big] \\ \dot{\rho} & = V_{\mathsf{r}}\big(\mathsf{c}\phi_{\mathsf{r}} - \mathsf{c}\phi\big) - \delta\omega_{\mathsf{r}}(t)\mathsf{s}\phi_{\mathsf{r}} - 2\varepsilon V_{\mathsf{r}}\mathsf{c}\phi_{\mathsf{r}}\Big[\rho\big(\mathsf{c}\phi - \mathsf{c}\phi_{\mathsf{r}}\big) + \delta\big(1 - \mathsf{c}\phi\phi_{\mathsf{r}}\big)\Big] \\ \dot{\phi}_{\mathsf{r}} & = \omega_{\mathsf{r}}(t) - \frac{1}{\rho}\big(V_{\mathsf{r}}\mathsf{s}\phi_{\mathsf{r}} - V_{\mathsf{r}}\mathsf{s}\phi + \delta\omega_{\mathsf{r}}(t)\mathsf{c}\phi_{\mathsf{r}}\big) + 2\varepsilon V_{\mathsf{r}}\mathsf{s}\phi_{\mathsf{r}}\Big[\mathsf{c}\phi - \mathsf{c}\phi_{\mathsf{r}} + \frac{\delta}{\rho}\big(1 - \mathsf{c}\phi\phi_{\mathsf{r}}\big)\Big] \\ \dot{\phi} & = -k_1\rho V_{\mathsf{r}}\frac{\sin\phi}{1+\cos\phi} \end{cases} \tag{3.51}$$

In order to assess the asymptotic stability of this non-autonomous system, consider again the Lyapunov function $V_2\big(\mathbf{x}\big)$ (3.46) with time-derivative $\dot{V}_2\big(\mathbf{x}\big)$ (3.48).

While the *LaSalle's Invariance Principle* restricts its application to autonomous system, the *Lyapunov-Like Lemma* stated in [68] (Lemma 4.3) can be applied to non-autonomous systems, achieving similar results, under further conditions for the considered Lyapunov function. It states that if the Lyapunov function $V_2\big(\mathbf{x}\big)$ satisfies the conditions

- $V_2\big(\mathbf{x}\big)$ is lower bounded,
- $\dot{V}_2\big(\mathbf{x}\big)$ is negative semi-definite,
- $\dot{V}_2\big(\mathbf{x}\big)$ is uniformly continuous in time,

then $\dot{V}_2\big(\mathbf{x}\big) \to 0$ as $t \to \infty$.

The first two conditions are verified from the definition of Lyapunov function. The negative semidefiniteness of the derivative $\dot{V}_2(\mathbf{x})$ implies that $V_2(t) \leq V_2(t_0), \ \ \forall t > t_0$, and hence, that ρ, ϕ_r, ϕ and δ are bounded.

To check whether $\dot{V}_2$ is uniformly continuous, its derivative should be found,

$$\ddot{V}_2 = -V_\mathsf{r}\left[\dot{\rho}\big(1-\cos\phi_\mathsf{r}\big) + \rho\dot{\phi}_\mathsf{r}\sin\phi_\mathsf{r} + \big(\dot{\phi}_\mathsf{r}-\dot{\phi}\big)\delta\sin\big(\phi_\mathsf{r}-\phi\big) + \dot{\delta}\Big(1-\cos\big(\phi_\mathsf{r}-\phi\big)\Big)\right]. \tag{3.52}$$

Since $\omega_\mathsf{r}(t)$ is bounded by hypothesis, and the state variables were shown to be bounded, then the state derivatives $\dot{\delta}$, $\dot{\rho}$, $\dot{\phi}_\mathsf{r}$ and $\dot{\phi}$ are also bounded. Hence, $\ddot{V}_2$ is bounded, implying that $\dot{V}_2$ is uniformly continuous in time.

With all the conditions satisfied, the *Lyapunov-Like Lemma* [68] can be applied, proving that $t \to \infty \Rightarrow \dot{V}_2(\mathbf{x},t) \to 0$. From the expression for the Lyapunov function derivative (3.48) it follows that

$$\dot{V}_2(\mathbf{x},t) \to 0 \Rightarrow \phi_\mathsf{r}(t), \phi(t) \to 0. \tag{3.53}$$

Now, given the time-dependency of the system, the implication $\phi_\mathsf{r}(t) \to 0 \Rightarrow \dot{\phi}_\mathsf{r}(t) \to 0$ cannot be readly assumed. However, it can be confirmed applying *Barbalat's Lemma* [68] to function $\dot{\phi}_\mathsf{r}(\mathbf{x},t)$:

$$\dot{\phi}_\mathsf{r}(\mathbf{x},t) = \omega_\mathsf{r}(t) - \frac{1}{\rho}\big(V_\mathsf{r}\mathsf{s}\phi_\mathsf{r} - V_\mathsf{r}\mathsf{s}\phi + \delta\omega_\mathsf{r}(t)\mathsf{c}\phi_\mathsf{r}\big) + 2\varepsilon V_\mathsf{r}\mathsf{s}\phi_\mathsf{r}\left[\mathsf{c}\phi - \mathsf{c}\phi_\mathsf{r} + \frac{\delta}{\rho}\big(1-\mathsf{c}\phi\phi_\mathsf{r}\big)\right] \tag{3.54}$$

In order to evaluate the time evolution of $\dot{\phi}_\mathsf{r}$ consider its derivative:

$$\begin{aligned}\ddot{\phi}_\mathsf{r}(t) = \dot{\omega}_\mathsf{r}(t) &+ \frac{1}{\rho^2}\left[V_\mathsf{r}\mathsf{s}\phi_\mathsf{r} - V_\mathsf{r}\mathsf{s}\phi + \delta\omega_\mathsf{r}(t)\mathsf{c}\phi_\mathsf{r}\right] - \frac{1}{\rho}\left[V_\mathsf{r}\dot{\phi}_\mathsf{r}\mathsf{c}\phi_\mathsf{r} - V_\mathsf{r}\dot{\phi}\mathsf{c}\phi + \dot{\delta}\omega_\mathsf{r}(t)\mathsf{c}\phi_\mathsf{r} + \delta\dot{\omega}_\mathsf{r}(t)\mathsf{c}\phi_\mathsf{r} - \delta\omega_\mathsf{r}(t)\dot{\phi}_\mathsf{r}\mathsf{s}\phi_\mathsf{r}\right] \\ &+ 2\varepsilon V_\mathsf{r}\dot{\phi}_\mathsf{r}\mathsf{c}\phi_\mathsf{r}\left[\mathsf{c}\phi - \mathsf{c}\phi_\mathsf{r} + \frac{\delta}{\rho}\big[1-\cos(\phi_\mathsf{r}-\phi)\big]\right] \\ &+ 2\varepsilon V_\mathsf{r}\mathsf{s}\phi_\mathsf{r}\left[-\dot{\phi}\mathsf{s}\phi + \dot{\phi}_\mathsf{r}\mathsf{s}\phi_\mathsf{r} + \frac{\dot{\delta}\rho - \delta\dot{\rho}}{\rho^2}\left[1-\cos(\phi_\mathsf{r}-\phi)\right] + \frac{\delta V_\mathsf{r}}{\rho}\big(\dot{\phi}_\mathsf{r}-\dot{\phi}\big)\sin(\phi_\mathsf{r}-\phi)\right]\end{aligned} \tag{3.55}$$

The *Barbalat's Lemma* [68] can then be applied, since the state variables and derivatives are bounded, as shown above, and given the boundedness of the reference heading rate derivative, $\dot{\omega}_\mathsf{r}(t)$. Note that it is here assumed the boundedness of the term $1/\rho$, which is achieved by a proper tuning of variables ε and R, as stated in condition (3.37). Hence, it is proved that if ϕ_r converges to zero as $t \to \infty$, then $\dot{\phi}_\mathsf{r}$ also converges to zero, i.e.,

$$\phi_\mathsf{r}(t) \to 0 \Rightarrow \dot{\phi}_\mathsf{r}(t) \to 0. \tag{3.56}$$

Therefore, given $\phi_\mathsf{r}(t), \phi(t), \dot{\phi}_\mathsf{r}(t) \to 0$ as $t \to \infty$, from equation (3.54) we get $\rho(t) \to \delta(t)$, as long as $\omega_\mathsf{r}(t) \neq 0$. By definition in the problem formulation, $\rho(t) \to \delta(t)$ implies that $d(t) \to 0$ and thus $\delta(t) \to R$. Hence, it is proved that $\mathbf{x}_0 \in D \Rightarrow \mathbf{x}(t) \to \mathbf{x}_d$ as $t \to \infty$, and then, the non-autonomous closed-loop system (3.51) is also asymptotically stable.

The concept of asymptotical stability is commonly used to denote for local asymptotical stability, where a local region of attraction is usually defined and the stability is only guaranteed for initial conditions starting in that restricted region. The results obtained in the present section also hold for a restricted region for the initial state of the system. However, the only existing restriction is due to the considered control law (3.43), which is not defined for $\phi = \pi$. Thus, it has a wider range then the usual problems were local asymptotic stability is reached only for a minor region around the equilibrium point. Here the region of atraction is almost the full state-space, and given the dynamics of the derivative $\dot{\phi}$, as long as the initial state verifies the condition of $\cos\phi \neq -1$, then the system never reaches this point. Therefore, we can denote the equilibrium point (3.39) of the controlled system (3.45) as *almost globally asymptotically stable*.

3.5 Nonlinear cascade system approach for a class of generic controllers

Despite the Lyapunov method being able to give sufficient conditions to prove stability of nonlinear systems, the definition of a Lyapunov function for the full system is not a necessary condition to prove global stability. Hence, several options are available in literature to give sufficient conditions to prove global stability of nonlinear systems, through the definition of weaker requirements on candidate Lyapunov functions.

Moreover, the results achieved in the analysis of the previous section, mainly the one inferred from the derivative of function V_1 (3.42), suggests that a wider range of controllers are suitable for the given control problem. Therefore, the assumption whose validity will be pursued in the present section is that if the error distance between the UAV and the reference point converges to zero whenever the variable ϕ is zero, and once the available control input ω is able to control directly the dynamics $\dot{\phi}$, then one should find a controller that can enforce an asymptotical convergence of ϕ to zero. The following analysis is based on the concept of *Input-to-State Stability* introduced in [66].

In order to generalize the problem at hand, consider the class of controllers described by

$$\omega\big(t, \mathbf{x}\big) = -h(\phi) + \omega_\rho\big(t, \mathbf{x}\big), \tag{3.57}$$

where $h(\phi)$ must satisfy $h(0) = 0$, $\phi h(\phi) > 0$, $\forall \phi \in [-\pi, \pi]$, and $\omega_\rho\big(\mathbf{x}\big)$ is given by equation (3.44).

Then, system (3.34) in closed-loop with a controller of the type (3.57) becomes

$$\dot{\mathbf{x}}\,(t, \mathbf{x}) = \begin{bmatrix} -2\varepsilon V_\mathsf{r}\Big[\rho\big(\mathsf{c}\phi - \mathsf{c}\phi_\mathsf{r}\big) + \delta\big(1 - \mathsf{c}\phi\phi_\mathsf{r}\big)\Big] \\ V_\mathsf{r}\big(\mathsf{c}\phi_\mathsf{r} - \mathsf{c}\phi\big) - \delta\omega_\mathsf{r}(t)\mathsf{s}\phi_\mathsf{r} - 2\varepsilon V_\mathsf{r}\mathsf{c}\phi_\mathsf{r}\Big[\rho\big(\mathsf{c}\phi - \mathsf{c}\phi_\mathsf{r}\big) + \delta\big(1 - \mathsf{c}\phi\phi_\mathsf{r}\big)\Big] \\ \omega_\mathsf{r}(t) - \frac{1}{\rho}\big(V_\mathsf{r}\mathsf{s}\phi_\mathsf{r} - V_\mathsf{r}\mathsf{s}\phi + \delta\omega_\mathsf{r}(t)\mathsf{c}\phi_\mathsf{r}\big) + 2\varepsilon V_\mathsf{r}\mathsf{s}\phi_\mathsf{r}\Big[\mathsf{c}\phi - \mathsf{c}\phi_\mathsf{r} + \frac{\delta}{\rho}\big(1 - \mathsf{c}\phi\phi_\mathsf{r}\big)\Big] \\ -h(\phi) \end{bmatrix} \tag{3.58}$$

The resulting closed-loop system suggests that a different representation can be considered, given the independency of derivative $\dot{\phi}$ on the remaining state variables. Hence, consider the previous controlled system, now represented as a nonliner cascade system of the form

$$\dot{\mathbf{x}}_1 = f_1(t, \mathbf{x}_1, \mathbf{x}_2), \tag{3.59a}$$
$$\dot{\mathbf{x}}_2 = f_2(\mathbf{x}_2), \tag{3.59b}$$

where $\mathbf{x}_1 = \begin{bmatrix}\delta & \rho & \phi_\mathsf{r}\end{bmatrix}^T$ and $\mathbf{x}_2 = \phi$.

As described in [66], Lemma 4.7, the global stability of this kind of cascade systems can be assessed if either subsystem (3.59a) is input-to-state stable, having $\mathbf{x}_2$ as input, and if subsytem (3.59b) is globally asymptotically stable.

Thus, in order to assess the requirements for the previous system to be input-to-state stable, one should first evaluate the stability of the unforced system

$$\dot{\mathbf{x}}_1 = f_1(t, \mathbf{x}_1, 0) = \begin{cases} \dot{\delta} & = -2\varepsilon\big(\rho + \delta\big)\big(1 - \mathsf{c}\phi_\mathsf{r}\big) \\ \dot{\rho} & = -V_\mathsf{r}\big(1 - \mathsf{c}\phi_\mathsf{r}\big) - \delta\omega_\mathsf{r}(t)\mathsf{s}\phi_\mathsf{r} - 2\varepsilon V_\mathsf{r}\mathsf{c}\phi_\mathsf{r}\big(\rho + \delta\big)\big(1 - \mathsf{c}\phi_\mathsf{r}\big) \\ \dot{\phi}_\mathsf{r} & = \omega_\mathsf{r}(t) - \frac{1}{\rho}\Big[V_\mathsf{r}\mathsf{s}\phi_\mathsf{r} + \delta\omega_\mathsf{r}(t)\mathsf{c}\phi_\mathsf{r} - 2\varepsilon V_\mathsf{r}\mathsf{s}\phi_\mathsf{r}\big(\rho + \delta\big)\big(1 - \mathsf{c}\phi_\mathsf{r}\big)\Big] \end{cases}. \tag{3.60}$$

Now recall the Lyapunov function candidate (3.41) introduced in previous section,

$$V_1\left(\mathbf{x}_1\right) = \frac{1}{2}d^2\left(\mathbf{x}_1\right) = \frac{1}{2}\left(\rho^2 + \delta^2 - 2\rho\delta\cos\phi_\mathsf{r}\right). \tag{3.61}$$

Evaluating its derivative over the unforced system (3.60), one gets

$$\begin{aligned}\dot{V}_1\left(\mathbf{x}_1\right) &= \Big[-\rho V_{\mathsf{r}}\big(1-\cos\phi_{\mathsf{r}}\big) - \delta V_{\mathsf{r}}\Big(1-\cos\big(\phi_{\mathsf{r}}-\phi\big)\Big) + \rho V_{\mathsf{r}}\big(1-\cos\phi\big)\Big]_{\phi=0} \\ &= -V_{\mathsf{r}}\big(\rho+\delta\big)\big(1-\cos\phi_{\mathsf{r}}\big) \leq 0\ .\end{aligned} \tag{3.62}$$

The resulting derivative $\dot{V}_1$ is negative semidefinite, and thus, V_1 is a Lyapunov function for the unforced system (3.60). However, the input-to-state stability condition requires a negative derivative of the Lyapunov function, as stated in Theorem 4.19 in [66], and thus it cannot be applied to the considered system.

This strong requirement of having a negative definite derivative of the Lyapunov function is always present in the conditions of [66] for input-to-state stability, and it is a very restrictive condition that may not be assessed by some kind of systems, such as the one considered here. However, there are several authors presenting some sufficient conditions to prove global asymptotic stability of cascade systems where only a negative semidefinite Lyapunov function derivative is achievable.

While some authors consider the global stability of nonlinear autonomous cascade systems, [69, 70, 71], others go even further and present sufficient conditions for nonlinear time-varying cascade systems [72, 73, 74]. As explained in the previous section, the considered system can be either autonomous or non-autonomous, depending on the reference heading rate ω_r that can be constant or time-varying $\omega_r(t)$, respectively. Given the similarity of the results in the referred papers, either for autonomous or non-autonomous cascade systems, the more inclusive case of the time-varying reference heading rate $\omega_r(t)$ will be considered and, thus, the non-autonomuos cascade system (3.59).

Therefore, the global asymptotic stability of the controlled system around the equilibrium $\mathbf{x}_d$ is achieved if both systems (3.59b) and (3.60) are globally asymptotically stable and also if all the trajectories of the system are bounded.

The first condition for the global asymptotic stability of the origin of (3.59b) is straightforward since $\dot{\mathbf{x}}_2 = f(\mathbf{x}_2) = -h(\phi)$, and given the stated conditions for function $h(\phi)$.

In order to assess the condition for the global asymptotic stability of (3.60), consider again the Lyapunov function V_1, which has the following derivative, evaluated over the unforced system (3.60),

$$\dot{V}_1\left(\mathbf{x}_1\right) = -V_{\mathsf{r}}\big(\rho+\delta\big)\big(1-\cos\phi_{\mathsf{r}}\big) \leq 0\ . \tag{3.63}$$

Since $\dot{V}_1(\mathbf{x}_1) \leq 0$, then $V_1(t) \leq V_1(t_0)$ and hence $\mathbf{x}_1$ is bounded. To check whether $\dot{V}_1$ is uniformly continuous, its derivative should be found,

$$\ddot{V}_1\left(\mathbf{x}_1\right) = -V_{\mathsf{r}}\big(\dot{\rho}+\dot{\delta}\big)\big(1-\cos\phi_{\mathsf{r}}\big) - V_{\mathsf{r}}\big(\rho+\delta\big)\dot{\phi}_{\mathsf{r}}\sin\phi_{\mathsf{r}}\ . \tag{3.64}$$

Since $\omega_{\mathsf{r}}(t)$ is bounded by hypothesis, and the state variables $\mathbf{x}_1$ were shown to be bounded, then the state derivatives $\dot{\delta}$, $\dot{\rho}$ and $\dot{\phi}_{\mathsf{r}}$ are also bounded. Hence, $\ddot{V}_1$ is bounded, proving that $\dot{V}_1$ is uniformly continuous, and thus, from the *Lyapunov Like-Lemma* [68], it is proved that $\dot{V}_1(t,\mathbf{x}_1) \to 0$ as $t \to \infty$.

From the previous expression for $\dot{V}_1$, it follows that $\dot{V}_1(t,\mathbf{x}_1) \to 0 \Rightarrow \phi_{\mathsf{r}}(t) \to 0$. Using *Barbalat's Lemma* [68] as in the previous section, one proves also that $\phi_{\mathsf{r}}(t) \to 0 \Rightarrow \dot{\phi}_{\mathsf{r}}(t) \to 0$. Therefore, from the third equation in (3.60) it is proved that $\dot{\phi}_{\mathsf{r}}(t) \to 0 \Rightarrow \rho(t) \to \delta(t)$. Hence, it is proved that $\mathbf{x}_1(t) \to \mathbf{x}_{1_d}$ as $t \to \infty$ for any initial conditions, and thus, the equilibrium $\mathbf{x}_{1_d}$ is a globally asymptotically stable equilibrium of the unforced system (3.60).

Now it is only left to prove that all the trajectories of the full system (3.59) are bounded. This condition comes from the fact that subsystem (3.59a) does not explode when ϕ is not zero. In the worst situation, the distance can be always increasing while ϕ is converging to zero (through the dynamics of $\dot{\mathbf{x}}_2$), and if variable ϕ converges to zero very slowly, the distance d can increase significantly. However, from the result in (3.42), the derivative of Lyapunov function V_1 can be written in the form

$$\dot{V}_1(t,\mathbf{x}_1) = -\rho V_{\mathsf{r}}\big(\cos\phi - \cos\phi_{\mathsf{r}}\big) - \delta V_{\mathsf{r}}\Big(1-\cos\big(\phi-\phi_{\mathsf{r}}\big)\Big). \tag{3.65}$$

Thus, proceeding with the previous reasoning, when variable ϕ is converging to zero, there is a time instant after which $\phi \leq \phi_{\mathsf{r}}$, and thus $\cos\phi \geq \cos\phi_{\mathsf{r}}$. From that time instant on, the distance no longer increases and, hence, all the trajectories of the system in (3.59) are bounded.

Hence, with the three conditions being verified, it is proved that $\mathbf{x}_d$ is a globally asymptotically stable equilibrium for the system in (3.59), and thus also for system (3.58). This enhances the result from the

previous section, since a wider range of controllers (3.57) can now be applied, in order to achieve global stability of system (3.34).

3.6 Analysis of the control parameters

Summarizing the results obtained so far in this chapter, a new approach for the tracking control problem was proposed, with the introduction of a new variable δ. The usual line-of-sight tracking method was then redefined in order to avoid the singularity that arises when the constant speed constraint is added to this kind of tracking control problems. Based on the system dynamics derived from the proposed approach, a controller acting on the UAV heading rate was derived, and global stability was proved.

An additional analysis is here, made in order to find how the control parameters affect the performance of the system, allowing for reasonable convergence times while respecting the main restriction of the maximum UAV heading rate.

Recalling the proposed error formulation, a new variable δ was introduced, and a virtual vector $\boldsymbol{\delta}$ was defined aligned with the reference velocity vector. A relative vector **z** was defined as the sum of the direct line-of-sight vector **d** (distance) and the new vector $\boldsymbol{\delta}$. Moreover, parameter δ was defined as a function of the squared norm of the distance d, from (3.23), with the norm of vector $\boldsymbol{\delta}$ becoming

$$\delta = \varepsilon d^2 + R. \tag{3.66}$$

As seen before, in order to avoid a possible singularity, the norm of this vector should be always greater than distance d, and thus control parameters ε and R must be tuned accordingly, respecting condition (3.37).

The derived error formulation was then based on a reference frame fixed with the relative vector **z**, and new error variables were defined, ρ, ϕ_r and ϕ, expressing the relative positions and relative headings between the UAV and the reference point. The relative errors and the derived system state dynamics are then strongly driven by the dynamics of variable δ, since it affects directly vector **z**, and thus a proper selection of parameters ε and R should be made, having a crucial impact on the system dynamics.

Therefore, a particular analysis will be made, in order to understand how the given parameters affect the system dynamics, particularly the control input to be commanded to the UAV heading rate. The key point to be considered is the main restriction on the UAV maximum heading rate ω_{max}, and thus, the following analysis aims to find how the parameters ε and R can be used to guarantee that the control input never exceeds this limit, $\omega \leq \omega_{\text{max}}$.

The derived control law that ensures a global asymptotic stability is given by (3.57), and provides some freedom on the choice of function $h(\phi)$, as long as the stated conditions are complied with. In order to simplify the analysis, the simplest form of function $h(\phi)$ will be here considered as $h(\phi) = k\phi$, leading to the following controller:

$$\begin{aligned}\omega(t,\mathbf{x}) &= -k\phi + \omega_\rho(t,\mathbf{x}) \\ &= -k\phi + \frac{1}{\rho}\big(V_{\text{r}}\text{s}\phi_{\text{r}} - V_{\text{r}}\text{s}\phi + \delta\omega_r(t)\text{c}\phi_{\text{r}}\big) - 2\varepsilon V_{\text{r}}\text{s}\phi_{\text{r}}\left[\text{c}\phi - \text{c}\phi_{\text{r}} + \frac{\delta}{\rho}\big(1 - \text{c}\phi\phi_r\big)\right],\end{aligned} \tag{3.67}$$

where k is a positive control gain to be tuned.

The idea of this control approach, discussed in the previous two sections, is to use the feedback term $-k\phi$ to drive variable ϕ to zero, aligning the UAV heading with the relative vector direction χ_ρ, and to use the term ω_ρ so that the UAV can keep up with the heading variation of the relative vector **z**. With this control approach, we proved the global asymptotic stability of the system to the desired point, that corresponds to the UAV overlapping the reference point.

However, the previous analysis did not consider an upper bound on the control input, as it only guarantees that once the system reaches the desired point, it remains there as long as a feasible reference trajectory is given. Therefore, the maximum possible value of the control input ω should be limited so it can be attained by the UAV.

Considering the control law in (3.67), we note that only the first term can be directly regulated – through the tuning of the control gain k – and the remaining terms – corresponding to the rate of direction of the relative vector, ω_ρ – are a result of the system dynamics and cannot be controlled directly. Hence, the dynamics ω_ρ will be assessed, mainly in terms of how it is affected by parameters ε and R.

The relation expressed in (3.37) states a condition to avoid a singularity that could exist when $\rho = 0$. However, it does not avoid possible high values of ω_ρ that cannot be suported by the UAV, and thus a further condition should be found to set a bound on this value.

Evaluating parameter ε, some initial considerations can be made. For $\varepsilon = 0$, it is not possible to prove that the singularity $\rho = 0$ will not be reached, since it would be necessary to have $R = \infty$. In contrast, if a large value of ε is considered, the value of δ would also be large, and for large values of the initial distance d, the convergence time would be also significantly high. In the extreme case of $\delta \to \infty$, the system will behave as if the commanded heading rate to the UAV was the reference heading rate ω_r. Hence, parameter ε should be selected by considering a trade-off, where a sufficiently low value should be chosen to allow for an acceptable performance, although sufficiently large, to allow for feasible values of ω_ρ.

For the evaluation of parameter R, consider the case in which the UAV is overlapping the reference point, yet with different headings. In this case, the distance between the UAV and the reference point is zero, $d = 0$, and thus $\rho = \delta = R$ and $\phi \neq 0$, leading to $\dot{\delta} = -2\varepsilon V_\mathsf{r} \left[R\left(\cos\phi - 1\right) + R\left(1 - \cos\phi\right)\right] = 0$. Moreover, considering the worst case obtained at $\phi = -\pi/2$, leading to the highest value of ω_ρ, it follows that

$$\omega_\rho \left(d = 0, \phi = -\frac{\pi}{2}\right) = \frac{1}{R}\big(V_\mathsf{r} + R\omega_r(t)\big). \tag{3.68}$$

Hence, parameter R should respect the condition

$$R \geq \frac{V_\mathsf{r}}{\omega_\mathsf{max} - \omega_{r_\mathsf{max}}}, \tag{3.69}$$

where ω_max is the UAV maximum heading rate to be respected, and ω_{r_max} is the maximum value of the reference heading rate.

From this condition one can see that when $\omega_{r_\mathsf{max}} = \omega_\mathsf{max}$, parameter R and thus variable δ should be infinite so the relative heading rate ω_ρ does not exceed ω_max. Moreover, this result is only for the case in which the distance is zero, as for greater values of distance d it is not possible to guarantee a feasible dynamics of ω_ρ when the reference heading reaches the UAV maximum heading rate. Nevertheless, the worst-case for the UAV heading direction was considered, by setting $\phi = -\pi/2$. However, if one considers $\phi = 0$ additionally to $d = 0$, the system is in the desired point, and the relative heading rate ω_ρ will equal the reference ω_r. Hence, it follows that once the system is in the desired point, then it can remain there, even if the reference trajectory is in the boundary of the feasible heading rate for the UAV.

Considering the maximum value of variable ϕ_r given by (3.38), and the condition imposed to parameters ε and R in (3.37), it is straightforward to conclude that the absolute value of ϕ_r never exceeds $90\,\mathrm{deg}$, and thus $\cos\phi_r > 0$. Hence, from the expression of ω_ρ in (3.44), the larger the reference heading rate ω_r, the larger the relative heading rate ω_ρ. Accordingly, to find the maximum value of ω_ρ, the maximum value of ω_r should be considered.

Given the high complexity of the relative heading dynamics, in (3.44), and the cross relations between the state variables, it is not straightforward to find analytically a direct relation between the parameters ε and R and the maximum possible value of ω_ρ. Hence, an algorithm is used to test all the possible combinations between the state variables for a given value of w_r, and for each pair (ε, R), in order to give several combinations that can ensure the maximum value of ω_ρ never exceeds ω_max.

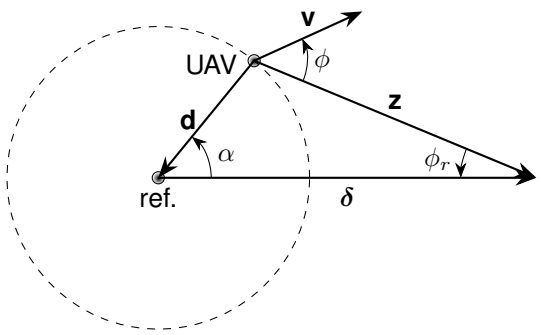

Figure 3.10: Relative motion geometry for the determination of all possible combinations between the state variables

Consider the geometry of the relative motion depicted in Figure 3.10. In order to test all the possible combinations of the state variables, the reference point and the reference velocity are fixed. Then, all the possible positions of the UAV can be represented by variables d and α, with $\alpha \in [-\pi, \pi]$. For each distance d there is a corresponding value of δ, and for each pair (d, α) there is a corresponding pair (ρ, ϕ_r). Then, for each position of the UAV – defined in relation to the reference point through the state variables δ, ρ and ϕ_r –, the direction of the UAV velocity vector is given by variable ϕ and range in $\phi \in [-\pi, \pi]$.

Hence, an algorithm is proposed here, which computes the maximum value of ω_ρ for all the possible values of the state variables, for a given pair (ε, R):

Algorithm 1 Determine the maximum value of ω_ρ

Require: (ε, R)
  $(\omega_\rho)_{\text{max}} = 0$
  for $d = 0$ to d_{max} **do**
    $\delta = \varepsilon d^2 + R$
    for $\alpha = -\pi$ to π **do**
      $\rho = \sqrt{d^2 + \delta^2 - 2d\delta\cos\alpha}$
      $\phi_r = \frac{\alpha}{|\alpha|}\arccos\left[\frac{\rho^2+\delta^2-d^2}{2\rho\delta}\right]$
      for $\phi = -\pi$ to π **do**
        $\omega_\rho = \frac{1}{\rho}\left(V_{\text{r}}\text{s}\phi_{\text{r}} - V_{\text{r}}\text{s}\phi + \delta\omega_r\text{c}\phi_{\text{r}}\right) - 2\varepsilon V_{\text{r}}\text{s}\phi_{\text{r}}\left[\text{c}\phi - \text{c}\phi_{\text{r}} + \frac{\delta}{\rho}\left(1 - \text{c}\phi\phi_r\right)\right]$
        if $\omega_\rho > (\omega_\rho)_{\text{max}}$ **then**
          $(\omega_\rho)_{\text{max}} = \omega_\rho$
        end if
      end for
    end for
  end for

Using the Algorithm 1, we would like to find the required value of ε, needed to ensure $\omega_\rho < \omega_{\text{max}}$ for every possible system configuration when the minimum value of parameter R is chosen from (3.69). The results obtained with this implementation are depicted in Table 3.1, considering $\omega_{\text{max}} = 1\ [rad/s]$.

Table 3.1: Control parameters (ε, R) for different values of ω_r. The minimum value of R is computed for each ω_r, and the corresponding value of ε is found to ensure $\omega_\rho \leq \omega_{\text{max}}$ always holds. Here we consider the maximum UAV heading rate $\omega_{\text{max}} = 1\ [rad/s]$.

$(\omega_r)_{\text{max}}\ [rad/s]$	0	0.1	0.2	0.3	0.4	0.5	0.6	0.7	0.8	0.9	1
$R_{\text{min}}\ [m]$	30	33.3	37.5	42.9	50	60	75	100	150	300	–
$\varepsilon\ [m^{-1}]$	1.6	1.6	1.6	1.7	1.8	1.8	2.0	2.0	2.1	2.2	–

From the results depicted in Table 3.1 we can observe that the minimum required value of R increases as the reference heading rate ω_r increases, as expected, to ensure that the UAV maximum heading rate is respected whenever the distance d is zero. For higher value of the distance between the UAV and the reference point, the condition $\omega_\rho \leq \omega_{\text{max}}$ is assured for every possible system configuration, using the corresponding value of ε. However, the needed values of ε lead to high values of vector $\boldsymbol{\delta}$ and thus lead to high convergence times, as it will be shown in the simulations of next chapter. Hence, we present in Table (3.2) the results after the implementation of Algorithm 1, where the minimum required values of R are found for each value of ω_r, considering several possible values of ε, smaller than the ones obtained in Table 3.1.

Table 3.2: Values of R needed to complete the pair (ε, R), for different values of ε, ensuring the compliance with $\omega_\rho \leq \omega_{\text{max}}$ for different values ω_r. The maximum UAV heading rate considered is $\omega_{\text{max}} = 1\ [rad/s]$.

$\varepsilon \backslash \omega_r$	0.3	0.4	0.5	0.6	0.7
0.006	129	167	228	–	–
0.007	117	150	204	–	–
0.008	107	138	186	–	–
0.009	100	128	172	–	–
0.01	95	121	162	233	380
0.02	69	86	112	155	242
0.03	61	74	95	129	197
0.04	56	69	87	116	173
0.05	54	65	82	108	159
0.06	52	63	78	103	150
0.07	51	61	76	99	143
0.08	50	60	74	96	138
0.09	49	59	72	94	134
0.10	49	58	71	92	131
1	44	51	62	77	103

With the results summarized in Table (3.2), several pairs of the control parameters (ε, R) are provided, to ensure the compliance of the resulting control input with the UAV maximum heading rate. The required value of R increases as the chosen value of ε decreases, and thus a trade-off should be made between both parameters. For relatively high values of ε (nearly $\varepsilon > 1$) small values of R are needed, although the convergence time may be excessively high. In contrast, as the considered ε decreases, the required R increases, leading to high convergence times for smaller distances. Still, these results are still quite abstract, and the impact of the pair (ε, R) in the system performance will be better understood in the simulations of the following chapter. A simulation analysis is held in Appendix B in order to understand the effect of each single state variable on the resulting maximum value of ω_ρ.

3.7 Summary

The main objective of this chapter was to address the tracking control problem for constant speed vehicles with nonholonomic constraints. The key challenge that arises in this kind of control problems is that the pursuer vehicle to be controlled is strongly underactuated, as the speed is set to constant, and the only available actuation is on the commanded heading rate. Hence, such a restricted system is likely to have a singularity when the most typical line-of-sight formulation is considered, as the relative vector between the pursuer vehicle and the reference point is not fully defined when both are coincident, leading also to a peak in the control input when both vehicles approach with opposite directions.

Therefore, in order to circumvent the singularity problem, a novel error formulation was proposed to represent the tracking control system, with the introduction of a new variable δ. A new vector with norm δ is placed in the reference point, aligned with its heading direction, and a relative vector is defined as the sum of both the direct line-of-sight vector (distance between the pursuer and the reference point) and the new vector $\boldsymbol{\delta}$. The norm of the new relative vector is represented by ρ, and, in addition to the norm δ, are both considered as state variables. Additionally, two other state variables are considered, ϕ_r and ϕ, representing the angle between the relative vector direction and the reference and pursuer headings, respectively. The full state vector is then composed of four state variables, one more than the usual error formulation in the literature, given the introduction of the new variable δ, which is the responsible for the elimination of the singularity.

Some steps of the intermediate process to achieve the final proposal for the error formulation are shortly described during this chapter, and the more relevant one is an intuitive definition of variable δ,

inversely proportional to the tracking distance error. This intermediate solution is intuitive as it would imply a very small δ for large distance errors, becoming equivalent to the direct line-of-sight solution, and then, for distance errors near zero, the value of δ would increase, and the relative heading would be the reference heading, avoiding thus the singularity in the desired point. However, it would not be possible to avoid the singularity on the whole state space, as the value of ρ could approach zero at some point, for some configuration of the involved variables. Hence, the proposed solution for the error formulation is able to avoid the singularity for the whole state space, as long as the control parameters ε and R are set such that the value of δ is greater than the distance so that ρ – the norm of the relative vector – never approaches zero.

After the development of the new error formulation globally valid for the given tracking control problem, ensuring the absence of any singularity, the goal was to design a control law to command the pursuer heading rate to the desired reference point/trajectory. The control law should ensure a global asymptotic stability of the controlled system, being able to steer the pursuer vehicle to the reference point in finite time, from any initial condition, or any possible configuration of the state variables. Given the nonlinearity of the problem, typical methods to assess the stability of nonlinear systems were applied, relying on Lyapunov's stability theory. This theory is based on generalized "energy-like" scalar functions that depend on the system state, and on a fundamental physical principle: *if the total energy of a physical system is continuously dissipated, then it must eventually settle to an equilibrium point*.

Firstly, a controller was derived through the definition of a Lyapunov function for the whole system, and asymptotic stability was proved from its negative semidefinite derivative and using Lyapunov's direct method, complemented with *LaSalle's Invariance Principle* and *Barbalat's Lemma*. However, this controller does not ensure global stability, as it is not defined in $\phi = \pi$ rad. Hence, further analysis was made, and from a particular result that ensured asymptotic stability whenever the condition of $\phi = 0$ rad was verified, a more generalized stability proof method was employed, through the analysis of the system as a nonlinear cascade system. This method ensures a global asymptotic stability of the overall system, as long as a controller is able to lead variable ϕ to zero, as the unforced system with $\phi = 0$ rad is proved to be asymptotically stable from the previous Lyapunov function. Therefore, a control law was obtained, whose dominant term is due to the relative error formulation, and is the rate of direction of the relative vector, ω_ρ. From the controller perspective there is no direct control on this term, as it is mainly dependent on the value of δ.

Hence, given the proposed definition of variable δ, the ω_ρ term and thus the controller behavior is mainly regulated by control parameters ε and R, which should be tuned so that the resulting control command can be limited, satisfying the pursuer maximum heading rate. However, given the complexity of the system dynamics, involving highly nonlinear cross-relations between the state variables, the analysis of parameters ε and R and its effect on the system evolution becomes non-trivial to quantify. Hence, given this challenging problem, an algorithm was implemented to compute the maximum achievable value of ω_ρ, for each pair of parameters (ε, R) and given the known maximum value of ω_r, a list was presented, with several pairs (ε, R) which ensure that the value of ω_ρ never exceeds the pursuer maximum heading rate. Therefore, parameters ε and R, responsible for the δ formulation, have an extreme importance on the tracking control problem, not only to guarantee the avoidance of the singularity but also to ensure a fair compromise between performance and enforcing the limits of actuation of the controlled system. A more detailed analysis of the influence of both parameters in the resulting system dynamics will be assessed in the following chapter.

Chapter 4

Simulations and Results

This chapter is devoted to the implementation and analysis of the Guidance and Control system, resulting from the combination of the separated sub-systems developed in the previous two chapters. Several simulations will be presented in order to consolidate the theoretical results of the previous chapters, in order to demonstrate the key features of the proposed solution. A discussion of the results achieved through the chapter will be held in the last section, as well as an overview of the limitations of the considered assumptions and the designed system.

Firstly, a simulation is presented of the guidance system, where a reference trajectory is generated, following a vessel with a variable speed profile. Secondly, a thorough series of simulations is carried out to evaluate the convergence rate and control effort of the Control system, with a circular trajectory as input. Here several aspects of the control system will be assessed, such as the effectiveness of the proposed δ-control approach, the adjustment of the control parameters ε and R to enforce the actuation bounds while optimizing its performance, and also the tuning of the control gain k_1. The introduction of different perturbations on the system will be also assessed, particularly an error on the UAV speed, that can arise from faulty sensor measurements, or from a weakness on the inner-loop controller accountable for the reference speed tracking, and also a constant wind perturbation. Finally, the overall system is implemented, and the oscillatory trajectory from the guidance is given to the control system, assessing the main problem of the UAV tracking to the vessel smoke plume, given the stated mission restrictions. The architecture of the overall system is depicted in Figure 4.1:

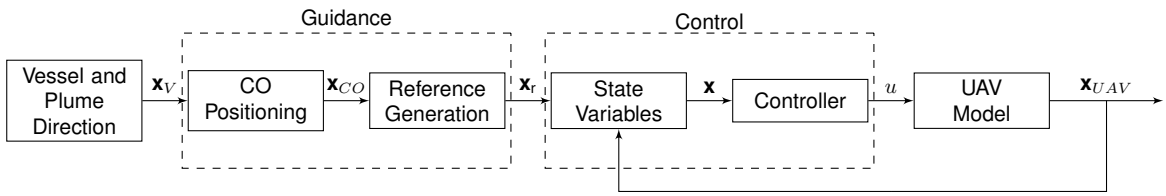

Figure 4.1: Guidance and Control Architecture

From the given motion of the vessel, namely its position, orientation and both the linear and angular velocities, the Guidance system is responsible for the generation of a reference trajectory, which represents the desired configuration of the UAV at every instant. The generated reference is the input to the Control system, as well as the UAV configuration. At this point the relative motion between the UAV and the reference point is converted in the state variables $\left[\delta, \rho, \phi_r, \phi\right]$ and the designed control law is computed and applied to the UAV heading rate, so it can converge to the reference trajectory. Consider the constant parameters of Table 4.1, applicable for all the simulations performed in this chapter:

Table 4.1: Constant parameters to be applied in all simulations

Reference speed	$V_\mathrm{r} = 30$ m/s
UAV maximum heading rate	$\omega_\mathrm{max} = 1$ rad/s
Keep-out area radius	$r_\mathrm{min} = 200$ m
Smoke plume heading	$\chi_P = 180\ \mathrm{deg}$

4.1 Guidance Results

The guidance system developed in Chapter 2 is here implemented, and a simulation is carried out to observe the behaviour of the reference trajectory motion (2.7), mainly the oscillatory heading rate solution, and the way parameter η is able to shape the trajectory to keep track with the vessel, even when variations of the vessel speed occurs.

The evolution of the vessel speed is represented in Figure 4.2 and is a typical speed profile for a marine vessel [75], considering soft accelerations. The vessel is initially stationary, then accelerates with a sinusoidal speed profile until reaching the speed ratio of $\nu = 0.8$, and then slows down to a speed ratio of $\nu = 0.5$, which holds until the end of the simulation.

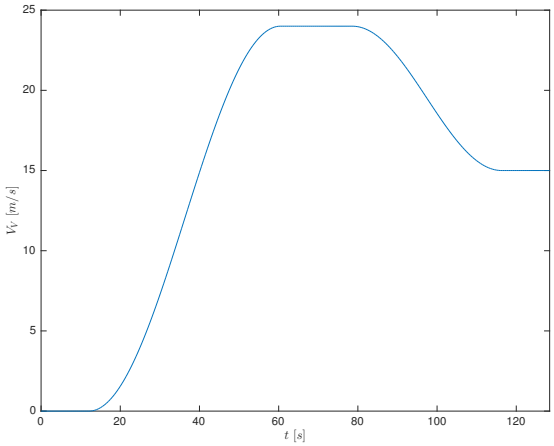

Figure 4.2: Vessel speed profile for the guidance system simulation

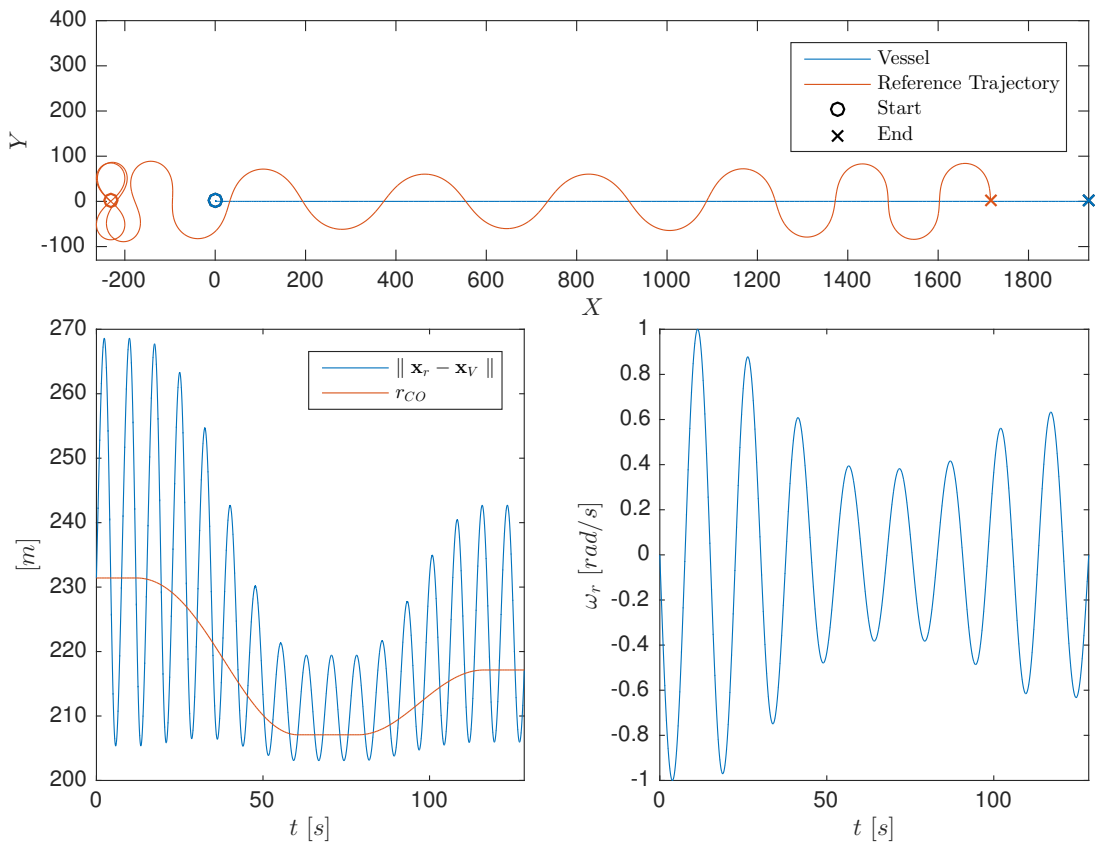

Figure 4.3: Simulation of the guidance system performance, generating a reference trajectory to follow a vessel with the speed profile of Figure 4.2

The results of the simulation of the guidance system, considering a vessel with the speed profile of Figure 4.2 are summarized in Figure 4.3. The upper figure depicts the trajectories of both the vessel and the reference point during the simulation. It is clear there is a constant reshaping of the reference trajectory along the vessel speed direction, keeping track with the vessel motion. This behavior is due to the parameter η, which depends on the speed ratio ν. On the bottom left figure, the distance between the vessel and the reference point is depicted, as well as the radius of the CO over time. The CO positioning was computed with the second method presented in section 2.6 and one can see that as the vessel speed increases, the radius of the CO decreases, maintaining the minimum distance between the reference and the vessel approximately constant, near the keep-out area ($r_{\text{min}} = 200\ m$). The smoke plume measurements should be performed in the points where the reference trajectory crosses the CO, that is in the smoke plume direction, and thus, with the presented solution, the gas measurements can be held with a periodicity of less than $\Delta t = 8\ s$, occurring twice every oscillation period, at a distance to the vessel that can range from about 207 m to 230 m, depending on the vessel speed. If the gas measurements need to be performed closer to the vessel, then the optimized CO positioning method introduced in Section 2.6 can be used. However, it would lead to a doubling of the period between consecutive measurements. The bottom right figure displays the reference heading rate throughout the simulation, and it is clear that it never exceeds the UAV maximum heading rate, and thus it is a feasible reference trajectory.

4.2 Control Results

In this section, the designed controller is implemented, and several simulations are presented to assess the performance of the proposed solution for the tracking control problem. The control system receives as input both the reference and the UAV position and heading, as well as the reference speed and heading rate. Internally, the controller transforms the relative configurations in the state variables introduced in Chapter 3: δ, ρ and ϕ_r to represent the relative position, and ϕ for the UAV relative heading. The output control command is computed from these state variables and provides the UAV with the appropriate heading rate in order to track the reference point. With the proper selection of the control parameters ε and R, the UAV will converge to the reference trajectory, as ensured by the global asymptotic stability result in the control design, while respecting always its maximum heading rate.

4.2.1 Particular case: circular reference trajectory – control of the steady-state distance error

First of all, and before the analysis of the results obtained with the proposed δ-control approach, the particular application of the direct line-of-sight control method that was introduced in Section 3.3.1.2 will be here validated. In that subsection, the particular problem of tracking a circular reference trajectory using a basic proportional controller was assessed.

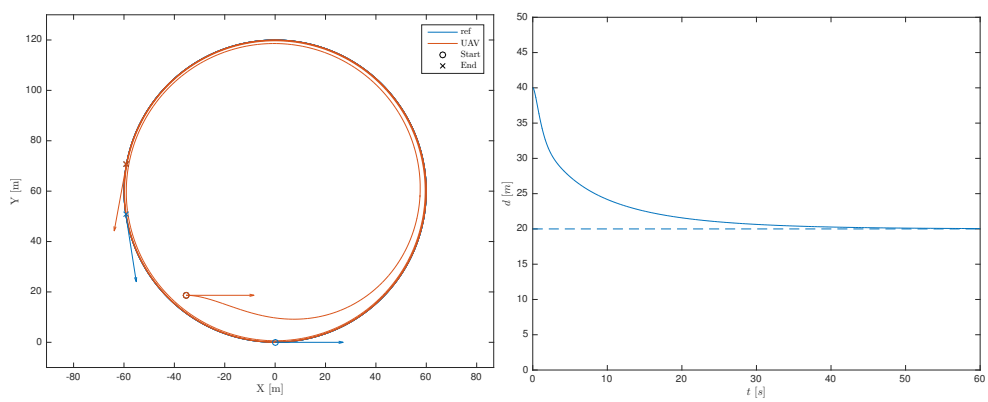

Figure 4.4: Implementation of the proportional controller to the line-of-sight approach, leading the steady-state error distance to $d^*_{ss} = 20$ m

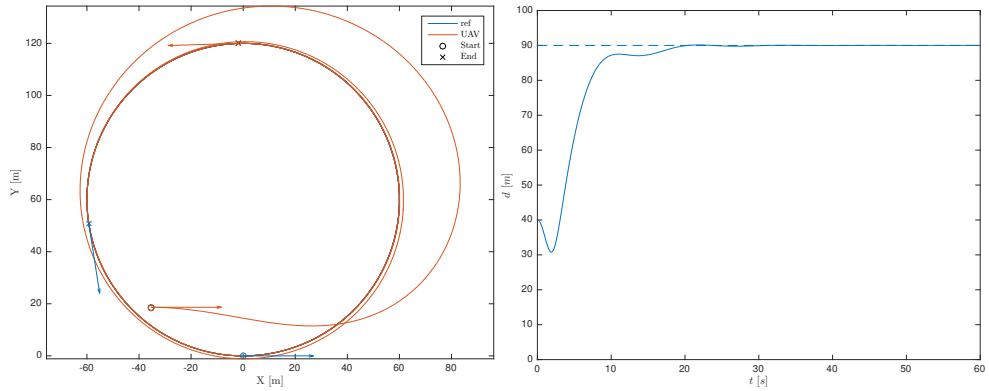

Figure 4.5: Implementation of the proportional controller to the line-of-sight approach, leading the steady-state error distance to $d^*_{ss} = 90$ m

An equilibrium point was found geometrically, and it was proved to be an asymptotically stable equilibrium of the system (3.12), using the *Lyapunov's indirect method*. However, the equilibrium point was not at the desired point, i.e. $d = 0$. Instead, the controlled system with the proportional controller converges to a constant steady-state error distance. The interesting feature that was found was that this steady-state distance can be regulated to a desired value d^*, through the proper choice of the control gain k, by using (3.20).

Hence, in order to validate the achieved result, the proportional controller was implemented and two simulations are depicted in Figures 4.4 and 4.5, where the control gain k was tuned to lead the steady-state distance to $d^* = 20$ m and $d^* = 90$ m, respectively.

4.2.2 Results supporting the adaptive δ-control approach

As discussed in Subsection 3.3.2, the direct line-of-sight approach for the tracking control problem has a critical issue, as it has a singularity exactly at the desired point. When the UAV is above the reference point, the relative heading on the direct line-of-sight control approach becomes ill-defined. Moreover, near this singularity, if the UAV approaches the reference point with opposite direction, the resulting control input may reach excessively high values and leading to the saturation of the UAV actuators. This saturation poses a great challenge on the derivation of a globally asymptotically stable control law, and it would be only possible if the UAV speed was also controllable, as it is considered in the existing works on the tracking control problem for nonholonomic vehicles, as referred in Section 3.2.

Hence, as a constant speed UAV is considered in this dissertation, the existing solutions for the tracking control problem with nonholonomic vehicles cannot be applied, and a δ-control approach was introduced. Even if one could control the speed of the UAV, it would be within a certain interval of admissible values, which violates the assumption in the literature of being able to vary the speed to arbitrarily low or high values. The direct line-of-sight between the UAV and the reference point was redefined, and the new line-of-sight was set as the relative vector connecting the UAV and the tip of vector $\boldsymbol{\delta}$. With this new approach, for a positive nonzero δ, the zero-error point is no longer a singularity, as the relative line-of-sight vector is well-defined when the UAV is above the reference point.

Simulation results are presented in Figure 4.6, where the δ-control approach is applied, considering a constant δ. Three different initial configurations of the UAV where simulated, all of them with the UAV heading pointing towards the tip of vector $\boldsymbol{\delta}$, and thus $\phi = 0$. Hence, the system behaves with the dynamics of the unforced system (3.60). The error distance evolution, in the upper right figure, confirms that the distance never increases when $\phi = 0$, as given by the semidefiniteness of the Lyapunov function derivative (3.62). However, a system with a constant δ can still reach a singularity, if the UAV approaches the tip of vector $\boldsymbol{\delta}$, and the effect of the singularity is noted in the example of UAV (3). In this particular example, the system approaches this singularity, with $\rho \to 0$, leading to a peak in the control input ω, due to the extreme variation in the relative heading χ_ρ.

However, if the relative angle ϕ is considered to be always null, and thus the error distance being always nonincreasing, it is straightforward to find a set of initial conditions that ensure the system never reaches the singularity. From the definition $\boldsymbol{\delta} = \mathbf{d} + \mathbf{z}$, if δ is always greater than the distance d, then $\rho = \|\mathbf{z}\|$ is always nonzero, and the singularity is not reachable. Hence, we conclude that the system never reaches the singularity, for any initial configuration respecting $\phi = 0$ and $d(t = 0) < \delta$.

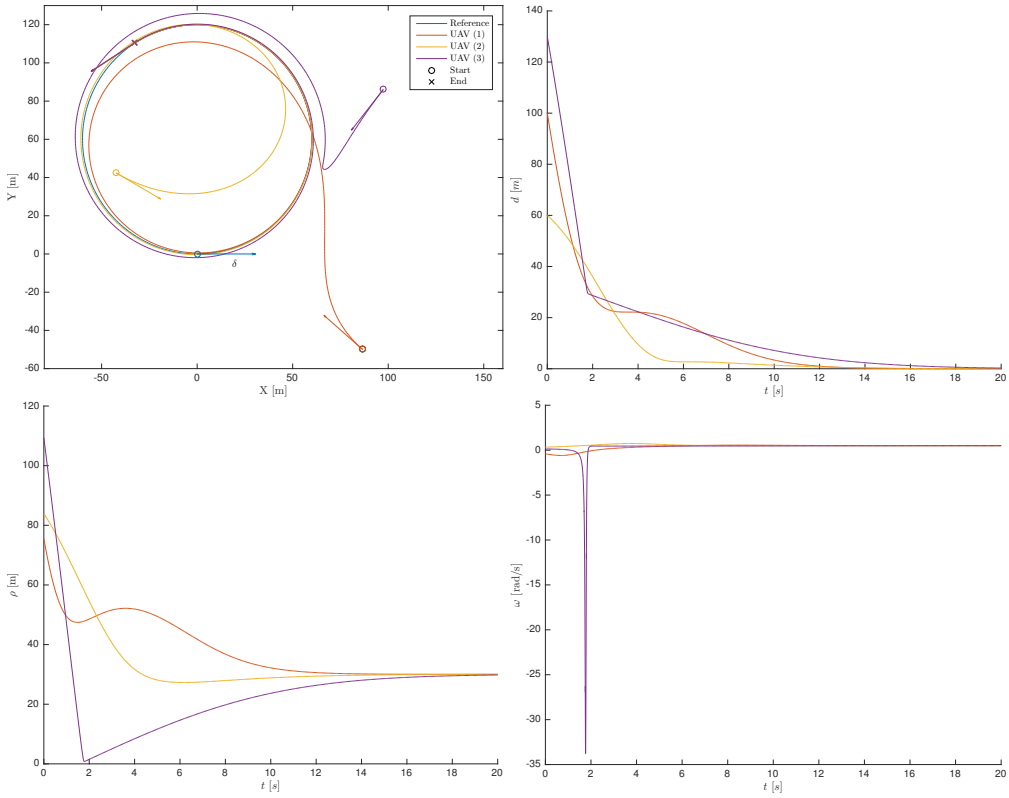

Figure 4.6: Tracking of a circular reference trajectory for different initial configurations. A constant δ is considered, and the relative angle ϕ is always null.

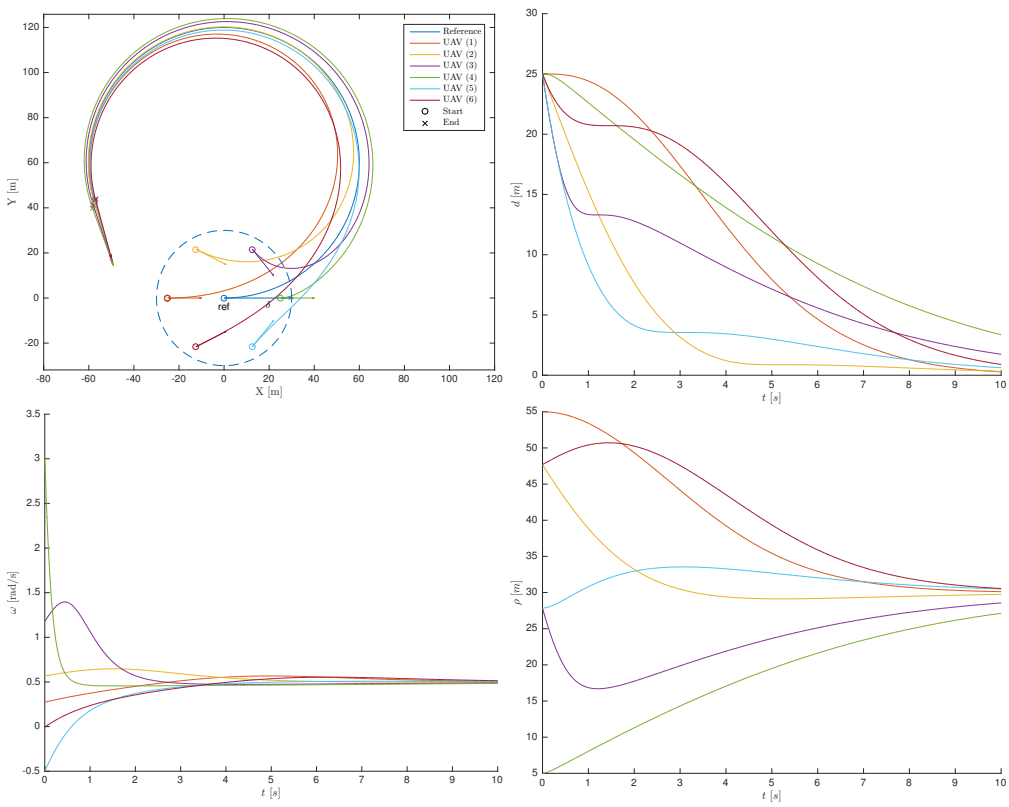

Figure 4.7: Tracking of a circular reference trajectory for a restricted set of initial configurations. A constant δ is considered with $\delta > d(t = 0)$, and the relative angle ϕ is always null.

It is presented in Figure 4.7 a simulation for a restricted set of initial UAV configurations. As for the given controller and in the ideal case of no disturbances or noise it is true that $\phi(t=0)=0 \Rightarrow \phi(t)=0$, then the distance d is always nonincreasing over time. Additionally, the condition for the initial distance $d(t=0)<\delta$ ensures that the system never reaches the singularity, as can be derived from the bottom right figure in 4.7, where ρ never gets close to zero.

Therefore, the previous reasoning can be extended for any initial distance between the UAV and the reference point, as long as the value of δ is chosen so that $\delta > d(t=0)$. However, even if the system never reaches the singularity, it can still lead to the saturation of the control input, as happens in examples 3 and 4 of the results in Figure 4.7, where ω exceeds $\omega_{\text{max}} = 1$ rad/s, and, thus, the condition $\delta > d(t=0)$ is still not enough to guarantee the the enforcement of the actuation bounds of this control approach. One can also infer from the simulation in Figure 4.7 that the ratio between δ and d may have an impact on the resulting control input bound.

In Figure 4.8 a couple of simulations with similar initial configurations are presented, differing only on the value of δ. While in Figure 4.8a a large value of $\delta = 5000$ m was considered, in the second Figure 4.8b a smaller value, $\delta = 200$ m, was used. Here one can see clearly the effect of the value of δ in the resulting control input. On the one hand, large values of δ lead to small oscillations of the control input around the reference heading rate, resulting in a slow convergence of the UAV to the reference trajectory. On the other hand, smaller values of δ enable a faster convergence, yet requiring more effort on the control command. Therefore, a trade-off must be made on the choice of the value of δ, being sufficiently small to enable a good performance, i.e. having small convergence times, while sufficiently large so that the actuators does not saturate.

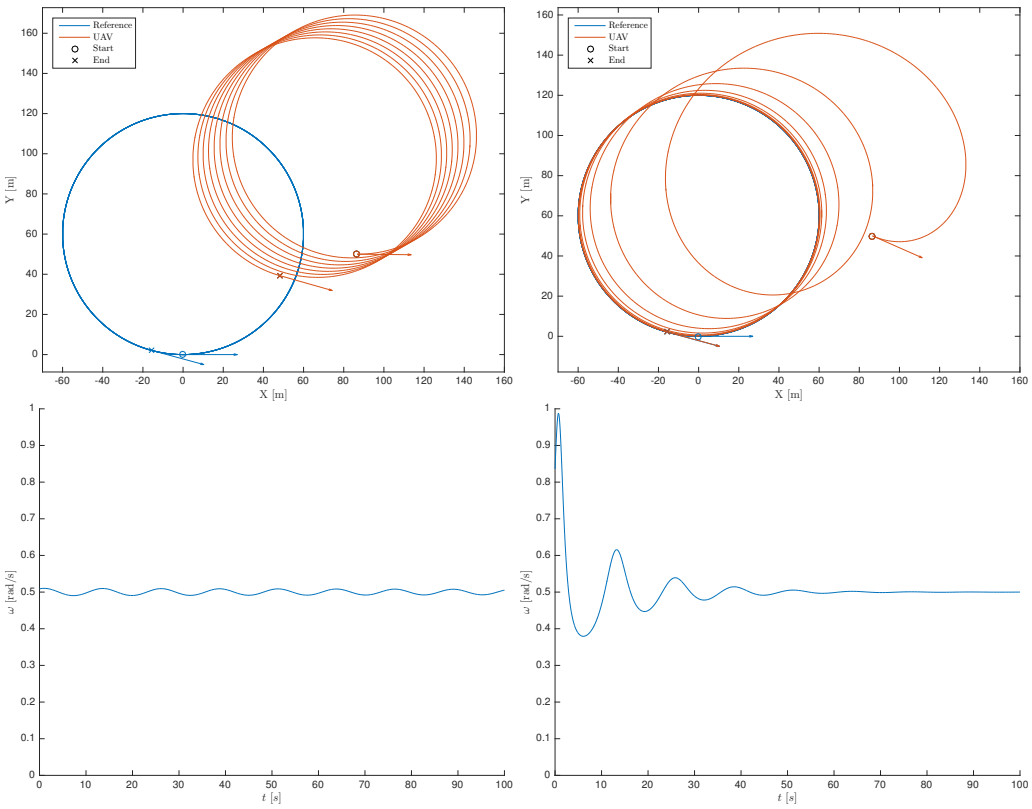

(a) $\delta = 5000$ m (b) $\delta = 200$ m

Figure 4.8: Tracking of a circular reference trajectory for similar initial configurations. Initial distance of $d = 100$ m and $\phi = 0$ rad.

A constant δ, however, does not seem to be an efficient solution, since for large initial distances it would be needed a large value of δ, leading to the deterioration of the control performance. Moreover, all the previous simulations considered a null value of ϕ, and in those cases the initial distance was the maximum distance of the entire simulation. However, if higher values of ϕ are considered for the initial condition, it is not clear how to estimate the maximum distance achieved during the simulation, even knowing it is bounded. Therefore, it is not possible to choose a constant value of δ to ensure the control

input never saturates, based only on the initial distance.

We now consider the proposed solution of using an adaptive δ, defined in (3.23), which increases with the squared norm of the distance in addition to a bias that ensures a nonzero value of δ at $d = 0$. The squared norm of the distance is chosen instead of simply the norm, as its derivative is well defined, in particular at the desired point, where the derivative of the norm of δ is not defined. A simulation is presented in the Figure 4.9, where the adaptive δ from the formulation in (3.23) is implemented. The improvement on the tracking control performance is evident, particularly when comparing the results of this simulation with the one in Figure 4.8b, where the same initial condition was considered, and a constant $\delta = 200$ m is applied. With the proposed approach, the value of δ in the beginning of the simulation is also close to 200 m, although this value decreases with the distance. This leads to a significant improvement on the convergence time, while the control input is still within the feasible bounds for the UAV heading rate, which was possible to attain through an appropriate choice of parameters ε and R.

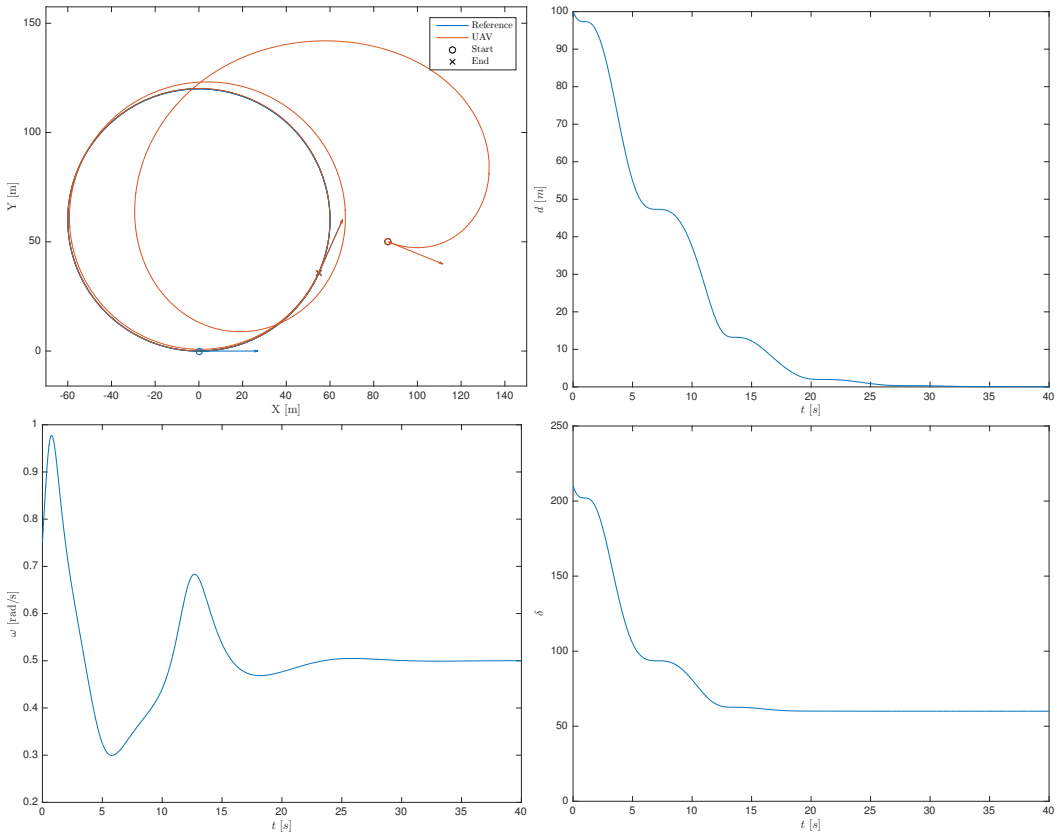

Figure 4.9: Tracking of a circular reference trajectory with the proposed adaptive δ-control approach.

Next, a simulation result is presented in Figure 4.10, to compare the behavior of the proposed δ-control approach in a situation where the direct line-of-sight control would saturate. In this simulation an extreme scenario is posed, with the UAV starting in front of the reference point, moving in the opposite direction. The simulation with the basic line-of-sight approach (left subfigure) converges almost instantaneously to the reference trajectory when it gets close to it. However, the resulting control signal exceeds the UAV maximum heading rate, leading to the saturation of the control input. On the other side, the simulation with the proposed δ approach is able to lead the UAV to converge to the reference point with a feasible control signal, and having a fairly acceptable performance, with a relatively fast convergence.

The resulting control command of the simulation with the δ approach is depicted in the bottom right Figure 4.10. The dashed line stands for the variation of the relative angle χ_ρ, which is a critical parameter to be considered, as it appears directly in the control law, and should not exceed the maximum heading rate of the UAV. In the same figure, the difference between the solid and the dashed line is due to the term of the control law $-h(\phi)$, defined in (3.57), which should be inversely proportional to the relative angle ϕ, and is the term responsible to lead this angle to zero. Intuitively, when the solid line overlaps the dashed line, it means that $\phi = 0$ and the distance no longer increases, as the system begins to behave as the unforced system (3.60).

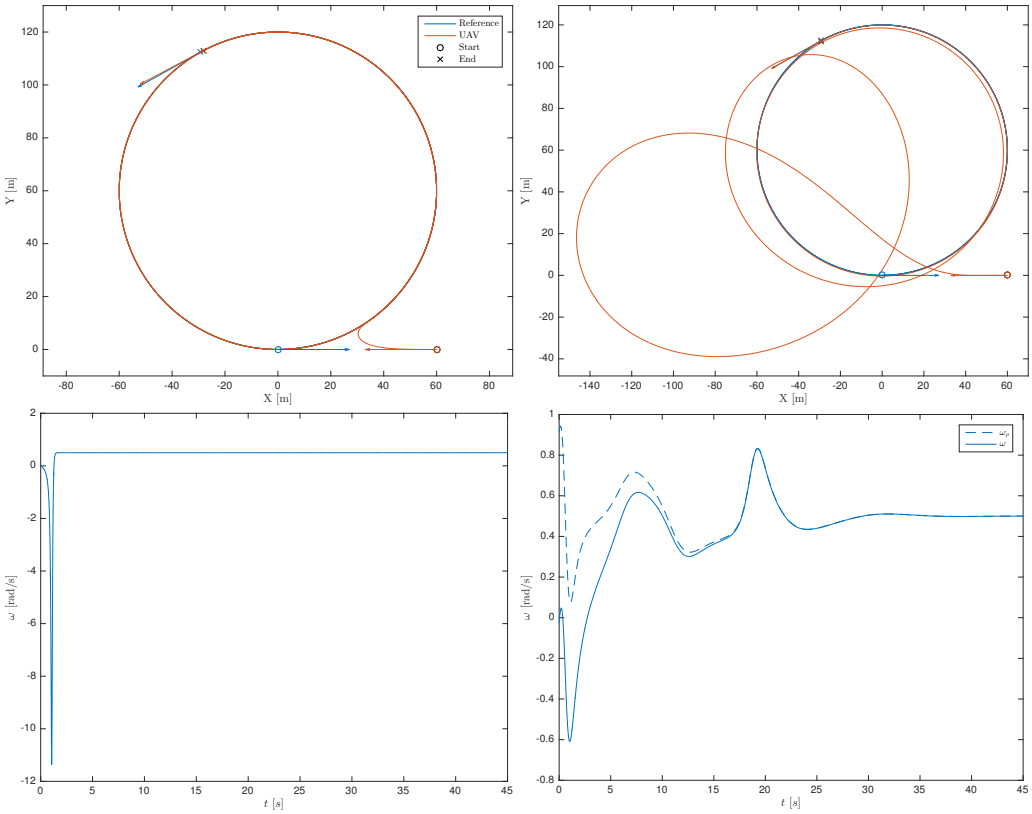

(a) Direct line-of-sight control

(b) Proposed adaptive δ-control approach

Figure 4.10: Comparison of the proposed δ-control approach with the direct line-of-sight control

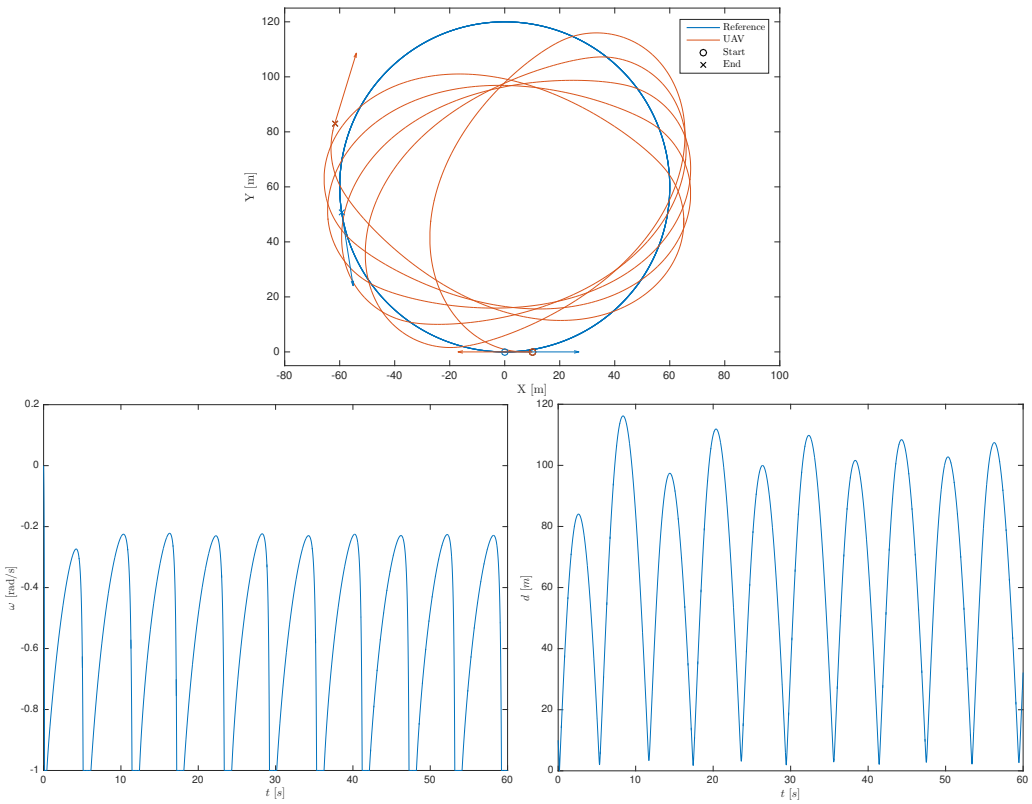

Figure 4.11: Extreme scenario leading to the saturation of the direct line-of-sight controller

One have already referred a few times that the direct line-of-sight control may reach excessively large values and saturate the UAV actuators, which should be always avoided, as it compromises the stability proof. Considering the controller derived in (3.57), which leads to the global asymptotic stability of the system, if the term ω_ρ exceeds the UAV maximum heading rate one can not guarantee that the system will converge to the desired point. With the proposed adaptive δ approach, the term ω_ρ can be indirectly regulated using control parameters ε and R. However, in the direct line-of-sight control, this term ω_ρ can ground unbounded near the singularity, leading to the saturation of the control input, and the stability proof does not hold. In Figure 4.11 simulation results are presented, with the direct line-of-sight control in an extreme scenario that leads to the saturation of the control input. Here the UAV heading rate is actually saturated, and one can see that in this particular case the system enters a limit cycle, thus not being able to converge to the desired point. This is a particular example to show that the saturation of the control input and the consequent loss of the stability proof validity lead to an unpredictable behavior of the system, and thus it should be strongly avoided.

In Subsection 3.3.2, a discussion was conducted in order to achieve the chosen formulation for the adaptive δ. One of the stated possibilities was that of an adaptive δ inversely proportional to the distance, d, that appeared to be an intuitive solution. Simulation results are presented in Figure 4.12, comparing both approaches, the one where δ is inversely proportional to the distance, $\delta \propto 1/d^2$ (left side), and the proposed solution with $\delta \propto d^2$ (right side). It is clear that the intuitive approach with $\delta \propto 1/d^2$ has better performance than the other solution for a great value of the initial distance. With the value of δ being roughly zero for large distances, the UAV heading points directly to the reference point in the simulation of the left figure, leading to a faster convergence. On the other side, as the value of δ is even greater than the distance d, the UAV will be nearly aligned with the reference heading, taking much longer to converge to the reference position.

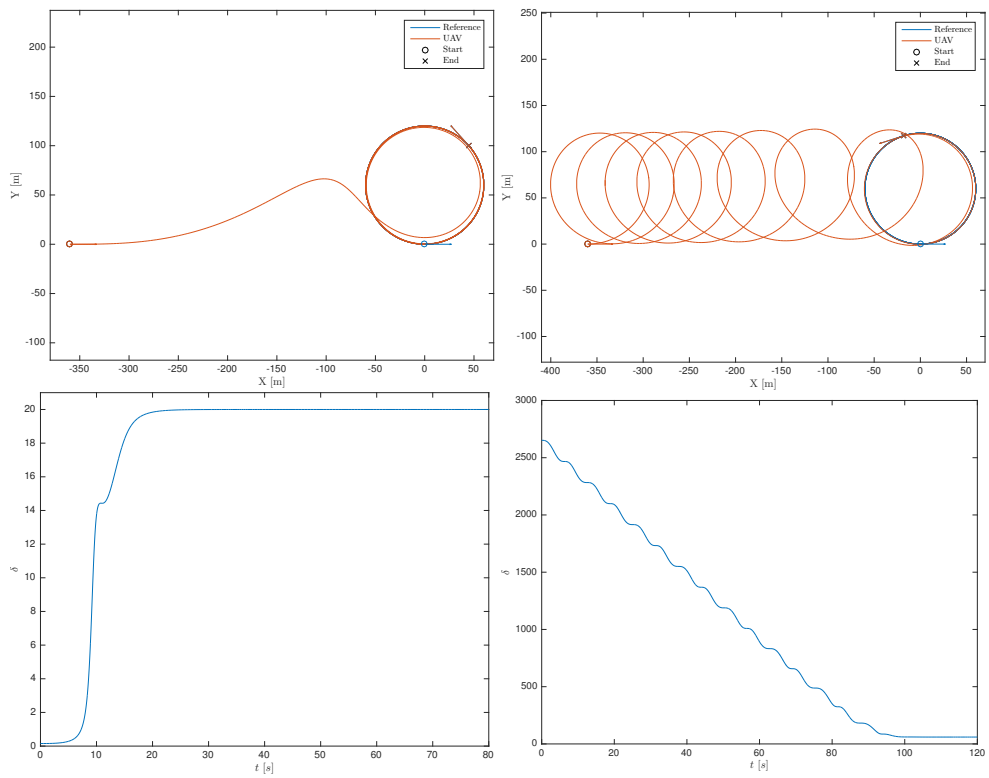

(a) $\delta \propto 1/d^2$ (b) $\delta \propto d^2$

Figure 4.12: Comparison between the different approaches for the variable δ, with a large initial distance

However, despite having better performance for large values of the distance, the intuitive solution with $\delta \propto 1/d^2$ is not able to avoid the singularity, and the same problem as for a constant δ arises. In Figure 4.13, a particular case is illustrated, in which the system with the intuitive δ solution approaches the singularity, leading to the saturation of the actuators, as can happen for the direct line-of-sight approach, or for the constant δ.

Hence, the solution that seems to be more intuitive at first does not solve the singularity problem, and thus cannot ensure global asymptotic stability. Concerning the chosen solution with $\delta \propto d^2$, despite leading to slower convergence times for larger distances, this is the one which guarantees the feasibility of the control effort, and the control parameters ε and R should be tuned in order to enhance the performance. The analysis of these control parameters will be assessed in the following section.

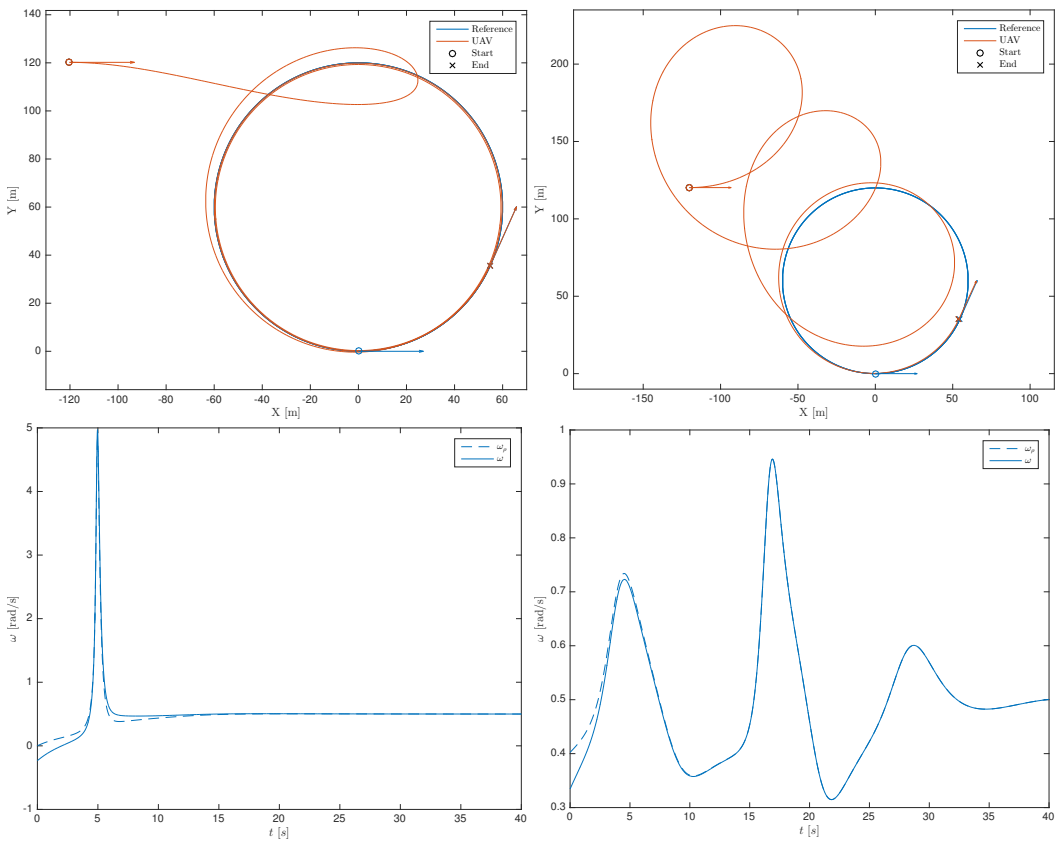

(a) $\delta \propto 1/d^2$ (b) $\delta \propto d^2$

Figure 4.13: Comparison between the different approaches for the variable δ, where the singularity is approached with one of the solutions

4.2.3 Variation of the control parameters

This section provides an analysis of the control parameters that are available in the proposed δ-control approach. The nominal controller that will be implemented here is the simplest one, given by (3.67). Hence, there is the control gain k to be tuned, as well as the control parameters ε and R which are able to indirectly affect the control law, by shaping the value of δ and thus affecting all the relative state variables and the system dynamics.

4.2.3.1 Control gain k

Firstly, the effect of the control gain k on the overall system performance is assessed. In Figure 4.14, different values of the control gain are applied for the same initial conditions. This results indicate how the control gain affects the convergence of the system to the desired point. A very small value of gain k, e.g. $k = 0.01$, leads to a very slow convergence, while a higher value enables a faster convergence, although possibly leading to the saturation of the actuators, as happens in the simulation with $k = 0.8$.

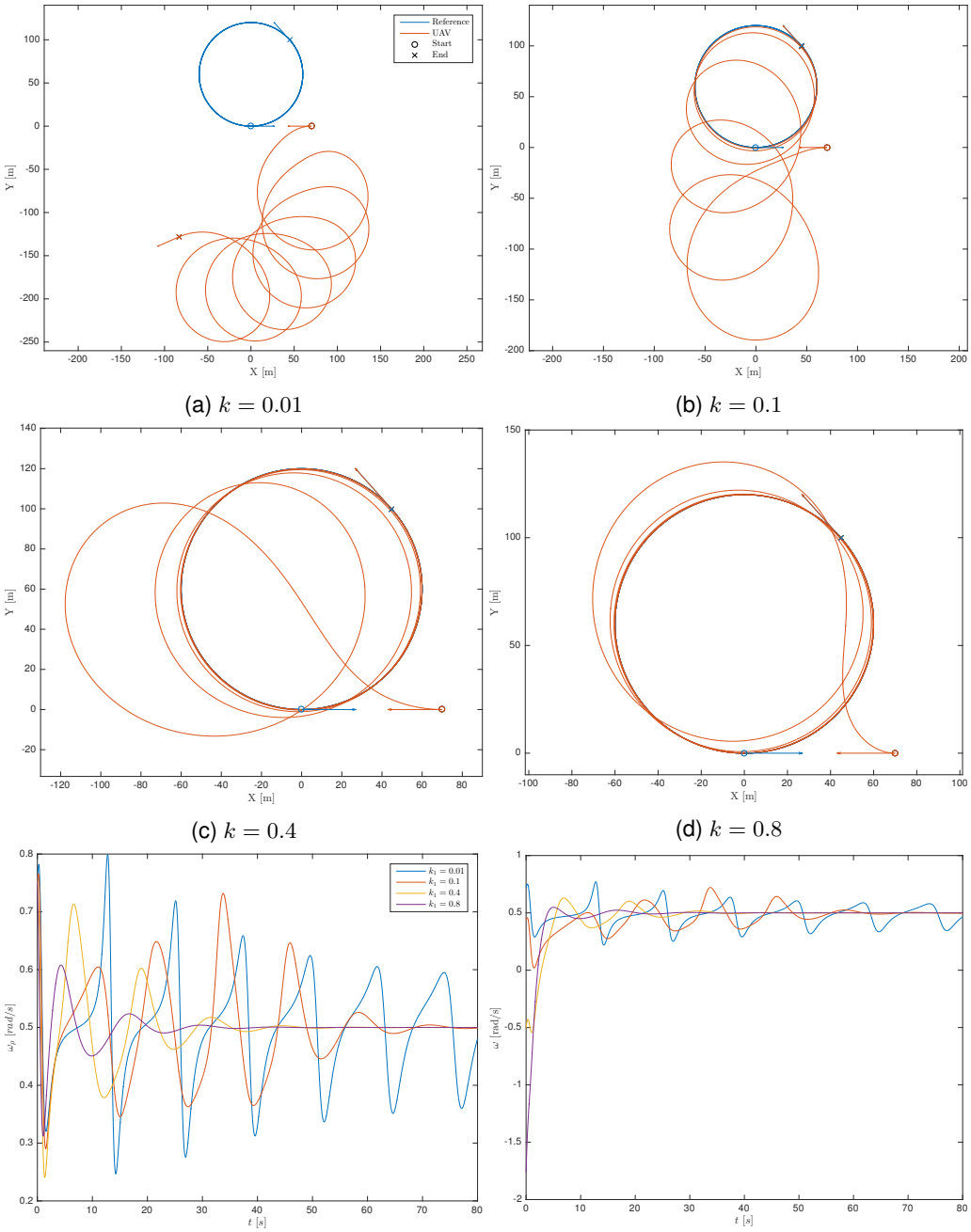

(a) $k = 0.01$ (b) $k = 0.1$

(c) $k = 0.4$ (d) $k = 0.8$

(e) ω_ρ (f) ω

Figure 4.14: Variation of the control gain k, and its impact on the tracking control performance

The effect of gain k is directly related to the result of the previous chapter where the system was analysed as a nonlinear cascade system. The convergence to the equilibrium point is only guaranteed when ϕ is zero – although, from the Lyapunov function, the condition of $\phi < \phi_\mathrm{r}$ is sufficient –, that corresponds to the condition in which the system behaves as the unforced system (3.60). Even with a very small gain k, it is assured that the system is bounded and that it will converge to the unforced system in finite time, and thus the asymptotic stability is always guaranteed. A higher value of k leads the value of ϕ to zero faster, thus leading to a faster convergence.

Hence, a higher value of gain k is desirable to enable a better performance of the controller. Ideally, gain k would be low for higher values of ϕ, and it could increase as ϕ decreases, ensuring that the control input never exceeds the UAV maximum heading rate. Such an adaptive approach of the control gain is possible, as the only condition required for the asymptotic stability is for the gain k to be positive. Therefore, assuming that the value of ω_ρ is always within the bound of ω_max, the value of k can be continuously adjusted so that the resulting control input ω stays also within the same bound.

An adaptive solution for the control gain k is then proposed and will be implemented in every further simulation. A nominal gain k^* is considered as the desired gain. Then, based on the current value of ω_ρ and the current error ϕ, if the resulting control input, ω, computed with gain k^*, exceeds the bound ω_{max}, the actual value of k to be used in the controller is computed such that the resulting control input match the limit of $\omega = \omega_{\text{max}}$. This is only possible if $\omega_\rho \leq \omega_{\text{max}}$, which should always be verified.

A simulation is presented in Figure 4.15, where the adopted solution for the adaptive control gain k is depicted. On the left side simulation, where a constant gain $k = 0.8$ is applied, it is possible to see that the control input exceeds the bound ω_{max} in the beginning of the simulation. However, the relative heading rate ω_ρ is within the bounds, and, thus, with the adaptation of the control gain, it is possible to limit the resulting control input, as in the simulation of the right side in Figure 4.15.

Hence, with the adaptive control gain solution, it is only left to ensure that the value of ω_ρ never exceeds the bound $\omega_{\text{max}} = 1$ rad/s, so that a feasible control input can be always given to the UAV heading rate. This condition will be assessed in the following section with the analysis of the control parameters ε and R.

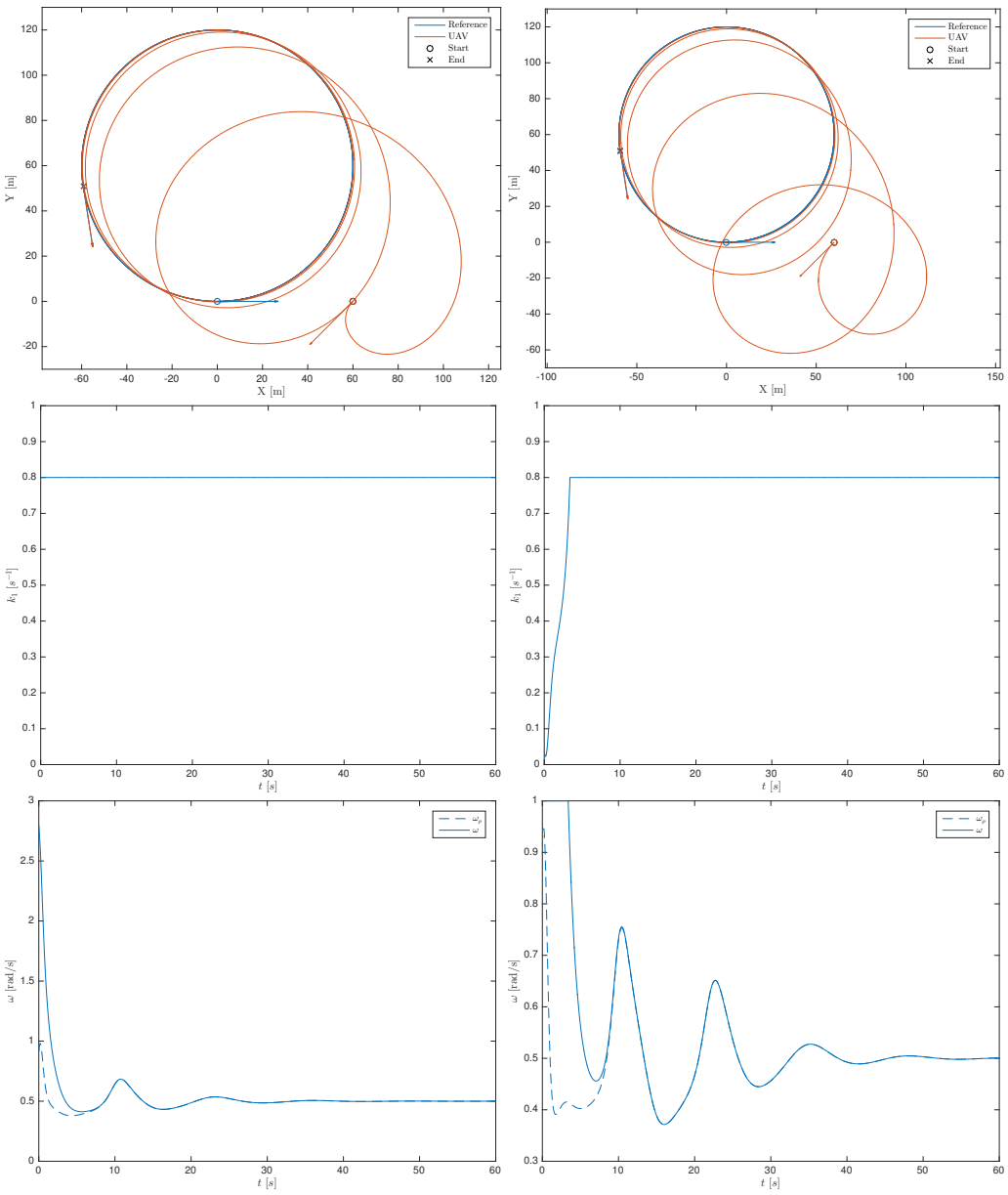

(a) Constant control gain $k = 0.8$ (b) Adaptive control gain $k \leq 0.8$

Figure 4.15: Assessment of the adopted solution for the adaptive control gain k

4.2.3.2 Control parameters ε and R

The formulation of the proposed approach for the tracking control problem is based on the definition of vector $\boldsymbol{\delta}$, which was defined to be proportional to the squared norm of the distance between the UAV and the reference point, in (3.23). The state variables derived to model the system dynamics are defined with respect to a relative vector $\mathbf{z}$, defined from the UAV to the tip of vector $\boldsymbol{\delta}$ and written as $\mathbf{z} = \mathbf{d} + \boldsymbol{\delta}$. Hence, the relative system dynamics is strongly affected by the norm of vector $\boldsymbol{\delta}$, and, thus, given its definition, $\delta(d^2) = \varepsilon d^2 + R$, by control parameters ε and R. In practice, these control parameters will affect the resulting control law to steer the UAV to the reference trajectory, especially the dynamics of the relative heading, ω_ρ, which is the main parameter that has to be bounded by the UAV maximum heading rate in order to provide a feasible control input.

In Chapter 3.6, an algorithm was derived to compute several pairs of parameters (ε, R), giving sufficient conditions to ensure the enforcement of the actuation bounds, given the maximum value of the reference trajectory heading rate.

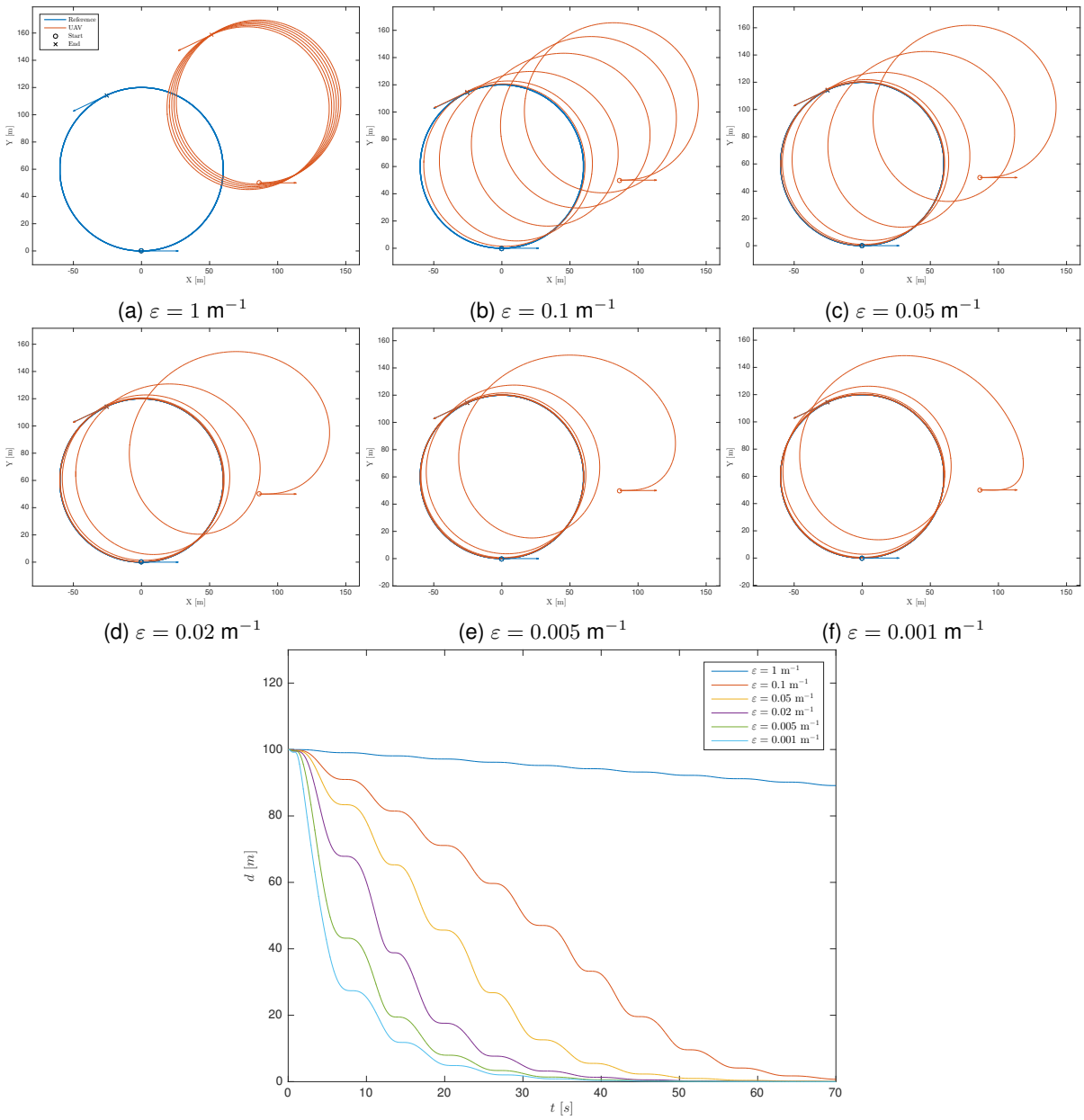

(a) $\varepsilon = 1$ m^{-1} (b) $\varepsilon = 0.1$ m^{-1} (c) $\varepsilon = 0.05$ m^{-1}

(d) $\varepsilon = 0.02$ m^{-1} (e) $\varepsilon = 0.005$ m^{-1} (f) $\varepsilon = 0.001$ m^{-1}

(g) Evolution of the distance for each value of ε

Figure 4.16: Variation of parameter ε, for a constant value of $R = 112$ m

The first set of simulation results is depicted in Figure 4.16, where different values of ε are applied

for the same value of R. It is possible to understand the effect of parameter ε, which sets the weight to be given to the squared norm of the distance in the value of δ. A higher value of ε leads to a very high δ for large distance errors, and thus to a slower convergence. As the value of ε decreases, the resulting performance is enhanced but below a certain value, the control input may saturate. In the stated example, where $\omega_r = 0.5$ rad/s and R is set to $R = 112$ m, the minimum value of ε that ensures a global boundedness of $|\omega_\rho| \leq -1$ rad/s is $\varepsilon = 0.02$ m^{-1}, as given in Table 3.2. Additionally, in figure 4.16g, it is possible to notice the influence of parameter ε in the evolution of the distance error. It is evident that the rate of reduction of the distance is much different between the curves while the distance is higher than when the distance gets close to zero. This happens because parameter ε has a bigger effect for large distance errors, while parameter R dominates the value of δ when the distance approaches zero.

In Figure 4.17, a set of simulation results is shown, selecting different values of parameter R, for a fixed value of $\varepsilon = 0.02$ m^{-1}. From Table 3.2, for $\varepsilon = 0.02$ m^{-1}, the minimum value of R to ensure a global feasibility of the control law is $R = 112$ m. For lower values of R, we can see that, despite leading to a better performance, the control input may saturate for shorter distance errors. On the other side, for higher values of R, performance is compromised, yet resulting in a more suitable control input.

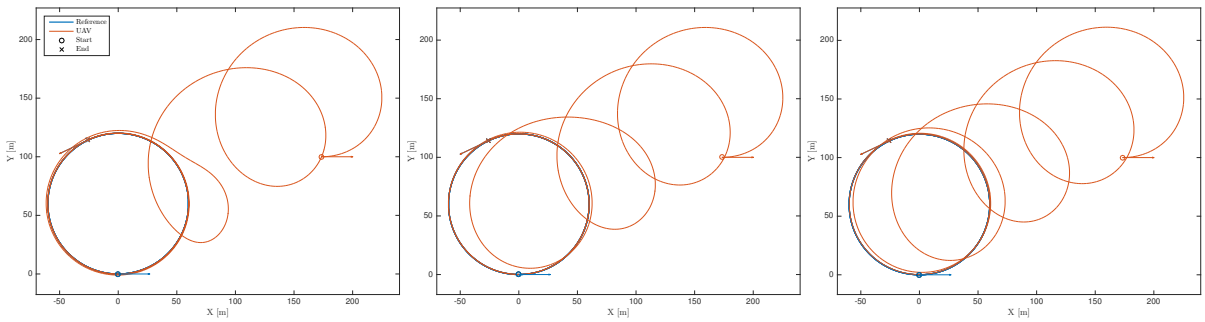

(a) $R = 20$ m (b) $R = 50$ m (c) $R = 80$ m

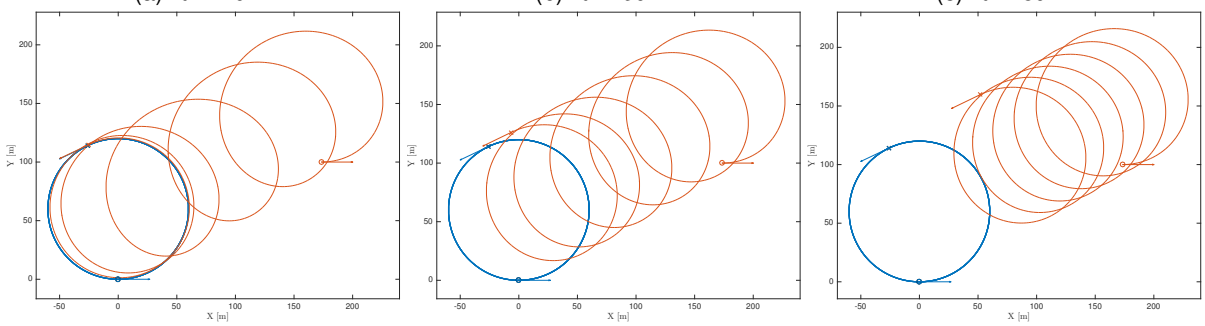

(d) $R = 112$ m (e) $R = 300$ m (f) $R = 900$ m

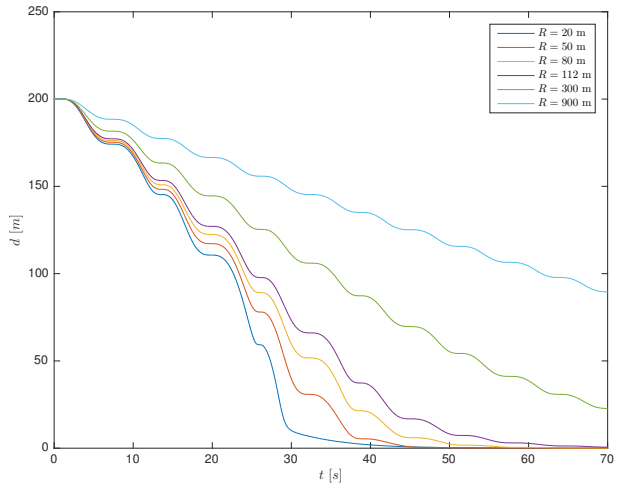

(g) Evolution of the distance for each value of R

Figure 4.17: Variation of parameter R, for a constant value of $\varepsilon = 0.02$ m^{-1}

From Figure 4.17g, it is clear to see that, when varying parameter R for a fixed value of ε, the convergence rate of the distance is closer between the different curves when the distance error is larger, and more distinct as the distance approaches zero. Comparing Figure 4.17g with Figure 4.16g, it is clear that parameter ε has more influence on the value of δ, and thus on the performance of the system for higher values of the distance error, but, as the distance decreases, the term εd^2 in (3.23) becomes weaker and parameter R dominates.

Hence, a trade-off is required between the value of parameters ε and R in order to understand which combination leads to the best performance of the system in terms of convergence time. It was already concluded that, for a fixed value of ε the best trade-off between convergence rate and control effort is ensured by applying the corresponding value of R depicted in Table 3.2, and the analogous stands for a fixed value of R. Moreover, since all pairs (ε, R) presented in Table 3.2 ensure a suitable control law, they should compared, in order to evaluate which one provides better performance. Looking at Table 3.2, one can see that, for a given value of ω_r, as the value of parameter ε decreases, the corresponding R increases, as expected. Hence, one should evaluate which pair provides the better performance: either if it is better to have a lower value of ε with the corresponding high value of R, or if a higher ε is preferable so that a lower value of R can be applied.

A series of simulation results is now depicted in Figure 4.18, where the different pairs of parameters ε and R from Table 3.2 are applied, for a reference heading rate of $\omega_r = 0.5$ rad/s, in order to evaluate which combinations lead to the best performance of the system:

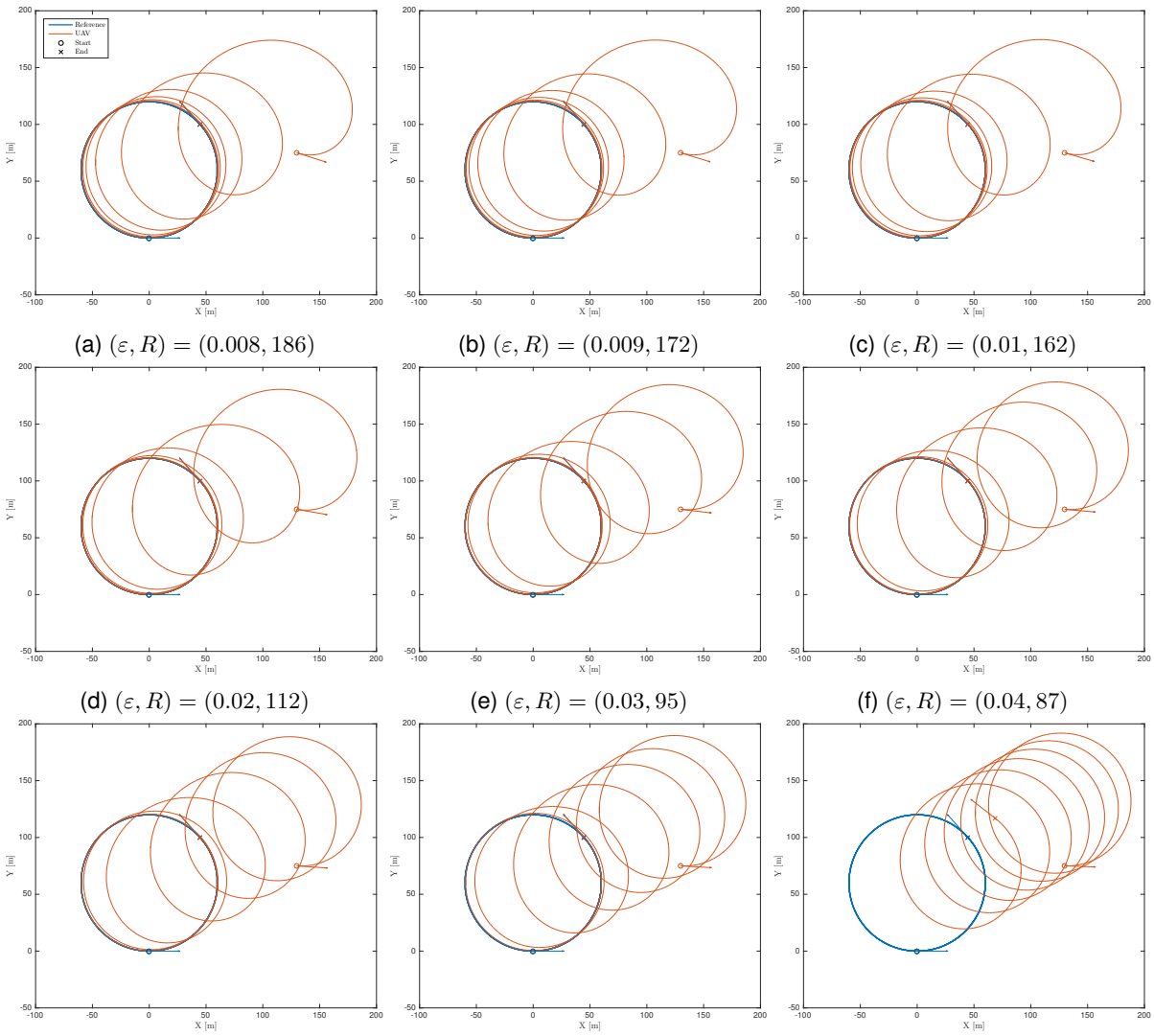

(a) $(\varepsilon, R) = (0.008, 186)$ (b) $(\varepsilon, R) = (0.009, 172)$ (c) $(\varepsilon, R) = (0.01, 162)$

(d) $(\varepsilon, R) = (0.02, 112)$ (e) $(\varepsilon, R) = (0.03, 95)$ (f) $(\varepsilon, R) = (0.04, 87)$

(g) $(\varepsilon, R) = (0.05, 82)$ (h) $(\varepsilon, R) = (0.06, 78)$ (i) $(\varepsilon, R) = (0.1, 71)$

Figure 4.18: Simulations with different pairs of parameters (ε, R) from Table 3.2, for $\omega_r = 0.5\ [rad/s]$

Analyzing the results in Figure 4.18 and comparing the resulting UAV trajectories for different com-

binations of the control parameters, one may infer the restricted range for the values of the parameters that enable a good convergence. Higher values of parameter ε, starting in the order of magnitude of 0.1, lead to the deterioration of the performance, as the convergence of the UAV to the reference point becomes much slower. On the other hand, lower values of ε, particularly below the order of magnitude of 0.01, require much higher values of R to enforce the actuation bounds, and, thus, despite having better convergence for large distances, the performance is compromised when the error distance decreases.

Additionally, in order to enable a more accurate analysis, the evolution of the distance resulting from the previous simulations with the different pairs (ε, R), is depicted in Figure 4.19. Here, the performance of the different combinations of parameters can be seen in more detail, particularly in the beginning and in the end of the simulation. In the first seconds of the simulations, it is very clear the difference between the different values of ε, and the lower the value of ε, the faster the convergence. However, a lower value of ε does not imply a good performance in the whole simulation, as its corresponding parameter R is larger, and thus the rate of convergence decreases as the distance decrease. This is clear from the detail of the end of the simulation, where the combinations which had the faster convergence in the beginning – namely $(\varepsilon, R) = (0.008, 186)$, $(\varepsilon, R) = (0.009, 172)$ and $(\varepsilon, R) = (0.01, 162)$ – have a slower convergence in the end, due to the high values of R. The pair of parameters that leads to the best performance is the one with $(\varepsilon, R) = (0.02, 112)$, which provides a satisfactory convergence rate for larger distances, as well as a very good convergence when the UAV approaches the reference point, leading to the best trade-off between control effort and convergence rate.

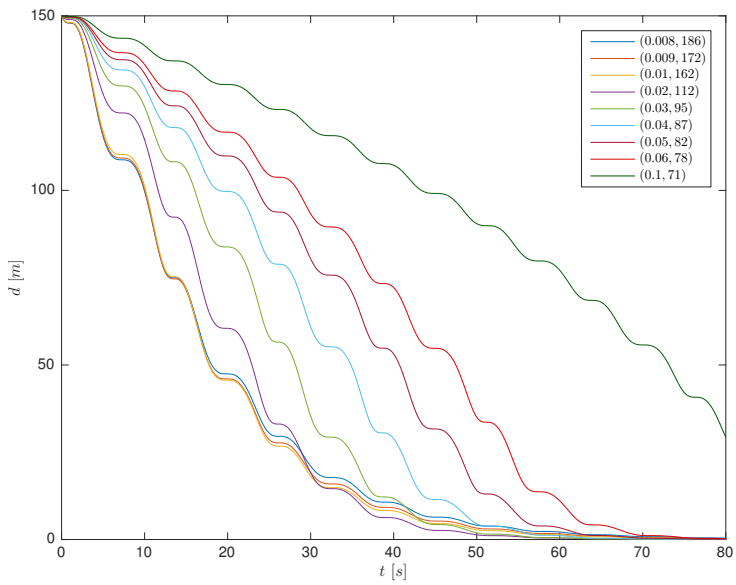

(a) Evolution of the distance d during the whole simulation

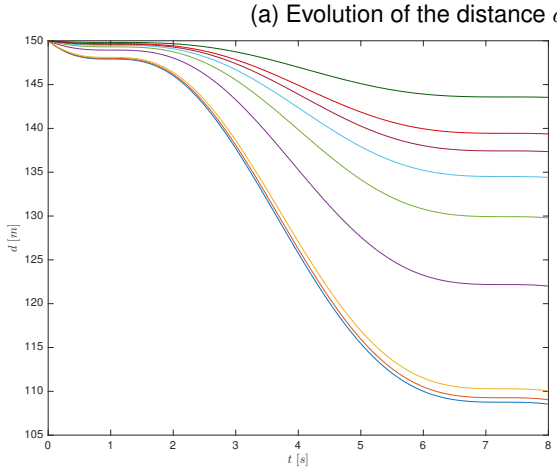

(b) Detail of the beginning of the simulation

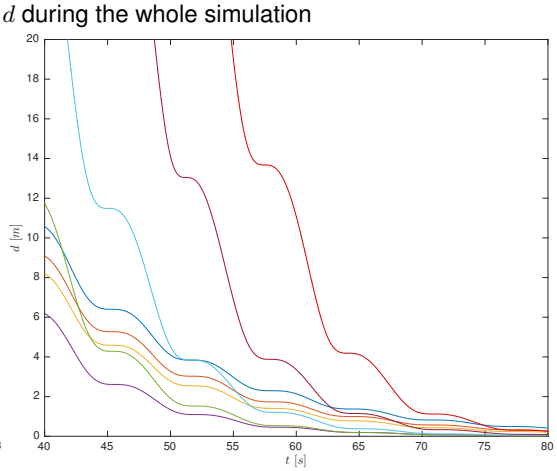

(c) Detail of the end of the simulation

Figure 4.19: Distance between the UAV and the reference point, for the different pairs of (ε, R)

4.2.4 Tracking reference trajectories with different constant heading rates

In all the simulations presented so far, the reference heading rate was set to a constant reference of $\omega_r = 0.5$ rad/s. However, this value was used only for simplicity, and the application of the proposed tracking control approach is not restricted to this condition. In Figures 4.20 and 4.21, the extreme cases with different reference heading rates are depicted, respectively a straight-line reference trajectory, where $\omega_r = 0$ rad/s, and a reference trajectory with the maximum UAV heading rate, $\omega_r = 1$ rad/s.

In the first case, where a straight-line reference trajectory is considered, two simulations were performed with different initial conditions, and are depicted in Figure 4.20. This is the particular case in which asymptotic stability cannot be guaranteed for this tracking control problem. As resulting from condition (3.50), if a straight-line reference is considered, one can only guarantee that the relative angles ϕ_r and ϕ converge to zero. Concerning the convergence of ρ, one can only ensure that it converges to a constant value. However, it is not trivial to estimate that steady-state value. Hence, for a straight-line reference, one can only guarantee that the UAV converges to the reference path, but the steady-state distance error depends on the initial conditions.Moreover, given the proposed approach – with the definition of vector $\boldsymbol{\delta}$ and the redefinition of the line-of-sight control objective –, the steady-state position of the UAV in the reference path can be either behind or ahead of the reference point, depending on the initial conditions, as confirmed on both simulations of Figure 4.20.

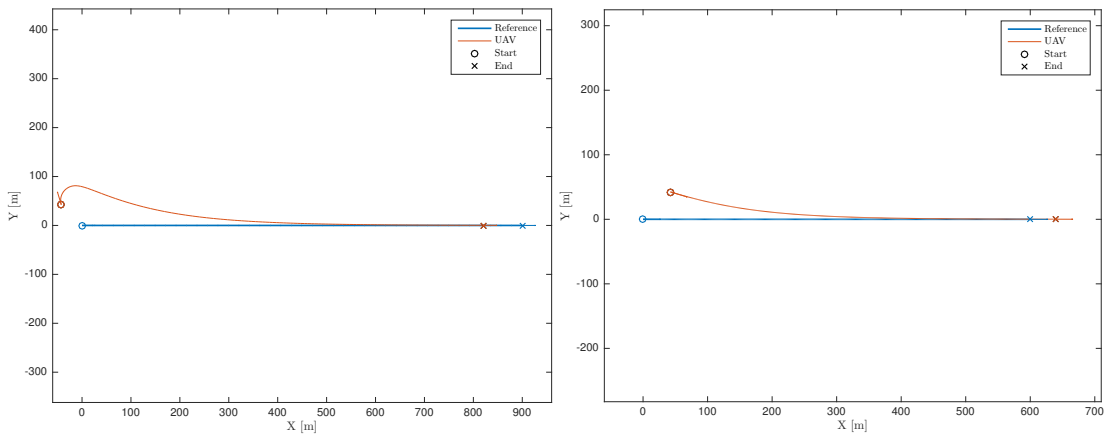

Figure 4.20: Tracking a reference trajectory with constant heading rate $\omega_r = 0$ rad/s, for different initial conditions

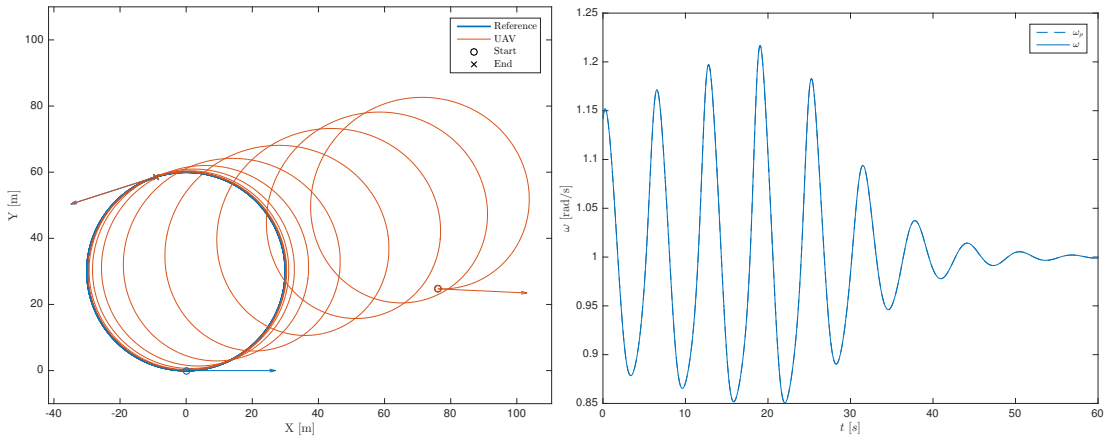

Figure 4.21: Tracking a reference trajectory with the maximum UAV heading rate $\omega_r = \omega_{\text{max}} = 1$ rad/s

In Figure 4.21, the tracking problem is assessed with a constant heading rate reference which has exactly the maximum heading rate achievable by the UAV. In this extreme case, it is not possible to enforce the actuation bounds with a control law able to steer the UAV from any initial position to the reference point without reaching the saturation of the control input. With the proposed control approach, the resulting UAV commanded heading rate will have oscillations around the desired (reference) value,

and thus, if the desired heading rate is exactly the maximum supported by the UAV, a robust control law cannot be provided for this particular case.

However, for the tracking control problem assessed in this dissertation, the reference trajectory is generated by a guidance system which can be directly controlled. Thus, guidance and control systems can be further interconnected and a more involved motion planning method can be developed. The guidance system can receive specific information from the control system – such as the tracking distance error – and can use this information to generate the reference trajectory.

This motion planning system can be designed in numerous manners, depending on the overall tracking objective. In Figure 4.22, a possible solution is presented, for a motion planning system where the goal is to lead the UAV to a reference trajectory with its maximum heading rate while enforcing the actuation bounds. Here the guidance system generates firstly a reference trajectory with a lower heading rate of $\omega_r = 0.5$ rad/s, and when the tracking distance error from the control system decreases down to zero, then the reference trajectory starts to linearly increase its heading rate until reaching the bound of $\omega_r = 1$ rad/s. As can be observed from the results presented in Figure 4.22, with this solution the UAV is able to reach a desired trajectory with its maximum heading rate, always ensuring that this value is never exceeded. Nevertheless, this is only one possible solution for this issue, and several improvements can be applied in order to adjust the reference trajectory to each specific main problem.

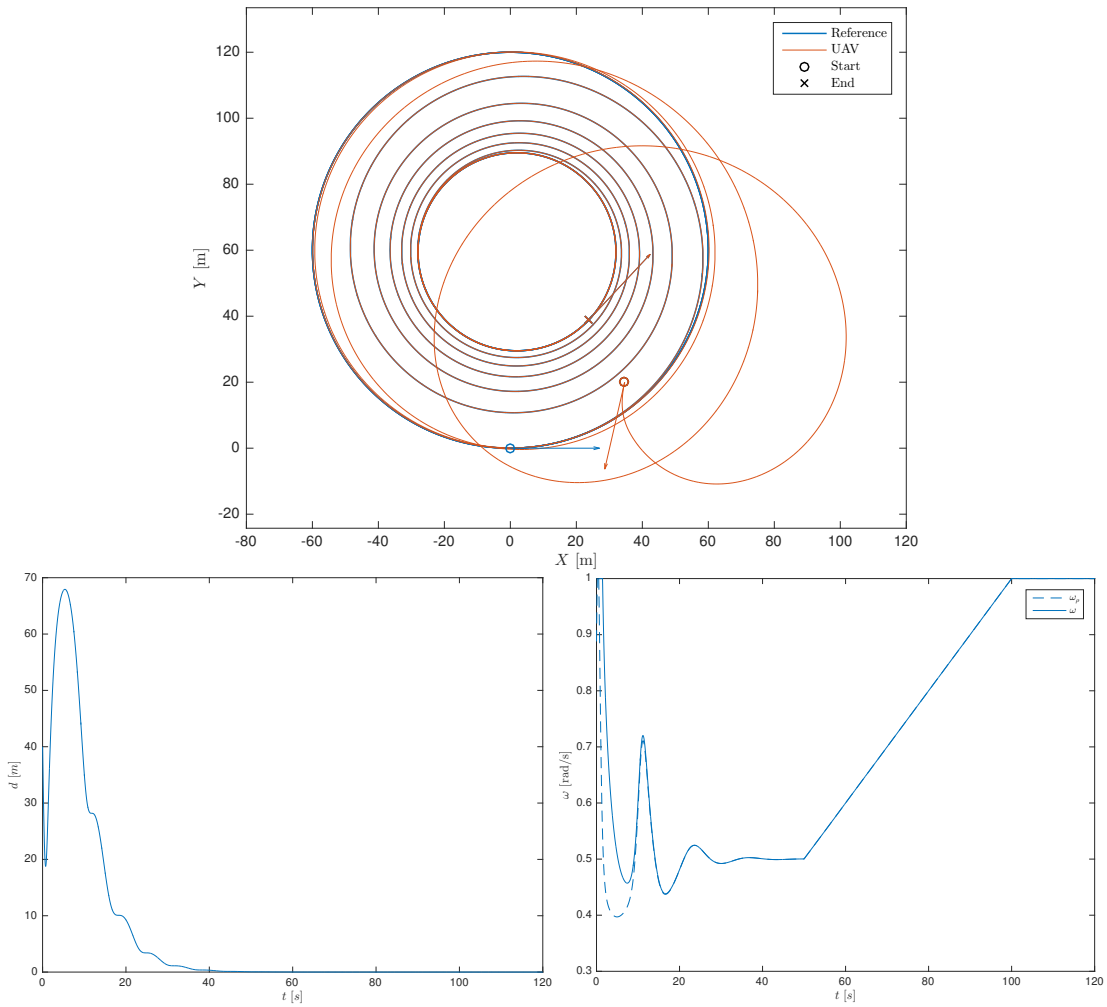

Figure 4.22: Motion planning solution for the tracking control of a circular trajectory with the maximum heading rate, while enforcing the actuation bounds

4.2.5 Perturbations

So far, in the tracking control problem assessed in this dissertation, only ideal conditions were considered for the relative system dynamics. However, in practice, several perturbations can be present and perturb the nominal system dynamics. The ideal conditions were considered in the present study to obtain

a sound theoretical basis for further analysis. In this section, we present some results obtained in simulation when some typical disturbances are present, in order to understand how the tracking control error is affected.

4.2.5.1 UAV speed offset

Firstly, a disturbance in the UAV true speed is assessed. So far, it was always assumed that the UAV was able to keep track with the reference speed. However, the UAV true speed can differ from the given reference, e.g. due to a malfunction on the sensors or from a constant error coming from the inner-loop controller responsible for the reference speed tracking.

In the following figures, two simulations are presented, in which a constant speed offset disturbance is applied to the UAV speed. In Figure 4.23, a UAV speed of $V = 0.8V_{\text{r}}$ is considered, while in Figure 4.24 the UAV speed was set to $V = 1.2V_{\text{r}}$, for a circular reference trajectory with $\omega_r = 0.5$ rad/s in both cases. It is possible to see that in both simulations the UAV is not able to track exactly the reference trajectory. Instead, it converges to a circular trajectory concentric with the reference but with a different radius. This result is intuitive since, with the proposed tracking control approach, the UAV will align its heading with the tip of vector $\boldsymbol{\delta}$, leading to a circular trajectory with the same angular speed ω_r. Hence, given the speed differential, the resulting trajectory will have a different radius, leading to a constant steady-state distance error. Moreover, as can be observed in both figures, the steady-state distance is not the minimum possible given both circular trajectories, as the resulting UAV trajectory is slightly out of phase compared with the reference. This is due to the alignment of the UAV heading with a virtual point in the tip of vector $\boldsymbol{\delta}$, and only an infinite δ would lead to the exact phasing of both trajectories. Nevertheless, one concludes that the system response to a constant offset on the UAV speed is fairly acceptable, as it is able to converge to a minimum steady-state distance error, tracking a circular reference trajectory.

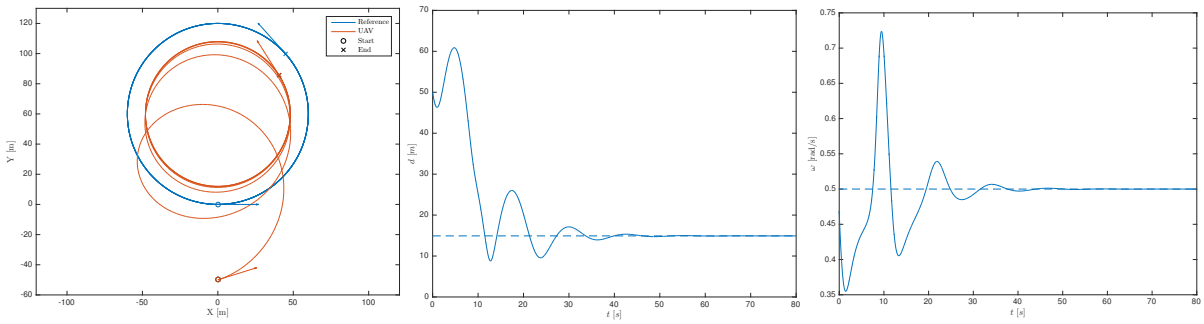

Figure 4.23: UAV speed offset, UAV slower than the reference

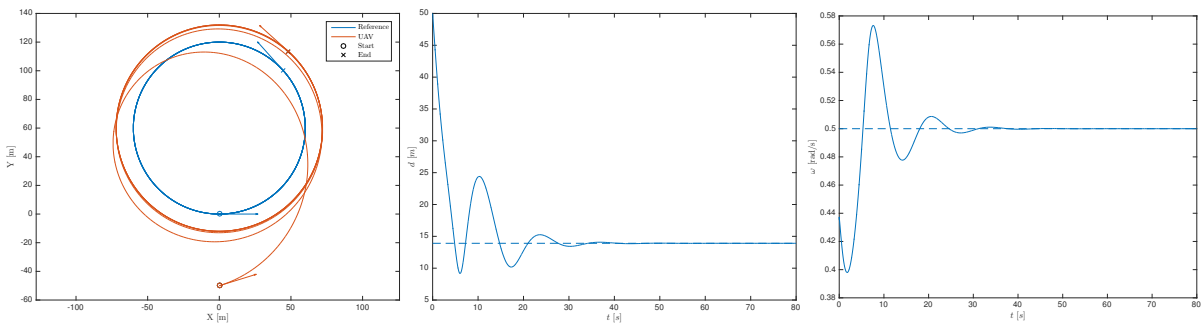

Figure 4.24: UAV speed offset, UAV faster than the reference

4.2.5.2 Constant Wind

Another typical disturbance inherent to the UAV operation is the wind. So far, the UAV true speed was considered to be exactly the ground speed. However, the UAV moves in relation to the airmass which, in turn, can have its own motion. Hence, the UAV motion in the presence of a non-steady wind will differ from the dynamics considered for the reference point generation, and thus, it is predictable that the UAV will not be able to track perfectly the reference trajectory.

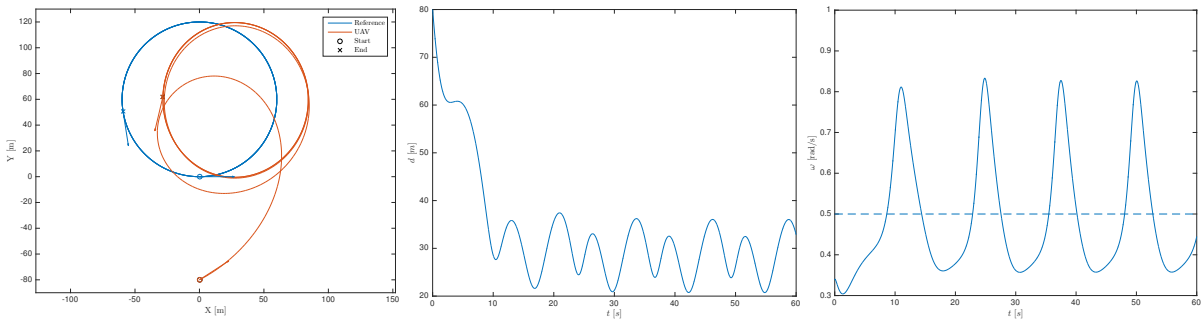

Figure 4.25: Tracking a circular trajectory in the presence of constant wind, where a bounded tracking error is reached

In order to evaluate the performance of the proposed control approach in the presence of a constant wind, a simulation was performed and the corresponding results are depicted in Figure 4.25. Here a constant wind is considered, with constant speed $V_w = 0.2V_\mathrm{r}$ and constant heading $\chi_w = 0$ rad. Analyzing the results from this simulation, one can see that in this case the resulting UAV trajectory will be similar to the reference, but shifted in the wind direction. Despite the absence of a perfect reference tracking, one can also notice that the distance error converges initially and remains in a bounded region. Moreover, as depicted in the time evolution of the control input, the resulting commanded UAV heading rate will be significantly compromised in order to lead to a circular trajectory. This is a problematic issue, as more critical conditions can lead to the saturation of the control input. Even with the adjustment of the control parameters of the proposed δ-control approach, which allow the reduction of the demanded control input, the problem cannot be solved. As we can observe in the simulation of Figure 4.26, if parameters ε and R are increased, the commanded heading rate will be reduced. However, it will lead to a divergence of the tracking error.

This is an unavoidable problem since, in the presence of wind, tracking a circular trajectory can be unachievable by a UAV, as we are assuming an incorrect UAV motion for the generation of the reference trajectory. Hence, in order to deal with the presence of non-steady wind, the guidance system needs to be reformulated, in order to consider this wind disturbance in the generated reference trajectory, providing a feasible reference to the UAV.

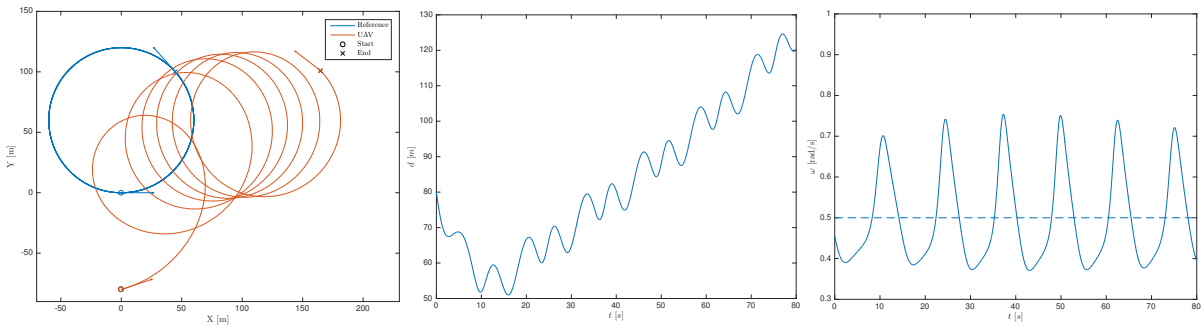

Figure 4.26: Tracking a circular trajectory in the presence of constant wind, where the tracking error will diverge

4.3 Guidance and Control System Implementation

As a consequence of the thorough analysis held in the previous section where the behavior of the proposed δ-control approach was assessed in different simulation scenarios, the available control parameters were calibrated and a trade-off between control effort and convergence rate was achieved. The designed control system is now implemented, together with the guidance system, and some scenarios are simulated in order to understand how the proposed controller can be adapted to a reference trajectory with a time-varying heading rate. First, some results are presented, in which the performance of the controller is validated for the kind of trajectories generated by our guidance system. Finally, the overall system of Figure 4.1 is implemented, and the main results of the UAV-based tracking of a marine vessel and the passage through the smoke plume are assessed.

In Figure 4.27, simulation results are presented, in which the tracking problem is implemented with a typical reference trajectory from the designed guidance system. Here, the case of a static vessel was considered, and, thus a speed ratio of $\nu = 0$, leading to a trajectory with the shape of a Lemniscate of Bernoulli. The maximum reference heading rate is $(\omega_r)_{\text{max}} = 0.5$ rad/s, and thus, from the results of the previous section, the pair of parameters $(\varepsilon, R) = (0.02, 112)$ provides the best performance for a tracking control law within the actuation bounds. In these conditions, it is ensured that the commanded heading rate is always feasible by the UAV for any initial configuration. The previously proposed solution for the adaptive tuning of the control gain k_1 is always applied, ensuring a reasonable convergence of the state variable ϕ while avoiding a controller saturation when large initial errors occur.

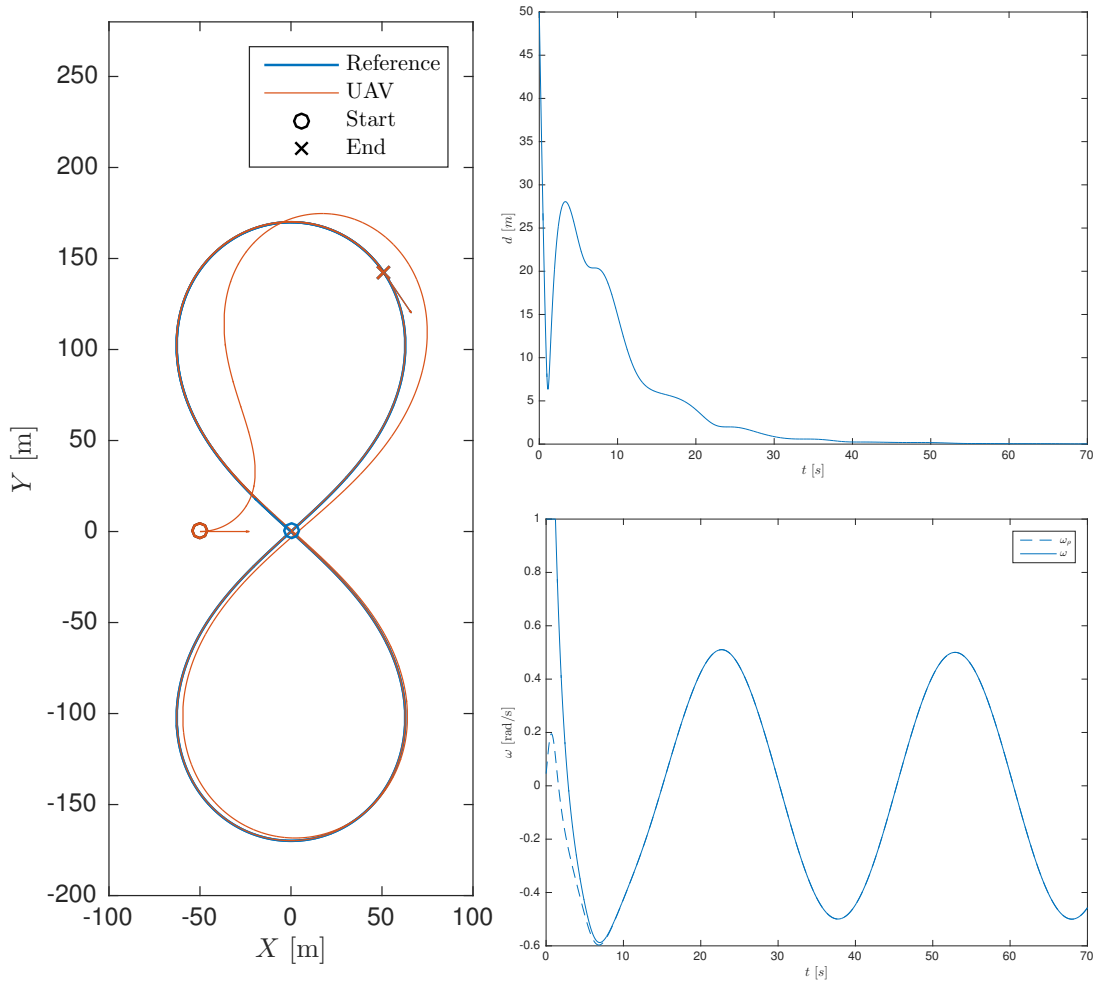

Figure 4.27: Tracking a reference trajectory from the guidance system, with $(\omega_r)_{\text{max}} = 0.5$ rad/s, for a speed ratio of $\nu = 0$

Similarly, in Figure 4.28, a reference trajectory from the guidance system is considered, this time for a speed ratio of $\nu = 0.5$. In this simulation, a larger initial error was considered, in order to assess the convergence of the trajectory with the proposed control approach. The resulting UAV trajectory starts to align with the reference from the first instants, leading to a relatively fast and smooth convergence to the desired trajectory.

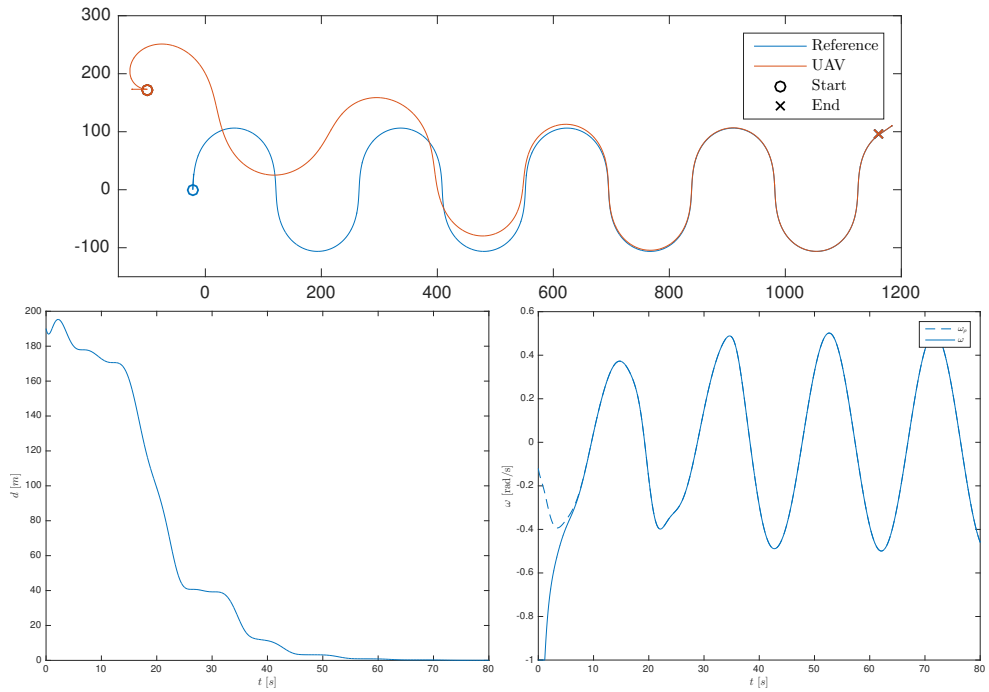

Figure 4.28: Tracking a reference trajectory from the guidance system, with $(\omega_r)_{\text{max}} = 0.5$ rad/s, for a speed ratio of $\nu = 0.5$

However, the previous two simulations considered a maximum reference heading rate of $(\omega_r)_{\text{max}} = 0.5$ rad/s, and, thus, looking upon the final objective of tracking a vessel, the full capacity of the UAV is not harnessed. Considering the periodicity between consecutive crossings of the CO, that will correspond to the crossings through the smoke plume, it is desirable to have a higher periodicity, in order to optimize the smoke gas measurements. Hence, the reduction of the oscillation period is attainable by the increasing of the maximum reference heading rate, thus taking advantage of the full capabilities of the UAV. However, it is not possible to ensure a robust tracking control when the reference heading rate reaches the bound $\omega_{\text{max}} = 1$ rad/s, as seen in the previous section for a circular trajectory, and confirmed in the example depicted in Figure 4.29 for a reference trajectory from the guidance system:

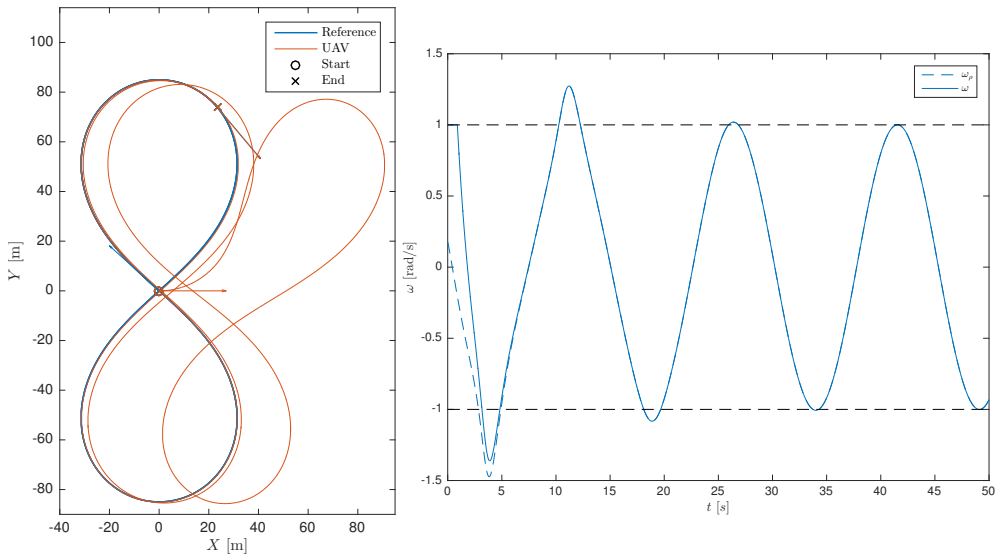

Figure 4.29: Tracking a reference trajectory from the guidance system, with $(\omega_r)_{\text{max}} = 1$ rad/s, for a speed ratio of $\nu = 0$

In order to solve the previous problem, and to be able to lead the UAV to a reference trajectory with the maximum heading rate $(\omega_r)_{\text{max}} = (\omega)_{\text{max}} = 1$ rad/s, while enforcing the actuation bounds when the

tracking error is present, a motion planning solution is presented, similarly to the one applied in Figure 4.22. Given the oscillatory heading rate approach of our guidance system, it is certain that the trajectory will always cross the CO, regardless of the oscillatory frequency ω_0. Hence, the oscillatory frequency ω_0 can be switched whenever the reference point is crossing the CO, with no displacement of the resulting reference trajectory.

Therefore, one can design a motion planning system in which the guidance system receives as input the tracking distance error, d, from the control system. From the beginning of the simulation, and while the distance error is not zero, the frequency of the oscillatory reference heading rate is chosen such that $(\omega_r)_{\text{max}} = 0.5$ rad/s. When the tracking distance error decreases down to zero, the frequency is switched in the end of the current period of the reference heading rate, such that in the following period the maximum reference heading rate reaches the bound $(\omega_r)_{\text{max}} = 1$ rad/s.

The outcome of this implementation is illustrated in Figure 4.30, where its effectiveness can be better understood. One can observe that, while the distance error is greater than zero, the maximum reference heading rate of the oscillation is $(\omega_r)_{\text{max}} = 0.5$ rad/s and thus the pair of parameters $(\varepsilon, R) = (0.02, 112)$ guarantees that the controller never saturates. When the tracking error approaches zero and the UAV proceeds with the same motion as the reference point, then the guidance system updates the oscillation frequency, so that the resulting reference trajectory has the maximum heading rate of $(\omega_r)_{\text{max}} = 1$ rad/s which can now be achievable by the UAV.

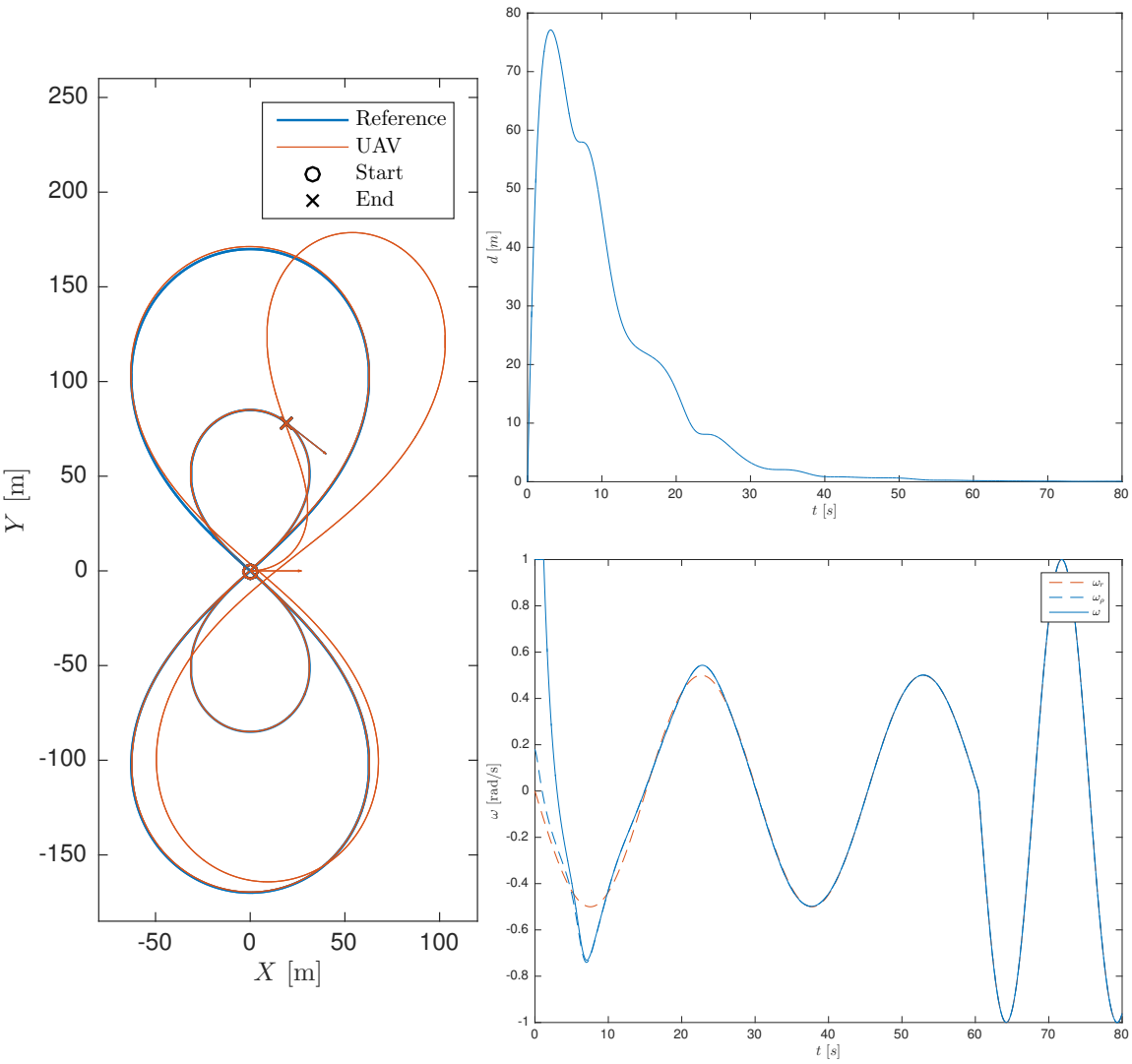

Figure 4.30: Tracking a reference trajectory from the guidance system, with adaptive oscillation frequency ω_0, for a speed ratio of $\nu = 0$

4.3.1 Perturbations

Similarly to the circular reference trajectory, the impact of the stated disturbances on the system dynamics will be also assessed for the kind of trajectories generated from the guidance system. At first, a constant offset error will be added to the UAV speed and the performance of the system will be assessed in this scenario. Secondly, a constant wind will be introduced in the system. The impact on the tracking control performance will be assessed, and then a solution will be proposed to adjust the guidance system to the known constant wind.

4.3.1.1 UAV speed offset

Firstly, a simulation is performed in which a constant offset error is added to the UAV speed, which is considered to be $V = 1.2V_{\mathrm{r}}$. As depicted in Figure 4.31, the impact of this disturbance on this kind of trajectories is not so defective as for a circular reference. In this case, the amplitude of the oscillatory trajectory is widened as expected. However, the center of the resulting trajectory is very close to the CO, that corresponds to the point where the smoke plume measurements are to be performed. Hence, given the boundedness of the tracking distance error, and the feasibility of the commanded control input (achieved from the proper tuning of control parameters ε and R), this kind of disturbance has limited impact on the tracking control performance.

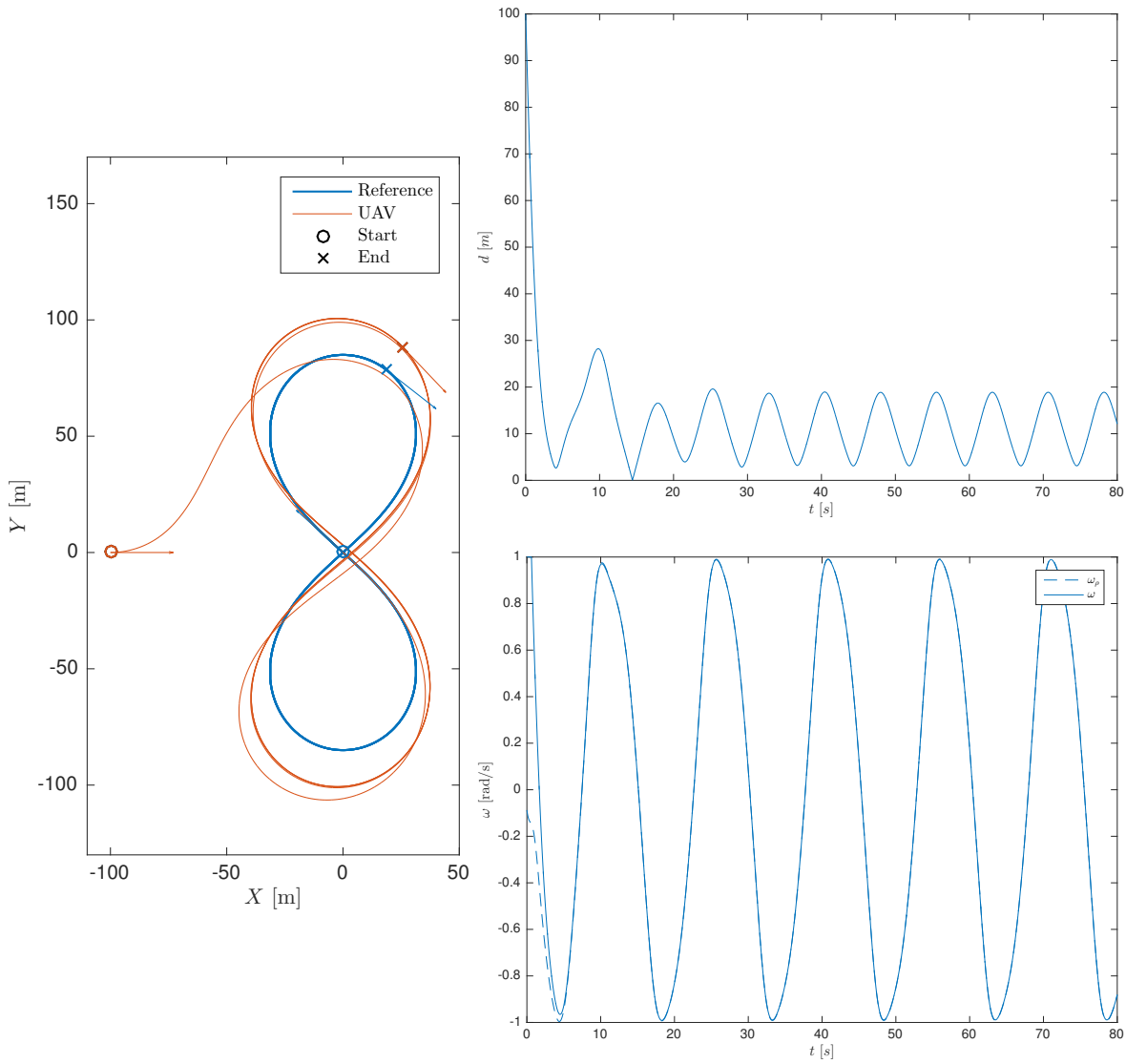

Figure 4.31: Tracking a reference trajectory from the guidance system, with a constant offset error in the UAV speed

4.3.1.2 Constant Wind

Now a constant wind will be added to the system in order to understand how the proposed guidance and control solution is affected by this disturbance, and, subsequently, an adaptation to the guidance system will be performed to enhance its performance in this scenario. A simulation is presented in Figure 4.32, where a constant wind, with speed $V_w = 0.2V_\mathrm{r}$ and heading $\chi_w = 0$ rad, is considered in the tracking of a reference trajectory from the guidance system, for a speed ratio of $\nu = 0$.

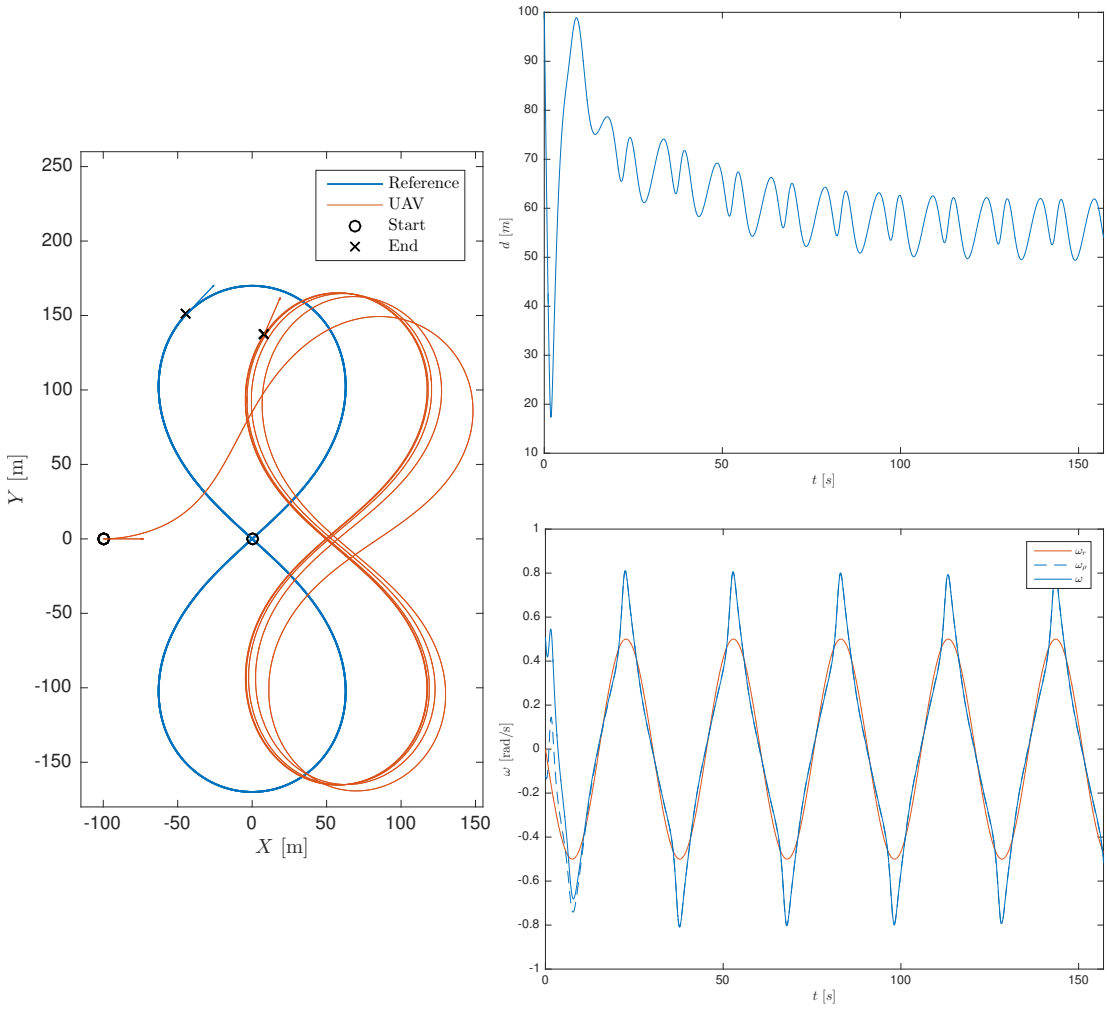

Figure 4.32: Tracking a reference trajectory from the guidance system, with a constant wind disturbance

Here, the effect of this disturbance is quite similar to the result of the simulation with the circular trajectory, depicted in Figure 4.25, with the resulting UAV trajectory being shifted to the wind direction. The tracking distance error converges to a bounded region with periodic oscillations and, as seen in both UAV and reference point positions at the end of the simulation, the resulting trajectories will be with similar orientations at every time instant. In this simulation, the oscillation frequency ω_0 was set so that the resulting maximum reference heading rate is $(\omega)_{\text{max}} = 0.5$ rad/s. When observing the resulting control input on the UAV heading rate, despite satisfying the bound $\omega < 1$ rad/s, it will not follow the same heading rate as the reference, having higher peaks above 0.5 rad/s necessary to compensate the wind speed. For more critical conditions, the control input can saturate, leading to a divergence of the tracking distance error, as happens in the simulation of Figure 4.26.

Given the results from the introduction of a constant wind in the previous simulation, and given the essence of the proposed guidance solution, which generates a reference trajectory with the UAV motion, able to keep track with a slower vessel, if the constant wind is assumed to be known, then a reference trajectory can be generated, able to compensate the displacement caused by the wind motion. Consider the reference point motion, first introduced in (2.7), now adapted to handle with the known wind motion,

namely the wind speed V_w and heading χ_w:

$$\dot{\mathbf{x}}_r = \begin{cases} \dot{x}_\mathsf{r} = V_\mathsf{r} \cos \chi_\mathsf{r} + V_w \cos \chi_w \\ \dot{y}_\mathsf{r} = V_\mathsf{r} \sin \chi_\mathsf{r} + V_w \sin \chi_w \\ \dot{\chi}_\mathsf{r} = -\eta \omega_0 \sin(\omega_0 t) + \omega_V \end{cases} , \tag{4.1}$$

Now the reference trajectory is generated in relation to the airmass, which is consistent with the resulting UAV motion. Moreover, the value of parameter η should be now adapted accordingly, and the apparent vessel velocity to the airmass should be considered instead of the vessel true speed. Hence, consider the wind triangle of Figure 1.1. With the ground velocity vector $\mathbf{v}_g$ corresponding to the vessel velocity $\mathbf{v}_V$ and with the vector $\mathbf{v}_a$ being the apparent vessel velocity in relation to the airmass, then the latter should be considered for the computation of parameter η, as the speed ratio is now defined as $\nu = V_a/V_\mathsf{r}$.

With the described modifications being implemented in the guidance system, it is presented in Figure 4.33 the results from a simulation for the same scenario as in Figure 4.32.

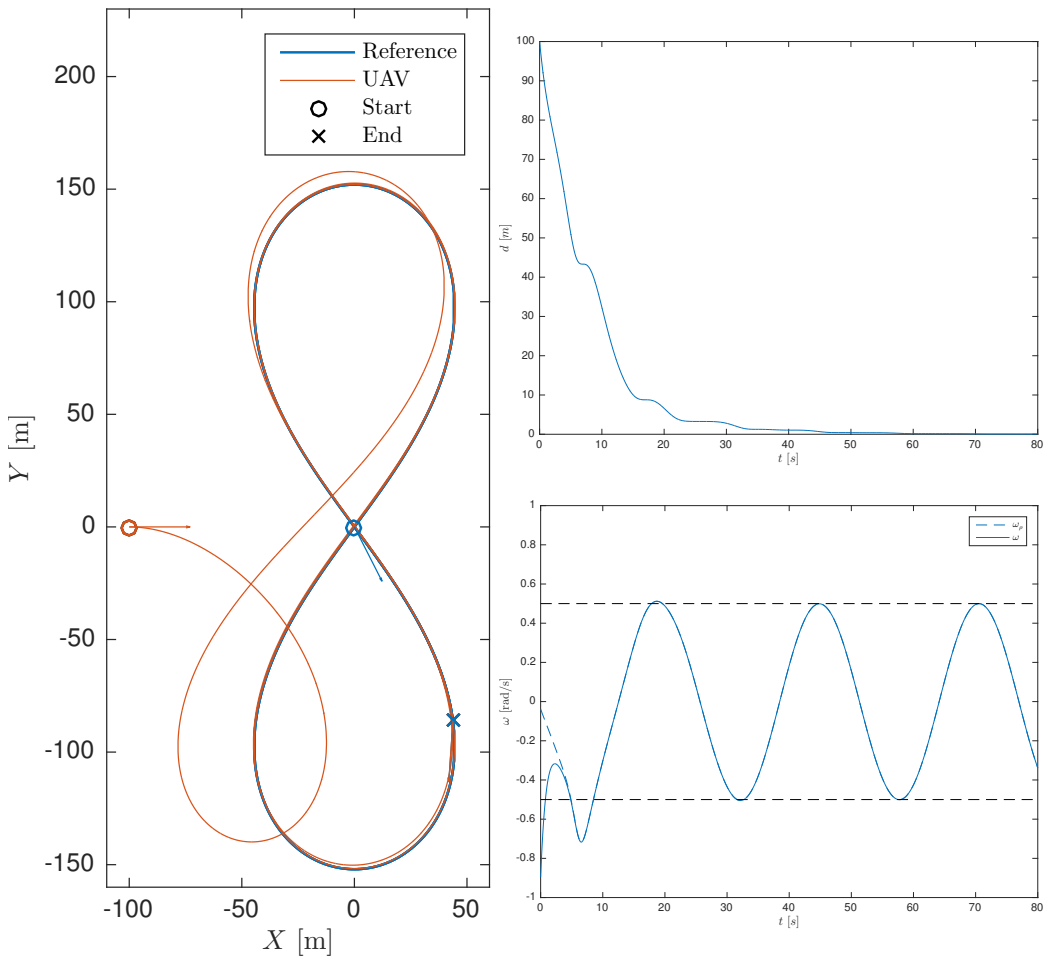

Figure 4.33: Tracking a reference trajectory from the guidance system, for a static vessel, with a constant wind disturbance

As seen in Figure 4.33, the proper generation of a reference trajectory where the constant wind velocity is taken into account enables a convergence of the UAV to the desired trajectory around the CO point. With this solution, the resulting trajectory is able to properly compensate the wind speed, as the parameter η is computed for an apparent speed ratio of $\nu = 0.2$. Hence, the resulting trajectory in relation to the airmass is equivalent to a trajectory generated in a zero wind condition, for a vessel moving with the speed $V_\mathsf{V} = 0.2 V_\mathsf{r}$. Even with the distortion of the trajectory in the inertial frame, the main objective of flying through the CO is achieved, leading to the correct crossing on the smoke plume measurement site.

Similarly, in Figure 4.34, where the vessel is considered to move with a speed $V_V = 0.5V_\mathrm{r}$. A steady wind speed is considered with a speed and heading of $(V_w, \chi_w) = (0.2V_\mathrm{r}, \pi/6 \text{ rad})$, respectively. The vessel is not represented in the figure. However, the CO moves with the same speed as the vessel and represents the desired point for the smoke plume measurement. One can see that the UAV is able to converge to the reference trajectory, compensating the effect of the steady wind, and flying above the CO twice every oscillation period of $T \approx 15$ s.

This adaptation of the guidance system, which generates the reference trajectory with respect to the airmass, considering the apparent velocity of the vessel, leads to the feasibility by the UAV, as the resulting tracking problem behaves as if the UAV was tracking a virtual UAV with the same motion. Hence, we can ensure that the UAV is able to attain the resulting control input on the commanded heading rate, contrarily to the scenario in Figure 4.32, where the reference trajectory did not consider the real UAV motion.

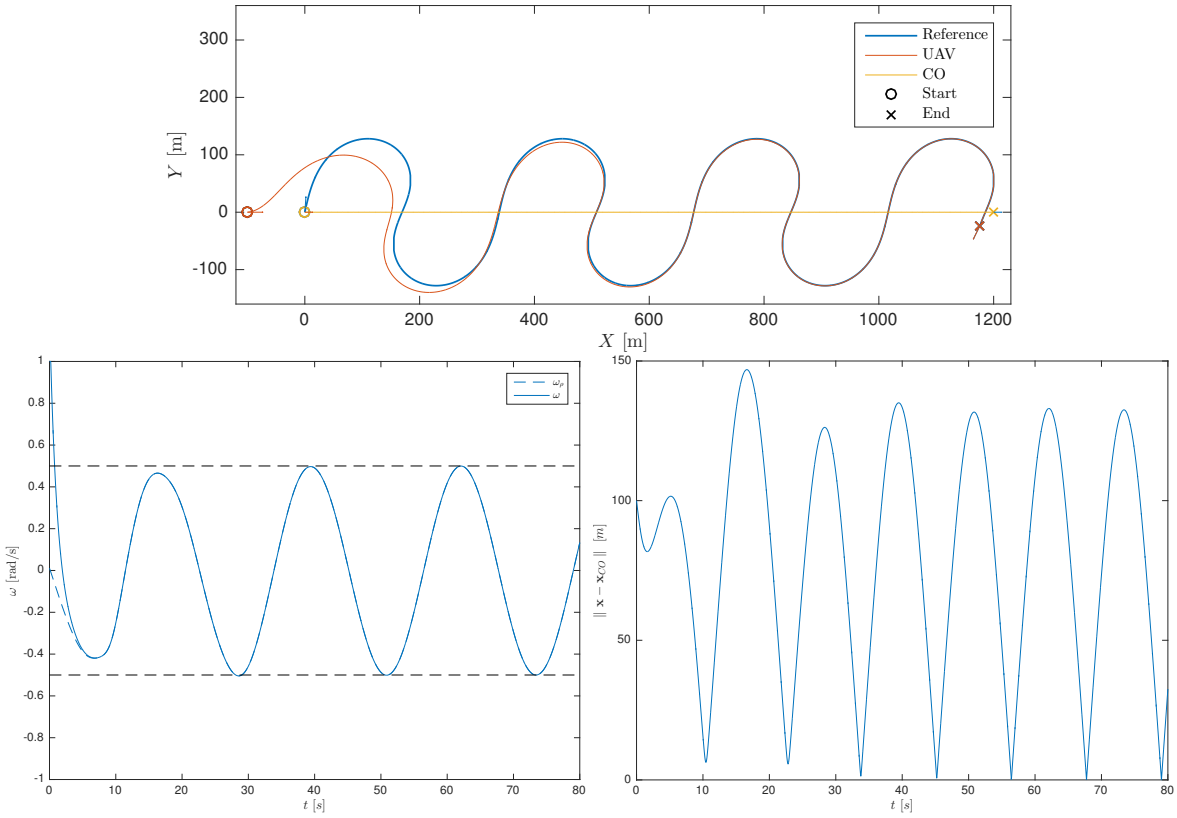

Figure 4.34: Tracking a reference trajectory from the guidance system, for a moving vessel, with a constant wind disturbance

4.3.2 Follow the vessel

After the presentation of a wide number of simulations, performed to validate the effectiveness of both the Guidance and the Control systems separately, it is left to present the results of the implementation of the overall system, as depicted in Figure 4.1. In Table 4.2, the most relevant parameters to be applied in the following final simulations are presented.

Table 4.2: Constant parameters to be applied in the final simulations

Speed ratio	$\nu = 0.5$
Smoke plume direction	$(\chi_P, \alpha_P) = (180, 50)$ deg
Oscillation amplitude	$\omega_0 \eta(\nu) = 0.5$ rad/s
Keep-out area radius	$r_\mathrm{min} = 200$ m
Control parameters	$(\varepsilon, R, k) = \left(0.02 \text{ m}^{-1}, 112 \text{ m}, 0.8 \text{ s}^{-1}\right)$

Firstly, a simulation is presented in Figure 4.35, where the overall system is implemented, revealing the main results of the UAV tracking to the smoke plume. In Figure 4.35a, the three-dimensional trajectories are depicted. Considering the vessel trajectory (blue line) with speed $V_{\mathrm{V}} = 0.5V_{\mathrm{r}}$, the reference trajectory (yellow line) is generated from the guidance system, expressing the desired trajectory for the UAV to track the vessel with the considered restrictions. The UAV starts in a random position behind the vessel, and a control command is generated from the control system, acting on the UAV heading rate, leading to the convergence of the UAV to the reference point trajectory. The convergence is relatively fast, and once the UAV reaches the reference point, it is kept in the desired trajectory.

In Figure 4.35b, the absolute distance between the vessel and the UAV is depicted for the entire simulation time. Here it can be confirmed that the UAV never enters the keep-out area, although being close to it. The distance between the vessel and the CO is represented by the dashed line and is computed from the second CO positioning method from (2.32), with d_{max} given from (2.33). The time instants in which the reference point crosses the CO are marked with a diamond and correspond to the desired points to perform the smoke plume measurements. After the UAV convergence to the reference trajectory, one can see that the UAV crosses the CO at those desired points. Moreover, from Figure 4.35c it can be confirmed that the UAV crosses the CO in the exact heading of the smoke plume, and thus, the desired point to perform the smoke plume measurements is periodically reached, every 9.5 s (half of the oscillation period T), at a distance of 214 m from the vessel.

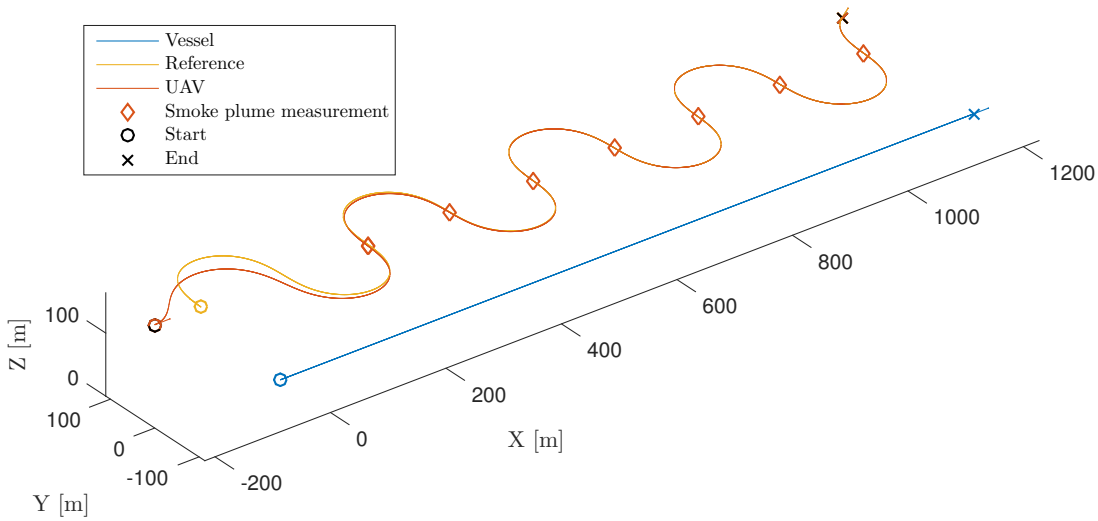

(a) Trajectories of vessel, reference, and UAV

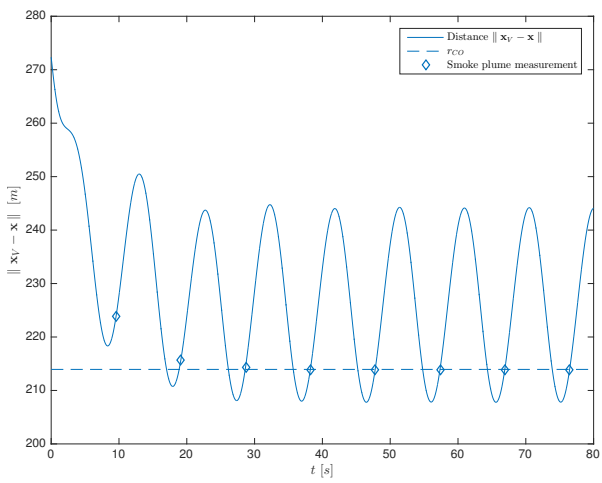

(b) Distance between the vessel and the UAV

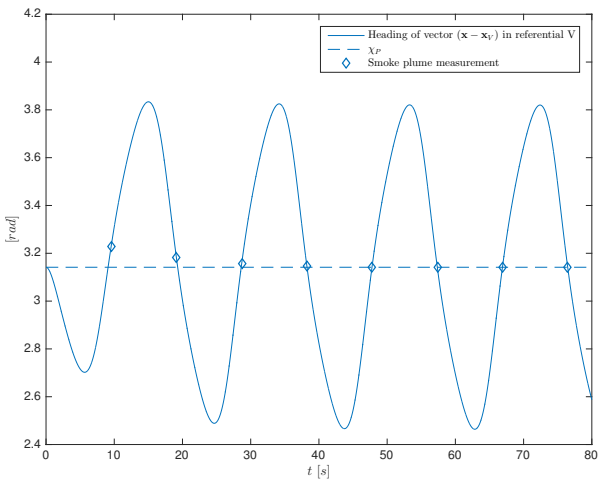

(c) Heading of the relative vector from vessel to UAV in referential $\{V\}$. Plume heading in dashed line.

Figure 4.35: Final simulation with the implementation of the full Guidance and Control System, with the second CO positionning method

As a result from the CO positioning method implemented in the previous simulation, the distance between the smoke plume measurement point and the vessel is not optimized to the keep-out area radius, given the considered approximations in the computation of d_{max} (2.33). However, this is the solution that enables the higher periodicity between consecutive smoke measurements. If a more precise distance for the smoke plume measurement is needed, the second CO positioning method can be used, with the regulation of the oscillation phase from the formulation in (2.34). The results from the implementation of this solution are depicted in Figure 4.36.

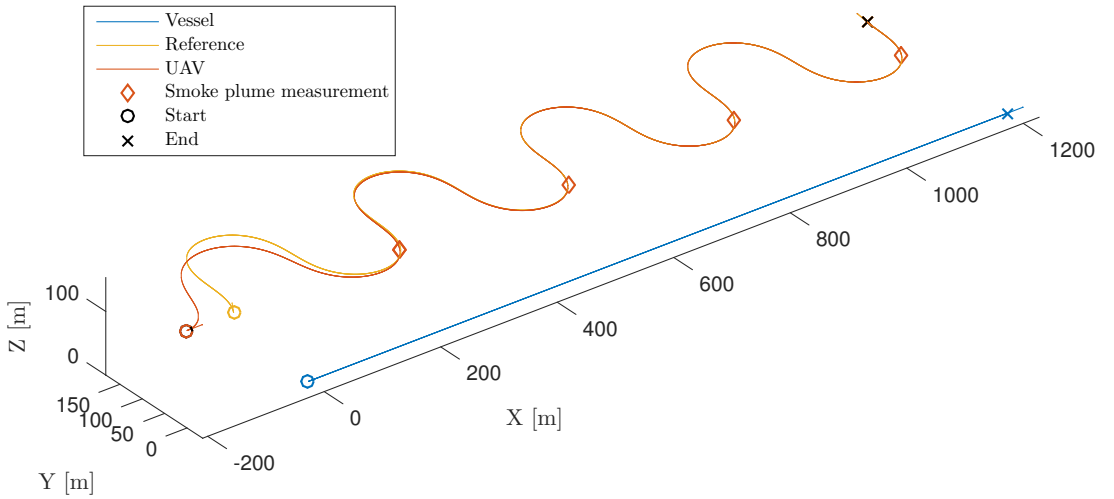

(a) Trajectories of vessel, reference, and UAV

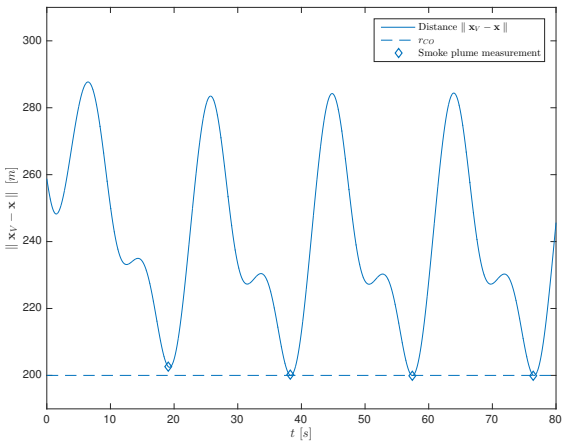

(b) Distance between the vessel and the UAV

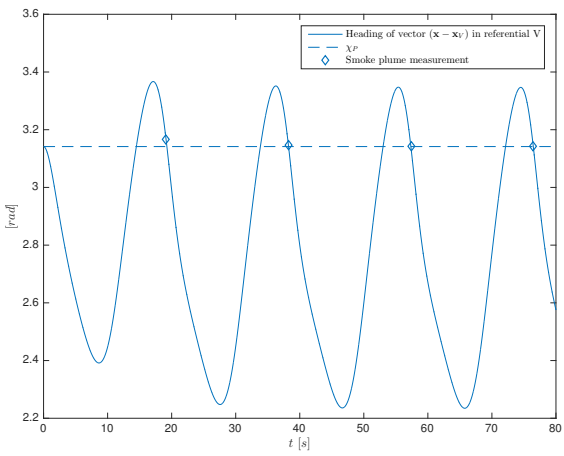

(c) Heading of the relative vector from vessel to UAV in referential $\{V\}$. Plume heading in dashed line.

Figure 4.36: Final simulation illustrating the implementation of the full Guidance and Control System, for the more rigorous CO positionning method

With this solution, one can see that the smoke plume measurements can be performed exactly in the border of the keep-out area, in the precise heading of the smoke plume. The only disadvantage of this solution, when compared with the previous one, is that the UAV only crosses the smoke plume measurement point once every oscillation period, enabling only a period of 19 s between consecutive measurements. In addition, the oscillation period can be reduced up to half of the previous value if the oscillation frequency ω_0 is set accordingly, up to the value that leads the reference trajectory ω_{r} to reach the UAV maximum heading rate. If larger values of ω_{r} are presented, however, the convergence time can be considerably increased, as the control parameters should be regulated to ensure a suitable control effort. Nevertheless, if higher values of ω_{r} in the nominal tracking trajectory are needed, an adaptive motion planning technique can be used for the initial UAV convergence, as introduced previously in the simulation of Figure 4.30.

4.4 Discussion of the Results

This chapter serves as a complement to the previous ones where the separated guidance and control systems were developed. Here both systems are combined and the overall system is implemented, in order to achieve the main goal of this dissertation, which is for a UAV to track the smoke plume of a marine vessel. Several simulations are performed as well, in order to validate the theoretical results introduced in the previous chapters, as well as to provide further analysis on the involved variables.

Firstly, a simulation is performed to assess the implementation of the guidance system of Chapter 2, generating a reference trajectory to follow a vessel with variable speed. It is possible to confirm the good performance of the proposed guidance solution, mainly the way it is able to adjust the resulting reference trajectory to the slower vessel speed, through the tuning of parameter η, being able to reshape continuously as the vessel speed changes. The effect of parameter ω_0 is also observed, as it is used to regulate the maximum value reached by the reference heading rate, which is always lower than the maximum achievable by the pursuer. The continuous positioning of the CO leads the reference trajectory to approach the keep-out area as the vessel speed changes, allowing for successive crossings through the smoke plume in a region relatively close to the vessel – given the considered restrictions –, thus providing the desirable conditions to perform the gas measurements.

The control system developed in Chapter 3 was also implemented, and several simulations were carried out to illustrate some of the theoretical aspects previously introduced, focusing on the analysis of the main contribution of the proposed δ-control approach for the relative tracking problem formulation.

A series of simulation results was presented, showing some intermediate results to support the reasoning carried out to reach the final solution for the adaptive δ formulation. It was confirmed that as long as the norm of vector $\boldsymbol{\delta}$ is higher than the distance between the pursuer and the reference point, then the system never reaches the singularity. Moreover, it is noted that the relation between δ and distance d is decisive for the resulting value of the variation of the relative vector, ω_ρ and thus of the resulting control input. For an excessively high δ in comparison with the distance, the resulting value of ω_ρ will be very close to the reference heading rate, ω_r, leading to a very slow convergence. A smaller value of δ (close to the distance d) enables for a faster convergence. However, it can lead to the controller saturation if the value of ω_ρ exceeds the pursuer maximum heading rate. Hence, the proposed formulation with a variable δ, proportional to the squared norm of the distance, is found to be a suitable solution, adjusting to high values of the distance, so the singularity is never reachable, while providing a good convergence when the system approaches the desired state.

In order to understand the advantages of the proposed δ formulation with respect to the direct line-of-sight control, a specific scenario was simulated, where the latter leads the system to approach the singularity and thus leading to the saturation of the controller, and showing how the proposed formulation behaves in the same situation, providing a feasible control command to lead the system to the desired state.

The proposed solution was then compared to a similar approach discussed in Chapter 3, which considers also the δ approach, although with the value of δ inversely proportional to the distance. In the performed simulations, the intuitive aspect of this alternative solution was confirmed, leading to a much faster convergence for large initial distance errors, with minimal oscillations, as well as the absence of the singularity in the desired point (contrary to the direct line-of-sight approach). However, this solution becomes impracticable, as it can still reach the singularity at some point, leading to the saturation of the controller. The proposed solution, in turn, although leading to a slower convergence for large initial distance errors, ensures that the singularity is always avoided, as long as the control parameters ε and R are properly adjusted.

Given the proposed error formulation with the adaptive δ, there are three parameters to be tuned in order to regulate the effectiveness of the considered controller, namely the control gain k, which appears directly in the control law of (3.67), and control parameters ε and R, which indirectly affect the evolution of ω_ρ as they are essential for the evolution of variable δ.

The first parameter to be tuned is the control gain k, which regulates directly the variable ϕ with the considered controller. As concluded in the theoretical results of Chapter 3, the system error is always monotonically decreasing as long as $\phi = 0$ rad, and, thus, the faster variable ϕ converges to zero, the faster the convergence of the system to the desired point. This result was confirmed by the performed simulations, with stark differences in the system evolution for different values of k. Moreover, an adaptive gain k was implemented, adjusting its value to the current value of ϕ, providing a fast convergence for lower values of ϕ, while ensuring the control input does not saturate when higher values of ϕ hold.

Thereafter, several simulations were performed with different values of the control parameters ε and

R, which are essential to trade-off between control effort and convergence rate of the controller. As expected, higher values of ε and R lead to a high value of δ, thus leading to a slower convergence. On the other hand, if too low (considering its corresponding range), they can lead to a saturation of the control input. Moreover, it was observed that the value of ε has a greater impact on the distance error convergence for larger values of the distance, while the value of R is more influent for lower distance errors. Hence, a good compromise between both parameters should be found, in order to enable a good performance during all the simulation, while ensuring the feasibility of the control law. Therefore, some of the pairs of parameters (ε, R) listed in Table 3.2, which all ensure the control system is able to enforce the actuation bounds, where implemented in order to assess which one provides the best performance, for the case when $\omega_\mathsf{r} = 0.5$ rad, and the pair that was found to provide the best compromise is $(\varepsilon, R) = \left(0.02\ m^{-1}, 112\ m\right)$.

Considering reference trajectories with constant heading rates, the extreme cases were assessed, for a straight-line reference, $\omega_r = 0$ rad/s, and for a reference with the pursuer maximum heading rate, $\omega_r = 1$ rad/s. For the first case, the theoretical results from Chapter 3 were confirmed, as for a straight-line reference with the same speed as the pursuer, the proposed solution only ensures the convergence of angles ϕ_r and ϕ to zero, leading to the alignment of the pursuer with the reference heading. However, regarding the final distance error, anything can be concluded, as it depends on the initial conditions. Considering the other extreme case, when the reference trajectory has the maximum heading rate achievable by the pursuer vehicle, it is not possible to ensure a suitable control effort with the proposed solution. Even with a high value of δ, the resulting control command to lead the pursuer to the reference trajectory will always oscillate around the reference heading rate, thus exceeding the limit.

Besides the constant heading rate references, the proposed control system is also applicable to reference trajectories with time-varying heading rates, as is the case of the trajectories generated by the guidance system of Chapter 2. Therefore, joining both guidance and control systems, it was possible to assess the effectiveness of the control system with the oscillatory trajectory from the guidance system, and it was found that the oscillatory reference heading rate leads to a better performance of the controller. The pairs of parameters in Table 3.2 can be used considering the maximum value achievable by the reference heading rate, in order to ensure that the resulting control input is always feasible by the pursuer vehicle.

The control system is unable to enforce the actuation bounds when the reference heading rate ω_r matches the maximum achievable by the pursuer ω_max, and when it is close to that limit, the performance is highly degraded, in order to ensure a suitable control effort for any possible error configuration. However, when the tracking error is already null, as long as the reference has a feasible trajectory, then it can be traced by the pursuer. Hence, a complete motion planning method can be applied, combining both guidance and control systems, generating the reference trajectory based on the current tracking error. That motion planning method, however, depends on each particular application, and an example is presented with a motion planning solution to lead the UAV to a circular trajectory with its maximum heading rate. As illustrated by another simulation, with the proposed guidance solution it is also possible to adjust the generated reference trajectory to the current tracking error, changing the oscillation frequency ω_0 between consecutive oscillation periods, as the resulting trajectory always crosses the CO.

Given the nature of the considered tracking control problem, where a reference trajectory is generated with the pursuer motion and then the pursuer vehicle is commanded to converge to that desired trajectory, only ideal conditions were considered for the nominal system, so that the behaviour of the proposed formulation could be easily investigated. However, the pursuer vehicle motion is susceptible to be disturbed by different kinds of perturbations. Hence, the system response to some typical perturbations was assessed, namely a constant offset in the real pursuer speed, which can arise e.g. from a malfunction of the airspeed sensors or from an error coming from the inner-loop controller responsible for the reference speed tracking, and also a constant wind, which is also a typical perturbation to all the aerial vehicles.

When a constant offset was applied to the UAV, it was able to align its heading with the relative vector, and in the case of a circular reference trajectory, converging to a trajectory with the same heading rate as the reference, although with a different radius of curvature, due to the speed differential. In the case of a reference trajectory from the guidance system, particularly for a speed ratio of $\nu = 0$, the resulting UAV trajectory was identical to the reference, also with a different radius of curvature, despite crossing its center very close to the desired CO. The performance of the control system in the presence of this perturbation can be considered to be acceptable, as it is physically impossible to track perfectly a reference trajectory with different speed. It is also possible to notice the advantage of this new formulation in comparison with the direct line-of-sight approach, as the latter would lead to a saturation

of the controller and would not reach an equilibrium state in the case when the UAV is faster than the reference.

The control system response in the presence of a constant wind speed was also assessed. The unmodeled wind in the reference point dynamics goes against the basic principle of generating a reference trajectory with the same dynamics as the pursuer vehicle, and thus, it is not sure that the pursuer will be able to keep track with the reference. As observed in the simulations, with the proposed control formulation the resulting UAV trajectory will be shifted in the wind direction in relation to the reference trajectory. If higher values of the control parameters ε and R are applied, leading to higher values of δ, the control input scope is reduced, and the UAV is not able to maintain a bounded error, diverging in the wind direction. The same happens in the presence of stronger wind, as it becomes unfeasible for the pursuer vehicle to draw the same trajectories in relation to the ground, leading to the same effect as depicted in Figure 2.2b.

Therefore, considering a constant wind scenario and also that the wind velocity is known – it can be estimated by using the methods available in the literature, as described in Section 1.2 –, this information can be included in the reference point dynamics, leading to feasible trajectories in the presence of wind. This approach was implemented and, instead of tracking the true vessel speed, the reference trajectory was generated to follow the apparent velocity of the vessel in relation to the airmass. In the simulation results presented, the effectiveness of this method is validated, with the resulting trajectories being able to compensate the airmass movement while maintaining its crossing points through the desired CO.

Finally, the overall system was implemented in a three-dimensional scenario, simulating the UAV tracking to the vessel by means of the reference point. Here the main goal of this dissertation was achieved, with the proper tracking of the UAV with respect to the vessel, with a trajectory adjusted to the speed differential between both vehicles, leading to a close flight of the UAV to the keep-out area around the vessel, crossing the smoke plume for consecutive times, providing ideal conditions for the periodic smoke plume measurements.

Chapter 5

Conclusions and Future Work

Motivated by the recent trends in the airborne monitorization of the gas emissions of marine vessels, the main goal of this dissertation was to develop a Guidance and Control System for an autonomous fixed-wing UAV, in order to enable the tracking of a marine vessel, providing enhanced conditions for the smoke plume measurements. Given the speed differential between both vehicles – with the UAV assumed to be faster than the vessel –, the UAV should be able to keep track with the vessel, while performing consecutive crossings through the smoke plume, being able to avoid a keep-out area around the vessel. Hence, the adopted solution for the posed tracking problem was divided into two complementary systems: the guidance system, responsible for the trajectory planning, and the control system, dealing with the trajectory tracking.

First, the guidance solution adopted in this work consists in the generation of a virtual reference point with the same dynamics as the UAV, having a desired trajectory to meet the given mission restrictions. An oscillatory approach was applied to the reference heading rate, and the proper tuning of the parameters enabled the reference trajectory to adjust its shape to the vessel velocity while satisfying the UAV maximum heading rate. The center of the oscillatory trajectory was then placed in the desired smoke plume measurement point, allowing for consecutive crossings through the smoke plume, while respecting the minimum allowed distance to the vessel. With the generation of this reference point, the former problem of tracking a slower target with the given mission constraints is then simplified to the tracking of a virtual target with the speed as the pursuer and a feasible trajectory.

The proposed control system aims to minimize the tracking distance error, leading the UAV to converge to the desired reference trajectory. However, given the nonholonomic constraints on the UAV dynamics, and the assumption of constant speed, this tracking problem is not trivial, as the only available control action is on the UAV heading rate. Despite the vast research available in the literature on the tracking control problem of nonholonomic vehicles, and to the best of the author's knowledge, the existing works consider the control actuation on both the pursuer speed and heading rate. When the pursuer speed is fixed, a formal proof of stability was lacking and the problem was still unresolved. Hence, a novel error formulation for the tracking control problem is here proposed, being the main theoretical contribution of this dissertation.

The proposed error formulation removes the singularity that arises on the usual tracking control problems based on the line-of-sight between the pursuer and the target. Here a new variable δ was introduced, and the relative vector was redefined, adjusting the relative reference frame to the tracking distance error, such that the relative vector was always well-defined for any system configuration. Moreover, a control law was derived for the pursuer heading rate, and global asymptotic stability was achieved, ensuring the pursuer vehicle was able to converge to any given feasible reference trajectory in a finite time, from any initial position. The control system performance was assessed, and sufficient conditions for the control parameters were presented, ensuring the enforcement of the actuation bounds.

The overall system was implemented, and all the proposed objectives were successfully accomplished, with the designed system being able to lead the UAV to a trajectory following the vessel, and performing consecutive crossings to its smoke plume, providing ideal conditions to perform the smoke plume measurements.

Despite this specific application, the designed system can be adapted to a wide range of scenarios, involving different kinds of pursuers with nonholonomic constraints, as well as different targets having predictable trajectories and constrained velocities, such as vessels, ground vehicles, cycling events or regattas, and can also generate trajectories for multiple UAVs to perform coordinated flights.

5.1 Future Work

During the development of this dissertation, several areas have been identified that can benefit from further analysis. Several assumptions and simplifications were considered, mainly on the UAV dynamics. The overall UAV motion was modeled as a Dubins vehicle and the only considered restriction, besides the constant speed, was the maximum heading rate. However, if all the inner control loops are considered, the UAV may not be able to keep track exactly with the resulting control commands, for example with extreme variations in the heading rate. Therefore, the implementation of the designed system in a complete UAV model would provide more realistic results.

Concerning the guidance system, the vessel motion was assumed with minimal course variation, which is reasonable for the considered mission. However, the designed trajectory planning system is not ideal for larger variations of the target heading, given the derived parameters adjustment based on the mean speed in the heading direction of the target. Hence, it would be interesting to improve the proposed oscillatory heading rate expression, possibly by adding other sinusoidal terms with new parameters, in order to provide the tracking of targets with faster heading variations.

Regarding the proposed control system, with particular emphasis on the novel relative error formulation, despite providing a suitable method for the tracking control problem, the proposed δ-formulation leads to a degradation of the performance for larger values of the distance error. Hence, further analysis can be made to improve this concept, either with an adaptive tuning of the control parameters ε and R, or by resorting to a reformulation of the definition of δ, for example with an expression of the form $\delta = \frac{d^2}{d+\varepsilon} + R$.

Additionally, considering the specific mission of the UAV-based smoke plume measurements, further investigation could be undertaken in order to improve the system capabilities, for example employing image processing algorithms. In this dissertation, both the UAV and the vessel positions and velocities are assumed to be completely known. However, in a real-world scenario, there are several uncertainties associated with both the UAV navigation and inertial systems, while also the determination of the vessel motion can be a great challenge. Hence, given the recent developments in the field, an image processing algorithm can be implemented to determine the relative position and motion between both vehicles, complemented with a proper estimator for those variables.

An image processing algorithm for the smoke plume detection would be also a very interesting research line, harnessing that information for the wind velocity estimation, and also to investigate how that information could be used to improve the designed guidance system.

Finally, it is also recalled that all the considered models and equations in this dissertation are described by continuous-time representations. However, actual UAV controllers are implemented by means of discrete-time algorithms, which can bring about several associated issues. Therefore, further work can be conducted on extending the adopted control techniques to the discrete-time domain.

Bibliography

[1] IMO, "Third IMO Greenhouse Gas Study 2014: Executive Summary and Final Report," Releasable to the Public.

[2] The Economist, "Green finance for dirty ships," Available at `https://goo.gl/7w5Fru` (2017/09/13).

[3] IMO, "MARPOL Annex VI, Sulphur oxides (SOx) - Regulation 14," Releasable to the Public.

[4] CompMon, "CompMon long term strategy," Releasable to the Public.

[5] W. Van Roy and K. Scheldeman, "Best Practices Airborne MARPOL Annex VI Monitoring," 2016.

[6] W. Van Roy and K. Scheldeman, "Results MARPOL Annex VI Monitoring Report – Belgian Sniffer Campaign 2016," 2016.

[7] Z. Xiong, R. Caballero, H. Wang, A. M. Finn, M. A. Lelic, and P.-Y. Peng, "Video-based Smoke Detection: Possibilities, Techniques, and Challenges," in *IFPA, fire suppression and detection research and applications—a technical working conference (SUPDET), Orlando, FL*, 2007.

[8] T.-H. Chen, Y.-H. Yin, S.-F. Huang, and Y.-T. Ye, "The Smoke Detection for Early Fire-Alarming System Base on Video Processing," in *International Conference on Intelligent Information Hiding and Multimedia Signal Processing*, pp. 427–430, IEEE, 2006.

[9] B. C. Ko, K.-H. Cheong, and J.-Y. Nam, "Fire detection based on vision sensor and support vector machines," *Fire Safety Journal*, vol. 44, no. 3, pp. 322–329, 2009.

[10] L. Merino, F. Caballero, J. R. Martínez-de Dios, I. Maza, and A. Ollero, "An Unmanned Aircraft System for Automatic Forest Fire Monitoring and Measurement," *Journal of Intelligent & Robotic Systems*, vol. 65, no. 1, pp. 533–548, 2012.

[11] L. Merino, F. Caballero, J. R. Martínez-de Dios, J. Ferruz, and A. Ollero, "A cooperative perception system for multiple UAVs: Application to automatic detection of forest fires," *Journal of Field Robotics*, vol. 23, no. 3-4, pp. 165–184, 2006.

[12] D. W. Casbeer, D. B. Kingston, R. W. Beard, and T. W. McLain, "Cooperative Forest Fire Surveillance Using a Team of Small Unmanned Air Vehicles," *International Journal of Systems Science*, vol. 37, no. 6, pp. 351–360, 2006.

[13] B. U. Töreyin, Y. Dedeoğlu, and A. E. Cetin, "Wavelet Based Real-Time Smoke Detection in Video," in *13th European Signal Processing Conference*, pp. 1–4, IEEE, 2005.

[14] S. Calderara, P. Piccinini, and R. Cucchiara, "Vision based smoke detection system using image energy and color information," *Machine Vision and Applications*, vol. 22, no. 4, pp. 705–719, 2011.

[15] Z. Xu and J. Xu, "Automatic Fire Smoke Detection Based on Image Visual Features," in *Proceedings of International Conference on Computational Intelligence and Security Workshops*, pp. 316–319, IEEE, 2007.

[16] J. Yang, F. Chen, and W. Zhang, "Visual-Based Smoke Detection Using Support Vector Machine," in *Fourth International Conference on Natural Computation*, vol. 4, pp. 301–305, IEEE, 2008.

[17] F. Yuan, "A Fast Accumulative Motion Orientation Model Based on Integral Image for Video Smoke Detection," *Pattern Recognition Letters*, vol. 29, no. 7, pp. 925–932, 2008.

[18] C.-Y. Lee, C.-T. Lin, C.-T. Hong, M.-T. Su, *et al.*, "Smoke Detection using Spatial and Temporal Analyses," *International Journal of Innovative Computing, Information and Control*, vol. 8, no. 7, pp. 4749–4770, 2012.

[19] J. M. Soares, A. P. Aguiar, A. M. Pascoal, and A. Martinoli, "A Graph-Based Formation Algorithm for Odor Plume Tracing," in *Distributed Autonomous Robotic Systems*, pp. 255–269, Springer, 2016.

[20] P. P. Neumann, S. Asadi, A. J. Lilienthal, M. Bartholmai, and J. H. Schiller, "Autonomous Gas-Sensitive Microdrone: Wind Vector Estimation and Gas Distribution Mapping," *IEEE Robotics & Automation Magazine*, vol. 19, no. 1, pp. 50–61, 2012.

[21] P. P. Neumann, V. Hernandez Bennetts, A. J. Lilienthal, M. Bartholmai, and J. H. Schiller, "Gas Source Localization With a Micro-Drone Using Bio-Inspired and Particle Filter-Based Algorithms," *Advanced Robotics*, vol. 27, no. 9, pp. 725–738, 2013.

[22] C. Lefas, "Real-Time Wind Estimation and Tracking with Transponder Downlinked Airspeed and Heading Data," *IEEE Transactions on Aerospace and Electronic Systems*, no. 2, pp. 169–174, 1987.

[23] D. Delahaye, S. Puechmorel, and P. Vacher, "Windfield Estimation by Radar Track Kalman filtering and Vector Spline Extrapolation," in *Digital Avionics Systems Conference*, IEEE, 2003.

[24] J. W. Langelaan, N. Alley, and J. Neidhoefer, "Wind Field Estimation for Small Unmanned Aerial Vehicles," *Journal of Guidance Control and Dynamics*, vol. 34, no. 4, p. 1016, 2011.

[25] M. Kumon, I. Mizumoto, Z. Iwai, and M. Nagata, "Wind Estimation by Unmanned Air Vehicle with Delta Wing," in *The IEEE International Conference on Robotics and Automation*, pp. 1896–1901, IEEE, 2005.

[26] A. Van den Kroonenberg, T. Martin, M. Buschmann, J. Bange, and P. Vörsmann, "Measuring the Wind Vector Using the Autonomous Mini Aerial Vehicle M^2AV," *Journal of Atmospheric and Oceanic Technology*, vol. 25, no. 11, pp. 1969–1982, 2008.

[27] M. Rhudy, T. Larrabee, H. Chao, Y. Gu, and M. R. Napolitano, "UAV Attitude, Heading, and Wind Estimation Using GPS/INS and an Air Data System," 2013.

[28] A. Cho, J. Kim, S. Lee, and C. Kee, "Wind Estimation and Airspeed Calibration Using a UAV with a Single-Antenna GPS Receiver and Pitot Tube," *IEEE Transactions on Aerospace and Electronic Systems*, vol. 47, no. 1, pp. 109–117, 2011.

[29] T. A. Johansen, A. Cristofaro, K. Sørensen, J. M. Hansen, and T. I. Fossen, "On Estimation of Wind Velocity, Angle-of-Attack and Sideslip Angle of Small UAVs Using Standard Sensors," in *International Conference on Unmanned Aircraft Systems*, pp. 510–519, IEEE, 2015.

[30] R. W. Beard and T. W. McLain, *Small Unmanned Aircraft: Theory and Practice*. Princeton University Press, 2012.

[31] L. E. Dubins, "On Curves of Minimal Length with a Constraint on Average Curvature, and with Prescribed Initial and Terminal Positions and Tangents," *American Journal of mathematics*, vol. 79, no. 3, pp. 497–516, 1957.

[32] R. W. Beard, "A Class of Flight Trajectories for Tracking Ground Targets with Micro Air Vehicles," in *Mediterranean Conference on Control & Automation*, pp. 1–6, IEEE, 2007.

[33] J. Lee, R. Huang, A. Vaughn, X. Xiao, J. K. Hedrick, M. Zennaro, and R. Sengupta, "Strategies of Path-Planning for a UAV to Track a Ground Vehicle," in *AINS Conference*, 2003.

[34] E. Lalish, K. A. Morgansen, and T. Tsukamaki, "Oscillatory Control for Constant-Speed Unicycle-Type Vehicles," in *Conference on Decision and Control*, pp. 5246–5251, IEEE, 2007.

[35] N. Regina and M. Zanzi, "UAV Guidance Law for Ground-based Target Trajectory Tracking and Loitering," in *Aerospace Conference*, pp. 1–9, IEEE, 2011.

[36] P. Tabuada and P. Lima, "Position Tracking for Underactuated Rigid Bodies on SE (3)," *IFAC Proceedings Volumes*, vol. 34, no. 6, pp. 1147–1152, 2001.

[37] T. Oliveira and P. Encarnação, “Ground Target Tracking Control System for Unmanned Aerial Vehicles,” *Journal of Intelligent & Robotic Systems*, pp. 1–15, 2013.

[38] E. W. Frew, D. A. Lawrence, C. Dixon, J. Elston, and W. J. Pisano, “Lyapunov Guidance Vector Fields for Unmanned Aircraft Applications,” in *American Control Conference*, pp. 371–376, IEEE, 2007.

[39] D. Cabecinhas, C. Silvestre, P. Rosa, and R. Cunha, “Path-Following Control for Coordinated Turn Aircraft Maneuvers,” in *AIAA Guidance, Navigation and Control Conference and Exhibit*, vol. 35, 2007.

[40] J. Saunders and R. Beard, “Tracking a Target in Wind Using a Micro Air Vehicle with a Fixed Angle Camera,” in *American Control Conference*, pp. 3863–3868, IEEE, 2008.

[41] V. N. Dobrokhodov, I. I. Kaminer, K. D. Jones, and R. Ghabcheloo, “Vision-Based Tracking and Motion Estimation for Moving Targets Using Small UAVs,” in *American Control Conference*, IEEE, 2006.

[42] V. N. Dobrokhodov, I. I. Kaminer, K. D. Jones, and R. Ghabcheloo, “Vision-Based Tracking and Motion Estimation for Moving Targets Using Unmanned Air Vehicles,” *Journal of guidance, control, and dynamics*, vol. 31, no. 4, p. 907, 2008.

[43] Z. Li, N. Hovakimyan, V. Dobrokhodov, and I. Kaminer, “Vision-Based Target Tracking and Motion Estimation Using a Small UAV,” in *49th IEEE Conference on Decision and Control*, pp. 2505–2510, IEEE, 2010.

[44] L. Ma, C. Cao, N. Hovakimyan, C. Woolsey, and W. E. Dixon, “Fast Estimation for Range Identification in the Presence of Unknown Motion Parameters,” *IMA journal of applied mathematics*, vol. 75, no. 2, pp. 165–189, 2010.

[45] D. B. Barber, J. D. Redding, T. W. McLain, R. W. Beard, and C. N. Taylor, “Vision-Based Target Geo-Location Using a Fixed-Wing Miniature Air Vehicle,” *Journal of Intelligent & Robotic Systems*, vol. 47, no. 4, pp. 361–382, 2006.

[46] M. Mallick, “Geolocation Using Video Sensor Measurements,” in *10th International Conference on Information Fusion*, pp. 1–8, IEEE, 2007.

[47] S. S. Ponda, R. M. Kolacinski, and E. Frazzoli, *Trajectory Optimization for Target Localization Using Small Unmanned Aerial Vehicles*. PhD thesis, Massachusetts Institute of Technology, Department of Aeronautics and Astronautics, 2008.

[48] E. W. Frew, “Sensitivity of Cooperative Target Geolocalization to Orbit Coordination,” *Journal of Guidance, Control, and Dynamics*, vol. 31, no. 4, p. 1028, 2008.

[49] R. Anderson and D. Milutinović, “A Stochastic Approach to Dubins Feedback Control for Target Tracking,” in *IEEE/RSJ International Conference on Intelligent Robots and Systems*, pp. 3917–3922, IEEE, 2011.

[50] S. A. Quintero and J. P. Hespanha, “Vision-Based Target Tracking with a Small UAV: Optimization-Based Control Strategies,” *Control Engineering Practice*, vol. 32, pp. 28–42, 2014.

[51] H. Oh, S. Kim, H.-S. Shin, A. Tsourdos, and B. White, “Coordinated Standoff Tracking of Groups of Moving Targets Using Multiple UAVs,” in *21st Mediterranean Conference on Control & Automation*, pp. 969–977, IEEE, 2013.

[52] S. A. Quintero, F. Papi, D. J. Klein, L. Chisci, and J. P. Hespanha, “Optimal UAV Coordination for Target Tracking Using Dynamic Programming,” in *49th IEEE Conference on Decision and Control*, pp. 4541–4546, IEEE, 2010.

[53] M. Stachura, A. Carfang, and E. W. Frew, “Cooperative Target Tracking with a Communication Limited Active Sensor Network,” in *In Proceedings of the International Workshop on Robotic Wireless Sensor Networks, Marina Del Rey*, Citeseer, 2009.

[54] S. A. Quintero, D. A. Copp, and J. P. Hespanha, "Robust UAV Coordination for Target Tracking Using Output-Feedback Model Predictive Control with Moving Horizon Estimation," in *American Control Conference*, pp. 3758–3764, IEEE, 2015.

[55] S. A. Quintero, D. A. Copp, and J. P. Hespanha, "Robust Coordination of Small UAVs for Vision-Based Target Tracking Using Output-Feedback MPC with MHE," *Cooperative Control of Multi-Agent Systems: Theory and Applications*, p. 51, 2017.

[56] J. Diebel, "Representing Attitude: Euler Angles, Unit Quaternions, and Rotation Vectors," *Matrix*, vol. 58, no. 15-16, pp. 1–35, 2006.

[57] C. Samson and K. Ait-Abderrahim, "Feedback Control of a Nonholonomic Wheeled Cart in Cartesian Space," in *International Conference on Robotics and Automation*, pp. 1136–1141, IEEE, 1991.

[58] Y. Kanayama, Y. Kimura, F. Miyazaki, and T. Noguchi, "A Stable Tracking Control Method for a Non-Holonomic Mobile Robot," in *International Workshop on Intelligent Robots and Systems*, pp. 1236–1241, IEEE, 1991.

[59] R. Fierro and F. L. Lewis, "Control of a Nonholonomic Mobile Robot: Backstepping Kinematics Into Dynamics," in *Proceedings of the 34th IEEE Conference on Decision and Control*, vol. 4, pp. 3805–3810, IEEE, 1995.

[60] I. Kolmanovsky and N. H. McClamroch, "Developments in Nonholonomic Control Problems," *IEEE Control Systems*, vol. 15, no. 6, pp. 20–36, 1995.

[61] Z.-P. Jiang and H. Nijmeijer, "Tracking Control of Mobile Robots: a Case Study in Backstepping," *Automatica*, vol. 33, no. 7, pp. 1393–1399, 1997.

[62] A. A. J. Lefeber, *Tracking Control of Nonlinear Mechanical Systems*. Universiteit Twente, 2000.

[63] T.-C. Lee, K.-T. Song, C.-H. Lee, and C.-C. Teng, "Tracking Control of Unicycle-Modeled Mobile Robots Using a Saturation Feedback Controller," *IEEE Transactions on Control Systems Technology*, vol. 9, no. 2, pp. 305–318, 2001.

[64] K.-C. Cao, "Formation Control of Multiple Nonholonomic Mobile Robots Based on Cascade Design," in *Proceedings of the 48th IEEE Conference on Decision and Control*, pp. 8340–8344, IEEE, 2009.

[65] S. Park, J. Deyst, and J. P. How, "A New Nonlinear Guidance Logic for Trajectory Tracking," in *AIAA Guidance, Navigation, and Control Conference and Exhibit*, pp. 16–19, 2004.

[66] H. Khalil, *Nonlinear Systems, Upper Saddle River, New Jersey: Pretice-Hall Inc*. Pearson Education International, 2000.

[67] R. C. Dorf and R. H. Bishop, *Modern Control Systems*. Pearson, 2011.

[68] J.-J. E. Slotine, W. Li, *et al.*, *Applied Nonlinear Control*, vol. 199. Prentice hall Englewood Cliffs, NJ, 1991.

[69] P. Seibert and R. Suarez, "Global Stabilization of Nonlinear Cascade Systems," *Systems & Control Letters*, vol. 14, no. 4, pp. 347–352, 1990.

[70] V. Sundarapandian, "Global Asymptotic Stability of Nonlinear Cascade Systems," *Applied Mathematics Letters*, vol. 15, no. 3, pp. 275–277, 2002.

[71] V. Sundarapandian, "Local and Global Asymptotic Stability of Nonlinear Cascade Interconnected Systems," *Mathematical and Computer Modelling*, vol. 40, no. 1-2, pp. 227–232, 2004.

[72] E. Panteley and A. Loría, "On Global Uniform Asymptotic Stability of Nonlinear Time-Varying Systems in Cascade," *Systems & Control Letters*, vol. 33, no. 2, pp. 131–138, 1998.

[73] E. Panteley and A. Loría, "Growth Rate Conditions for Uniform Asymptotic Stability of Cascaded Time-Varying Systems," *Automatica*, vol. 37, no. 3, pp. 453–460, 2001.

[74] A. Loría and E. Panteley, "Cascaded Nonlinear Time-Varying Systems: Analysis and Design," *Advanced Topics in Control Systems Theory*, pp. 23–64, 2005.

[75] F. Baldi, F. Ahlgren, T.-V. Nguyen, C. Gabrielii, and K. Andersson, "Energy and exergy analysis of a cruise ship," in *The 28th International Conference on Efficiency, Cost, Optimization, Simulation and Environmental Impact of Eeergy Systems, June 29-july 3, 2015, Pau, France*, Pau University, 2015.

Appendix A

Derivation of the error state dynamics

The error state formulation commonly used in the tracking control of nonholonomic vehicles, is represented as the difference between the configurations of the pursuer vehicle and the target reference, written in the pursuer body-fixed reference frame:

$$\mathbf{x}_e = \begin{bmatrix} x_e \\ y_e \\ \chi_e \end{bmatrix} = \begin{bmatrix} x_{\mathsf{r}}^B \\ y_{\mathsf{r}}^B \\ \chi_{\mathsf{r}} - \chi \end{bmatrix} = \mathcal{R}_I^B(\chi, 0, 0) \begin{bmatrix} x_{\mathsf{r}} - x \\ y_{\mathsf{r}} - x \\ \chi_{\mathsf{r}} - \chi \end{bmatrix} \tag{A.1}$$

Here follows the derivation of the error state dynamics of this fromulation:

$$\begin{aligned}
\dot{x}_e &= \frac{d}{dt}\big[\,(x_r - x)\cos\chi + (y_r - y)\sin\chi\big] \\
&= (\dot{x}_r - \dot{x})\cos\chi - (x_r - x)\,\dot{\chi}\sin\chi + (\dot{y}_r - \dot{y})\sin\chi + (y_r - y)\,\dot{\chi}\cos\chi \\
&= \big[\underbrace{-(x_r - x)\sin\chi + (y_r - y)\cos\chi}_{y_e}\big]\dot{\chi} + \dot{x}_{\mathsf{r}}\cos\chi + \dot{y}_{\mathsf{r}}\sin\chi - \big(\underbrace{\dot{x}\cos\chi + \dot{y}\sin\chi}_{v}\big) \\
&= y_e\omega - v + \dot{x}_{\mathsf{r}}\cos(\chi_{\mathsf{r}} - \chi_e) + \dot{y}_{\mathsf{r}}\sin(\chi_{\mathsf{r}} - \chi_e) \\
&= y_e\omega - v + \dot{x}_{\mathsf{r}}(\cos\chi_{\mathsf{r}}\cos\chi_e + \sin\chi_{\mathsf{r}}\sin\chi_e) + \dot{y}_{\mathsf{r}}(\sin\chi_{\mathsf{r}}\cos\chi_e - \cos\chi_{\mathsf{r}}\sin\chi_e) \\
&= y_e\omega - v + \big(\underbrace{\dot{x}_{\mathsf{r}}\cos\chi_{\mathsf{r}} + \dot{y}_{\mathsf{r}}\sin\chi_{\mathsf{r}}}_{V_{\mathsf{r}}}\big)\cos\chi_e + \big(\underbrace{\dot{x}_{\mathsf{r}}\sin\chi_{\mathsf{r}} - \dot{y}_{\mathsf{r}}\cos\chi_{\mathsf{r}}}_{=0}\big)\sin\chi_e \\
&= y_e\omega - v + V_{\mathsf{r}}\cos\chi_e
\end{aligned}$$

$$\begin{aligned}
\dot{y}_e &= \frac{d}{dt}\big[-(x_r - x)\sin\chi + (y_r - y)\cos\chi\big] \\
&= -(\dot{x}_r - \dot{x})\sin\chi - (x_r - x)\,\dot{\chi}\cos\chi + (\dot{y}_r - \dot{y})\cos\chi - (y_r - y)\,\dot{\chi}\sin\chi \\
&= -\big[\underbrace{(x_r - x)\cos\chi + (y_r - y)\sin\chi}_{x_e}\big]\dot{\chi} - \dot{x}_{\mathsf{r}}\sin\chi + \dot{y}_{\mathsf{r}}\cos\chi + \big(\underbrace{\dot{x}\sin\chi - \dot{y}\cos\chi}_{=0}\big) \\
&= -x_e\omega - \dot{x}_{\mathsf{r}}(\sin\chi_{\mathsf{r}}\cos\chi_e - \cos\chi_{\mathsf{r}}\sin\chi_e) + \dot{y}_{\mathsf{r}}(\cos\chi_{\mathsf{r}}\cos\chi_e + \sin\chi_{\mathsf{r}}\sin\chi_e) \\
&= -x_e\omega - \big(\underbrace{\dot{x}_{\mathsf{r}}\sin\chi_{\mathsf{r}} - \dot{y}_{\mathsf{r}}\cos\chi_{\mathsf{r}}}_{=0}\big)\cos\chi_e + \big(\underbrace{\dot{x}_{\mathsf{r}}\cos\chi_{\mathsf{r}} + \dot{y}_{\mathsf{r}}\sin\chi_{\mathsf{r}}}_{V_{\mathsf{r}}}\big)\sin\chi_e \\
&= -x_e\omega + V_{\mathsf{r}}\sin\chi_e
\end{aligned}$$

$$\dot{\chi}_e = \dot{\chi}_r - \dot{\chi} = \omega_r - \omega$$

$$\dot{\mathbf{x}}_e = \begin{bmatrix} \dot{x}_e \\ \dot{y}_e \\ \dot{\chi}_e \end{bmatrix} = \begin{bmatrix} y_e\omega - v + V_{\mathsf{r}}\cos\chi_e \\ -x_e\omega + V_{\mathsf{r}}\sin\chi_e \\ \omega_r - \omega \end{bmatrix} = \begin{bmatrix} \cos\chi_e & 0 \\ \sin\chi_e & 0 \\ 0 & 1 \end{bmatrix} \begin{bmatrix} V_{\mathsf{r}} \\ \omega_r \end{bmatrix} + \begin{bmatrix} -1 & y_e \\ 0 & -x_e \\ 0 & -1 \end{bmatrix} \begin{bmatrix} v \\ \omega \end{bmatrix} \tag{A.2}$$

Appendix B

State variables variation

Further results can be obtained with Algorithm 1, in particular the resulting ω_ρ when varying a single state variable. Hence, in order to understand how the value of ω_ρ is affected by the different state variables, it is presented in Figure B.1 three graphs illustrating the variation of ω_ρ with each one of the state variables.

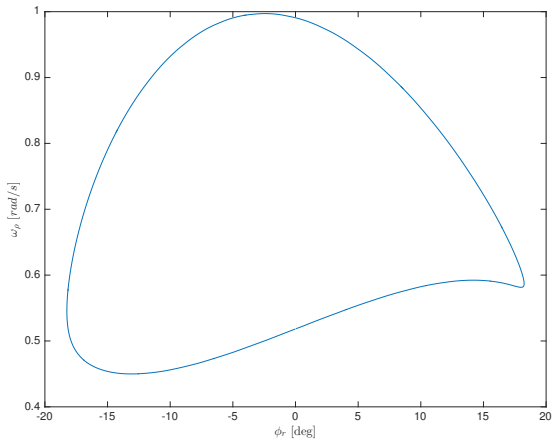

(a) Variation of the maximum value of ω_ρ along the domain of ϕ_r.

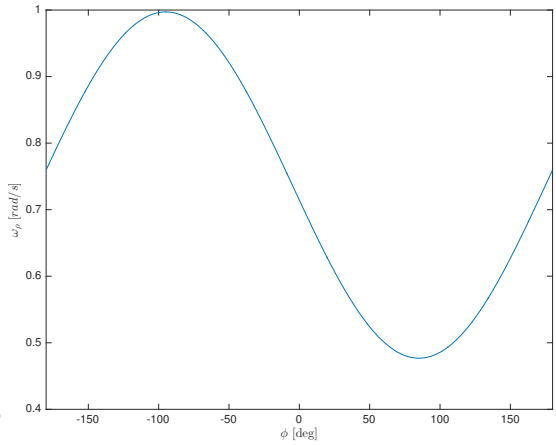

(b) Variation of the maximum value of ω_ρ along the domain of ϕ

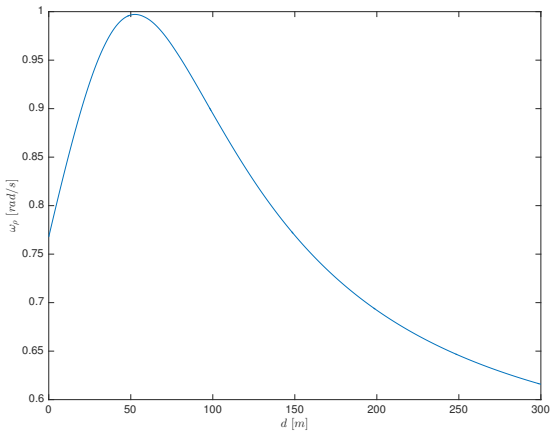

(c) Variation of the maximum value of ω_ρ along the distance d.

Figure B.1: Variation of the relative heading rate ω_ρ when varying single state variables. $V_\text{r} = 30$ m/s, $\omega_r = 0.5$ rad/s, $(\varepsilon, R) = (0.02, 112)$.

All of the three graphs in Figure B.1 consider a reference speed of $V_\text{r} = 30$ m/s, a maximum reference heading rate of $\omega_r = 0.5$ rad/s and parameters $(\varepsilon, R) = (0.02, 112)$ taken from Table (3.2). In B.1c, the maximum value of ω_ρ was found with Algorithm 1, and for each distance d all the possible system

configurations were tested. In Figure B.1a it is possible to see the constrained domain of variable ϕ_r, given by (3.38). Here, a fixed distance was considered, $d = 52$ m, that is the distance that leads to the highest value of ω_ρ for the considered parameters. There are two possible values of ω_ρ for a given angle ϕ_r, as there are two possible values of ρ for a fixed distance d and a given angle ϕ_r, as can be inferred from Figure 3.10. The higher values of ω_ρ correspond to the smaller value of ρ. In Figure B.1b the maximum value of ω_ρ is depicted along the domain of ϕ, corresponding to different headings of the UAV for a given relative position. Here the considered relative position was the one leading to the highest value of ω_ρ, and is given by $(d, \rho, \phi_r) = (52 \text{ m}, 114.4 \text{ m}, -2.4 \text{ deg})$.

From the previous figures, one can see that the maximum value of ω_ρ is obtained only for a very specific combination of the state variables, corresponding to a specific relative configuration between the UAV and the reference point. However, we should ensure the resulting control input can be feasible by the UAV and thus the worst possible case should be considered. Hence, knowing the maximum values of the reference heading rate ω_r, the pairs of parameters (ε, R) given in Table (3.2) ensure that the resulting relative heading rate ω_ρ is always lower than ω_{max}, and thus a feasible control command is guaranteed.